

DARK MATTER HALO CHARACTERIZATION THROUGH PROPERTIES OF THE HOST GALAXIES CLASSIFIED IN THE HUBBLE SEQUENCE

UNDERGRADUATE PROGRAM IN ASTRONOMY

Presented by:

JORGE ANDRÉS VILLA VÉLEZ

To obtain a Bsc degree in Astronomy

Advisor

Dr. Juan Carlos Muñoz Cuartas



**UNIVERSIDAD
DE ANTIOQUIA**

1 8 0 3

Instituto de Física
Facultad de Ciencias Exactas y Naturales
2014

ABSTRACT

The formation and evolution of galaxies has always been an important topic in order to know why the universe looks as it does today. In a Λ -CDM scenario dark matter collapses to build up halos which merge forming bigger halos. According to this theory barionic matter collapses into the dark matter halo forming galaxies, so, the properties of galaxies are expected to depend on or to be correlated to the dark matter halo properties [22]. Motivated by the Sloan digital Sky Survey Data Release 7 (SDSS-DR7) [7], data from the New York University Value-Added Galaxy Catalog (NYU-VAGC) [11] and a classification method performed by Huertas-Company, 2010 [19], we analyzed a sample of galaxies of the SDSS-DR7 to infer the connection between the structural parameters of the dark matter halo with the properties of the galaxy hosted in that halo. If structural differences in a given type of galaxy are related to structural differences in their halos, we are able to infer properties of the halo giving an independent test to the formation of structures and galaxies.

Data sample obtained from Huertas-Company, 2010 [19] has approximately 600.000 galaxies of the SDSS-DR7 which are tagged with a probability of belonging to an *E,S0,Sab and Scd* subclass. This information was enriched with properties of the objects extracted from NYU-VAGC as the petrosian magnitudes u,g,r,i,z , velocity dispersion, and the Sérsic's parameters A, R_0 and n in each band. Using the Color-Magnitude diagram (CMD) and the fundamental plane for each band we tested the quality of the dataset and the relation between the surface brightness profile with its respective type. Through the distribution of their Sérsic parameters, we obtained a direct connection between the dark matter halo parameter as spin, concentration and virial mass (λ, C, M_{vir}) with the photometric properties of the galaxy as surface brightness, disk scale length and Sérsic's index (A, R_0, n). Performing inference techniques we studied correlations between properties of a galaxy with the parameters of the dark matter halo where it should be hosted at.

It was observed a strong correlation between the Sérsic's parameters and the Hubble classification according to the technique shown by Huertas-Company, 2010 [19]. There are differences between galaxies classified as the same type as a function of its luminosity. We assume that we know how the properties of the dark matter halo are distributed, using this indicates that through an inference analysis is possible to estimate, at least in an statistical way, the properties of the halo. Using a model for disk galaxies it is possible to obtain the disk scale length and the surface density profile in terms of the dark matter halo structural parameters as concentration, virial mass and spin. Once the observed disk scale length and the model one are compared, each observed galaxy inherits the median values which better describes the dark matter halo where they are embedded at. A correlation between the spin parameter and the concentration (i.e virial mass) is found which tell us that a given dark matter halo will host a given disk galaxy only if its corresponding value of spin parameter it is related to the concentration. Also, tables corresponding to the results for the *Sab* and *Scd* SDSS-DR7 galaxies are shown which contains information about the disk and dark matter halo properties assigned after matching the observations with the model.

Key words: *Dark Matter - (DM), Photometric Properties, Dark Matter Halo Parameters, Correlations, Sérsic's Profile.*

*Mortal as I am, I know that I am born for a day,
but when I follow the serried multitude of the stars in their circular course,
my feet no longer touch the earth; I ascend to Zeus himself to feast me on ambrosia, the food of
the gods.*

—Claudius Ptolemy
(100 d.C - 170 d.C) Greco-Roman Astronomer.

ACKNOWLEDGMENTS

First and foremost I offer my sincerest gratitude to my supervisor, Dr. Juan Carlos Muñoz who has supported me throughout my thesis with his knowledge and his patience. Without his encouragement and effort this thesis would not be completed and written. He was a helping hand always teaching me new things about being a good scientist, about being a good researcher. All the fundamental values about investigation were given to me through his wisdom. I'm pretty grateful for his advices and continuous efforts to help me out to reach my goals and for turning me into a better scientist.

I am really grateful with my parents Jorge Mario Villa Marín and Gladys Vélez Muñoz who trusted in me, who always stayed by my side helping me and supporting me with my dreams and goals. They never let me down and always boosted me to keep on going on and to keep on fighting for what I wanted to become. They were my cornerstone which took me further and further away to succeed in this journey that closes a chapter today. I also want to thank to my family, my aunts Yomaira and Aida, my cousins Jeniffer, Bryan, Esteban, Jonathan and Janeth for being there in bad and good times, encouraging me to push through and reach goals. I am happy because I know they all feel really proud of me. To my Grandma who is not now among us, I wanna thank her all her advice and all the things she did for me to take me to the place I am now. I am really, really grateful with my uncle Joaquín Zuluaga Betancur for showing me since I was a child that math was easier than we thought, that science was an open door to discover new things and for helping me out to be a more reasoning and thinking person.

To Laura María Uribe Diez my girlfriend I wanna thank her so much for all her support, for believing in what I do, for trusting me and giving me all her best wishes throughout this long way. She was a big support to keep me on the right way to success, helping me either in bad or good times. My friends which begin to study with me are so special and I know that this goal is their goal too because we became like a new family. This dream is also their dream, so I wanna thank to Carlos Castillo, Carlos Eduardo, Jeisson Mejía, Mauricio Meneses, Karen, Carmenza Jaramillo, Diana Arango, Jeniffer Arboleda, Adriana Mora, Malory Agudelo, Mónica Villa, Nicolás Gómez, Yennifer Angarita, Nancy, Jorge(GAIA), Santiago Alvarado, Yeimy, David Millán, Valdimir, Bayron and all of those guys with which I enjoyed going outside to watch the stars and shared our common taste for Astronomy.

Indeed, I am grateful with all my physics friends as Nataly, Sebastián (Binney), César (El Coste) for all their helpful discussions, useful advices and support throughout this time, which opened my mind when I was stuck and helped me out to see a light when everything was dark. To Paula Otálvaro and Julián Mejía because they helped me when I was just a curious guy trying to learn something about stellar astronomy and for their long support. Heisman, Rodolfo, Carlos, Faber,

Andy, Robin, Alexis, Mateo, Juli, Elizabeth, Eliana, Mario Cadavid, Alejo Correa, Victor Moreno, Mariana, Alexandra, Sebastián Duque and David Ricardo for being with me through this journey and helping me to have great times. Also to the guys I knew when I was ending up this career as Diego Olmos, Daniel Montenegro, Julián Calle, Natalia Osorio, Rafael Arango, Vanesa Ramírez, Alejo Guerra, Juan Orión, Julio (Sheepo) and Juan Manuel Espejo.

Finally, all those professors who in one way or another gave all of them to teach me all I know now, who expended time to solve questions and help me with my issues. I am grateful with Jorge Zuluaga, Pablo Cuartas for believing that we could be the first colombian astronomers, Ignacio Ferrín, Carlos Molina, Daniel Jaramillo, Jesus Mira, Leonardo Pachón, John Fredy Barrera, José Luis Sanz, Boris Ángel Rodríguez and Oscar Zapata.

Thanks everyone, let's keep on doing and enjoying what we like to do and cheers ! .

CONTENT

1	THEORETICAL FRAMEWORK	1
1.1	Introduction	1
1.2	Morphological classification of galaxies	1
1.2.1	Hubble's tuning-fork diagram	3
1.2.2	De Vaucouleurs' system	7
1.2.3	Yerkes or Morgan's system	8
1.2.4	DDO or Van den Bergh's system	10
1.2.5	The Color-Magnitude diagram (CMD)	12
1.3	Properties of galaxies	13
1.3.1	Optical colors, luminosities and linear size	14
1.3.2	Optical surface brightness: Galaxy profile shape and surface brightness	14
1.3.3	Far infrared emission	15
1.3.4	Radio continuum emission	16
1.3.5	X-ray emission	16
1.3.6	Neutral Hydrogen Mass and Content	17
1.3.7	HII regions	17
1.3.8	Chemical abundances	17
1.3.9	Total Masses and Related Quantities	18
1.3.10	Global Properties: the effect of environment	18
1.4	Galaxy formation theory	18
1.4.1	Cosmological Scenario	19
1.4.2	Background Material	22
1.4.3	Pre-galactic Evolution of Baryons: Mechanisms of cooling and heating	24
1.4.4	Interactions: Mergers, harassment and hydrodynamical interactions	28
1.4.5	Galactic Structure	29
1.4.6	Properties of the dark matter halo and the connection with the host galaxy	33
2	OBSERVATIONAL DATA	37
2.1	Introduction	37
2.2	Research Data Repositories	37
2.2.1	Sloan Digital Sky Survey (SDSS) Data	38
2.2.2	The NYU Value-Added Galaxy Catalog (VAGC)	39
2.3	Automated Morphological Classification of the SDSS-DR7 Sample	41
2.4	Selection Criteria and Correlations	43
2.5	Data Tests	47
2.5.1	Fundamental Plane	47
2.5.2	SDSS units: Fundamental Plane	49
2.6	Sérsic's Profile Parameters	57
2.6.1	Distribution of the Sérsic Parameters Respect Petrosian Magnitudes	59
3	GALACTIC DISKS MODEL	71

3.1	Introduction	71
3.2	Data	71
3.3	Galactic disks model	72
3.4	Mo, Mao & White model	72
3.4.1	Model scheme	72
3.4.2	NFW model	73
3.4.3	Spin, Concentration, Virial Mass	75
3.5	Connection between observation and model	78
3.6	Comparison	80
4	DISCUSSION AND SUMMARY	95
4.1	Discussion	95
4.2	Future prospects	96
	BIBLIOGRAPHY	99

LIST OF FIGURES

Figure 1	Galaxy features comparison in two different bands	2
Figure 2	Hubble tuning-fork diagram	4
Figure 3	De Vaucouleurs' objects	8
Figure 4	De Vaucouleurs' three dimensional representation	9
Figure 5	Simplified Yerkes classification system	10
Figure 6	Comparison between Hubble and van den Bergh systems	12
Figure 7	Color-Magnitude Diagram	13
Figure 8	Surface brightness, size and concentration as a luminosity function	15
Figure 9	SDSS response to all five Petrosian bands u, g, r, i, z	39
Figure 10	Procedure to classify galaxies into a given type	42
Figure 11	Probability distribution for early-type	43
Figure 12	Probability distribution for $E, S0, Sab, Scd$ subclasses	44
Figure 13	Conditional probability distributions for early-type sample	45
Figure 14	Correlation between early-type and late-type samples	45
Figure 15	Conditional probability distributions for late-type sample (Early-type)	46
Figure 16	Conditional probability distributions for late-type sample (Late-type)	46
Figure 17	Probabilities distribution against the redshift	48
Figure 18	Fundamental plane projections onto different two parameters planes	49
Figure 19	Angular diameter and R_0 Sérsic's parameter relation	51
Figure 20	Fundamental plane in the u-Band	52
Figure 21	Fundamental plane in the g-Band	53
Figure 22	Fundamental plane in the r-Band	54
Figure 23	Fundamental plane in the i-Band	55
Figure 24	Fundamental plane in the z-Band	56
Figure 25	Color-magnitude diagram (CMD)	57
Figure 26	Velocity dispersion in ($km\ s^{-1}$) as function of the Petrosian r -band magnitude	58
Figure 27	Sérsic parameters A, R_0, n as a function of Petrosian magnitudes u, g, r, i, z	63
Figure 28	Sérsic's parameter A ($mag/arcsec^2$) histograms	64
Figure 29	Sérsic's parameter R_0 ($parsecs$) histograms	65
Figure 30	Sérsic's parameter n histograms	66
Figure 31	Sérsic's parameter A ($mag/arcsec^2$) histograms	67
Figure 32	Sérsic's parameter R_0 ($parsecs$) histograms	68
Figure 33	Sérsic's parameter n histograms	69
Figure 34	Spin distribution obtained through the acceptance-rejection method	75
Figure 35	Mass function distribution	76
Figure 36	Mass function distribution for $10^{10} M_\odot \leq M \leq 10^{13} M_\odot$	77
Figure 37	Concentration distribution against the virial mass	77
Figure 38	Disk scale length distribution	78
Figure 39	Surface density profile distribution	79
Figure 40	Selection method with disk scale lengths	80

Figure 41	Concentration distribution for four randomly choosen <i>Sab</i> matched galaxies	81
Figure 42	Spin distribution for four randomly choosen <i>Sab</i> matched galaxies	81
Figure 43	Virial mass distribution for four randomly choosen <i>Sab</i> matched galaxies	82
Figure 44	Surface density distribution for four randomly choosen <i>Sab</i> matched galaxies	82
Figure 45	Concentration, virial mass and spin relations for <i>Sab</i> matched sample	83
Figure 46	Concentration distribution for four randomly choosen <i>Scd</i> matched galaxies	84
Figure 47	Spin distribution for four randomly choosen <i>Scd</i> matched galaxies	84
Figure 48	Virial mass distribution for four randomly choosen <i>Scd</i> matched galaxies	85
Figure 49	Surface density distribution for four randomly choosen <i>Scd</i> matched galaxies	85
Figure 50	Concentration, virial mass and spin relations for <i>Scd</i> matched sample	86
Figure 51	Scale length, virial mass and spin relations <i>Sab</i> galaxies	86
Figure 52	Sérsic index n relations with virial mass, scale length and spin <i>Sab</i> galaxies	87
Figure 53	Scale length, virial mass and spin relations <i>Scd</i> galaxies	87
Figure 54	Sérsic index n relations with virial mass, scale length and spin <i>Scd</i> galaxies	88
Figure 55	Surface brightness parameter A from Sérsic's profile vs Stellar mass of each object	91
Figure 56	Surface brightness parameter A from Sérsic's profile vs measured redshift of each object	91
Figure 57	Surface brightness parameter A from Sérsic's profile vs Absolut magnitude in the $r - band$	92
Figure 58	Scale length parameter R_0 from Sérsic's profile vs Stellar mass of each galaxy	92
Figure 59	Scale length parameter R_0 from Sérsic's profile vs Absolut magnitude in the $r - band$	93
Figure 60	Scale length parameter R_0 from Sérsic's profile vs measured redshift of each object	93
Figure 61	n -index from Sérsic's profile in the $r - band$ vs measured redshift of each object	94

LIST OF TABLES

Table 1	General galaxy classification schemes	3
---------	---------------------------------------	---

Table 2	Spiral-type bulge-disk luminosity relation and pitch angle ranges	5
Table 3	Disk galaxy properties	6
Table 4	Spheroidal galaxy properties	6
Table 5	Properties of spiral galaxies in the Hubble classification	7
Table 6	Properties of elliptical galaxies in the Hubble classification	7
Table 7	Hubble stage T and correspondence with de Vaucouleurs scheme	8
Table 8	Form Families of the Yerkes System	10
Table 9	Relation between spectral type (morphology) and stellar central component	10
Table 10	Classification types in the DDO system	11
Table 11	Values of density parameters for specific models	20
Table 12	Sab final sample result	89
Table 13	Scd final sample result	89

THEORETICAL FRAMEWORK

1.1 INTRODUCTION

In this chapter the galaxy morphological classification system will be described. Different kinds of systems specifically the Hubble sequence, the De Vaucouleur's and other ones will be addressed to specify how Astronomers identify properties of galaxies to relate them with other physical systems as the dark matter halos. Properties of galaxies, as important as velocity dispersion, color, magnitude, surface brightness profile among others will guide us to specify the connection between the galaxy and the host dark matter halo. Later on it will be addressed the connection between properties of galaxies and parameters such as concentration and spin related to dark matter halo distributions.

A simple view of different topics will be explained as thoroughly as we can. The main aim is to connect the photometric properties of galaxies with the parameters that describe the dark matter halo. Throughout next sections a variety of issues will be discussed to clarify ideas and different points of view.

1.2 MORPHOLOGICAL CLASSIFICATION OF GALAXIES

Galaxies are a key sample when we want to know some kind of information about the Universe. They behave like little blocks building up this whole thing we call Cosmos. However, when someone talks about galaxies people could be confused, because it is not the type of objects that surround us in our daily lives. In fact, the books and journals bring us an idea of these objects which can be misleading and fuzzy. Clarifying the nature of these objects is the main task Astronomers have, or at least, for those ones who want to know more about their behavior, composition, appearance and evolution. When classifying astronomical objects one must seek quantitative information instead of qualitative impressions wherever possible, because this would lead to a wrong class of the object and a bad quality catalog.

The main aim lies in the way the scheme of galaxies is going to be constructed. How the collection of objects will be treated. Morphology plays an important role here because it will help us to recognize properties and interpret them in terms of the evolution. That was indeed what Edwin Hubble was trying to look for. A way through morphology of galaxies to give an explanation of their own evolution over time.

The way galaxies are studied is through photometric analysis. Though, there are a few problems that could arise when extracting information of the same object with different image properties. Suppose that in one hand there are two images of the same object (classified in a given system) but with different depths. Here depth and shallowness of an image refers to whether the image has been zoomed in or not. The appearance of the object is so different in both images that one may feel a degree of disbelief, because the objects could not be matched as the same one. A similar

confusion arise between images which have been taken in different bands. The features observed in some band may look conspicuous and totally vanish in the other. It is a big deal because one object could look like a barred-galaxy, for example, in some band and that outstanding feature could disappear in another one. So, this object would be a normal spiral and a barred spiral at the same time in a given classification system. In [Figure 1](#) it can be observed what has been said about morphology with objects such as NGC 628 (M74) upper panel and NGC 2841 lower panel in HI and B-band.

An important aim of these collections of objects is to put them into a library to compare each

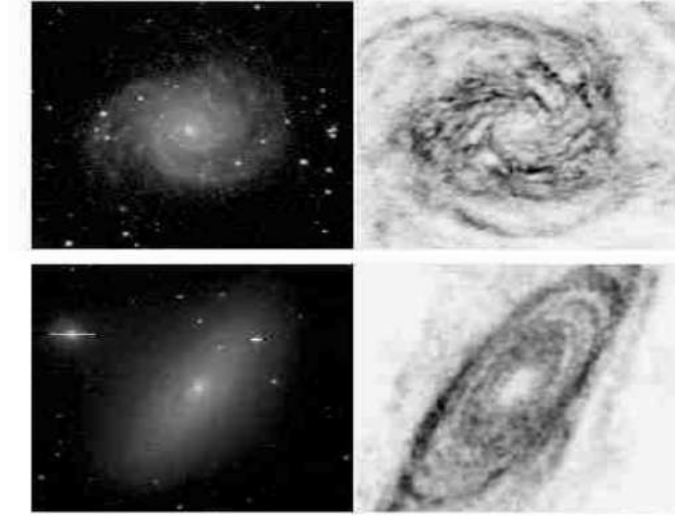


Figure 1: HI and B-band morphology for NGC 628 upper panels and NGC 2841 lower panels. It can be observed how different features can emerge when we observe in different filters. Same behavior occurs when we zoom in which sometimes is referred as depth and shallowness of an image. Here deep images are those in the right-hand and shallow ones in the left-side. [\[15\]](#)

other and then try to notice their common features. Human's brain is capable to figure out patterns and divide the entire sample into classes and split it into different characteristics that may contain intermediate type of galaxies. One may take care to avoid biased samples and collect all kind of objects to cover a wide range of galaxies to take into account all the possible types of objects. For this reason the sample should be large to ensure completeness. Moreover, color can play an important role in the classification scheme so taking images of the same object in each band might be helpful.

A fundamental consideration comes when comparing images of different objects. It makes no sense to compare a B-band image of one galaxy with a R-band image of another, nor to compare a shallow image of one galaxy with a deep one of another. A set of similar images must be available for every object to ensure the comparison between them.

It is likely that the chosen classification scheme reflects one's view as to what is physically important and what is merely important. Building these libraries is an early step so maybe some features tagged at a first time as superficial are instead fundamental however one has to deal with this kind of problems. So, the criteria used to assign a galaxy to a class should permit a unique classification in each case.

[Table 1](#) summarizes the general classification schemes used as shown by [\[9\]](#) and will be discussed along the next subsections. It shows the systems and the principal criteria used to classify galaxies,

the nomenclature and some examples of the same galaxy in every system of classification. These schemes were built with B- or photographic-band images. Hence colors do not play an

Table 1: **General galaxy classification schemes**

System	Principal criteria	Symbols	Examples
Hubble-Sandage ¹	barrishness;	E,S0,S,SB,Irr	M87 = E1
	openness of arms/disk-bulge ratio;	a,b,c	M31 = Sb
	degree of resolution of arms into stars		M101 = Sc
			LMC = IrrI
De Vaucouleurs ²	barrishness;	E,S0,S,SA,SB,I	M87 = E1P
	openness of arms/disk-bulge ratio;	a,b,c,d,m	M31 = SA(s)b
	rings or s shapes	(r),(s)	M101 = SAB(rs)cd
			LMC = SB(s)c
Yerkes ³	central condensation of light;	k,g,f,a	M87 = kE1
	barrishness/smoothness	E,R,D,S,B,I	M31 = kS5
			M101 = fS1
			LMC = aff2
DDO ⁴	young-star richness of disk;	E,S0,A,S,Ir	M87 = E1
	barrishness;	B	M31 = Sb I-II
	central condensation of light;	a,b,c	M101 = Sc I
	quality and length of arms	I,I,...,V	LMC = Ir III-IV

Notes: ¹Sandage (1961-1995), ²de Vaucouleurs (1959b), ³Morgan (1958-1970), ⁴van den Bergh (1960-1976) [9]

important role. Also they were designed to include all galaxies brighter than some given apparent magnitude or having isophotal diameters in excess of some given angular size. Most of them employ more than one classification criteria which causes that the class of a given galaxy is occasionally ambiguous.

1.2.1 Hubble's tuning-fork diagram

Edwin Hubble introduced in 1936 a classification scheme in his book "*The realm of the Nebulae*" as a first step to classify galaxies. The scheme was modified according as the collection was growing up and it has been the most widely used along decades. Later on, Sandage published "*The Hubble Atlas of Galaxies*" which is what we know as the definitive exposition of Hubble's scheme. Another one known as "*The Carnegie Atlas of Galaxies*" is a variant of the original whose only difference is that is more extensive because it includes more different types of objects.

The scheme shown in [Figure 2](#) represents the Hubble tuning-fork diagram with a little modification between elliptical and spiral types to include stages of lenticular galaxies.

Hubble suggested that the diagram was an evolution of galaxies over time. To him, galaxies evolved from the left-hand end to the right-hand end going through different stages. Even though this was a wrong idea, it has been kept alive in language used because the left-hand is still referred to as **early-type** and the right-hand as **late-type**.

On the left-hand side of the diagram are located the smooth and structureless galaxies designated

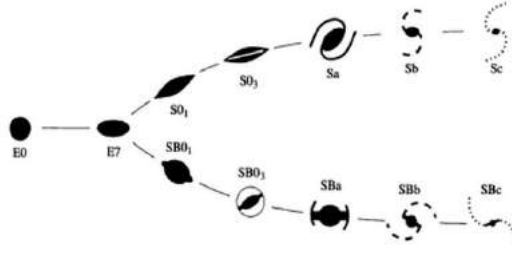


Figure 2: The Hubble tuning-fork diagram. This figure differs from Hubble's original diagram in that it shows stages of lenticular galaxies interposed between the elliptical and the spirals. Left-side region contains the elliptical galaxies and as it goes to the right lenticular and spiral types emerge. Spirals split into two branches which contains on the top the pure spirals and on the bottom the barred ones. [9]

as En , where, n describes the apparent axial ratio (b/a) through the relation $n = 10[1 - (b/a)]$. Here a and b represents the minor and major axes of an elliptic galaxy which is treated as an ellipsoid. Such type of galaxies are known as **Ellipticals**. Then, if the galaxy looks round-like, it is assigned an E0 class, while if it is elongated belongs to an E6 class. As ellipticity increases objects flatten, while if it decreases they are rounded.

Most elliptical galaxies have a low luminosity, called **Dwarf Elliptical** (dE). Another kind of these objects are characterized by having a low star density and an appearance of mere clustering of faint stars belonging to a class known as **Dwarf Spheroidal**. Ground-based telescopes cannot detect them if they lie significantly outside of the Local Group.

After elliptical galaxies the Hubble's diagram bifurcates into two branches called the normal and the barred galaxies both types belonging to a same class known as **Spirals**. Misclassification is really common because bar-like features may be lost on small-scale plates and when they are nearly edge-on.

Normal Spirals (**S**) are comprised by a central brightness condensation which resembles an elliptical, located at the center of a thin disk containing the spiral arms. However Barred Spirals, (**SB**) have interior to their spiral arms a bar, containing often dark lanes believed to be produced by absorption of light by dust. The spiral arms often emanate from the ends of the bar. Not all the objects fit into these two types so there is a sub-division taking into account next three criteria:

- Importance of the central luminous bulge and the outlying disk respect the overall light distribution.
- Tightness with which the spiral arms are wound.
- Degree to which the spiral arms are resolved into stars and individual emission nebulae (HII regions).

Regular spirals and barred subdivide into different types with specific features. In general their masses are between $(10^{10}-10^{12}) M_{\odot}$, luminosity between $(10^8 - 10^{11}) L_{\odot}$, blue absolute magnitude between $(-16, -23)$ and diameters measured over extension of starlight between 5 – 100 kpc. First of all, $Sa-SBa$ objects on the left-hand side branch of spirals of the Hubble's diagram are characterized by having large bulges, to be tightly wound and have smooth arms. Most of their stars are G-K types, approximately 5% of their luminous mass is in the form of gas so they have

low star formation. On the other hand there are *Sc-SBc* galaxies in the right-hand side of the branches which are distinguished by their small central brightness condensations, loosely wound and highly resolved arms. Most of their stellar component are A spectral type and approximately 20% of their luminous mass is in the form of gas so their star formation is moderately high. Finally in the middle of the branches we find *Sb-SBd* objects. They have intermediate central condensation and tightness. Mostly build up of F-G stars where 10% of their luminous mass is in the form of gas. Spiral galaxies are a mix of population I and II stars, where disk is supported by relatively rapid rotation, but spheroid is puffed up by random motions. After this, depending on how the object looks like it can be set into a regular family described by (Sa,Sab,Sb,Sbc,Sc) or a barred-like family (SBa,SBab,SBb,SBbc,SBc).

In [Table 2](#) there are some important quantities as the pitch-angle and the relation between bulge and disk for spiral galaxies which help us to define more rigorously differences between galaxies of this specific type. The pitch angle is defined as an angle between a tangent to the spiral arm and a tangent to a circle centered in the bulge which crosses the arm in its large curvature point. This angle gives us a measure of how tightened are the spiral arms of a galaxy. Furthermore, the relation between bulge and disk luminosity L_{bulge}/L_{disk} gives us an estimate of which one is larger in size whether the bulge or the disk.

At the junction of ellipticals and spirals there is a class of galaxies called **Lenticular** galaxies

Table 2: **Spiral-type bulge-disk luminosity relation and pitch angle ranges**

Spiral Type	L_b/L_d	Pitch Angle	Interpretation
<i>Sa-SBa</i>	~ 0.3	$\sim 6^\circ$	Large bulge, tight arms
<i>Sb-SBb</i>	> 0.1	$\sim 12^\circ$	Intermediate bulge and tightness
<i>Sc-SBc</i>	~ 0.05	$\sim 18^\circ$	Small bulge, open spiral arms

(S0 or SB0), if they are barred or not. Lenticular galaxies are characterized by a smooth central brightness condensation with their outermost parts tending to be very flat. They are subdivided into three types (S0₁,S0₂,S0₃) according to the strength of dust absorption within their disks. S0₁ shows no signs of absorption by dust while S0₃ shows a completely dark band within their disks around their elliptical components. S0₂ is an intermediate kind. When classifying barred types, dust absorption is not taken into account but the prominence of the bar. So they could be (SB0₁,SB0₂,SB0₃). SB0₁ shows a bar, composed of two broad regions of slightly enhanced brightness on either side of the central bulge while SB0₃ expose a narrow and well defined bar, extending completely across the lens. In the case of SB0₂, it has an intermediate prominence.

Following, Hubble non-symmetrical galaxies can belong to Irr-I and Irr-II types. Irr-I display bright knots containing OB associations, "well" defined arms and a lack symmetry while, Irr-II are non-symmetrical objects which frequently display dust lanes.

In [Table 3](#) and [Table 4](#) we present the main characteristic ranges of properties for disks and spheroids in general. For disks some properties are shown as mass, luminosity, mass-luminosity relation, radius, form, scale length, velocity dispersion, metallicity and age for the neutral gas, thin and thick disks which are the main constituents. In the case of spheroids same properties but this time for central bulge, stellar halo and dark-matter halo. In [Table 5](#) and [Table 6](#) there are more properties for distinct spiral and elliptical subclasses as classified in the Hubble sequence.

Properties are given for (*Sa,Sb,Sc*) early spirals and (*Sd/Sm*) late spirals and (*Im/Ir*) irregular galaxies. In the table for ellipticals (*cD, E, S0/SB0*) are cD-type, ellipticals and lenticular galaxies respectively, while (*dE, dSph*) are dwarf elliptical and spheroidal galaxies. We can find there properties as absolute magnitude in blue band M_B , total mass, luminosity relation, diameter, mass-luminosity relation, maximum velocity, pitch angle, color (B-V), gas to total mass ratio and molecular to neutral hydrogen mass ratio.

De Vaucouleurs argued that Hubble's classification of spiral was incomplete and that his

Table 3: **Disk galaxy properties**

Property	Neutral gas	Thin disk	Thick disk
$M(10^{10} M_{\odot})$	0.5	6	0.2 to 0.4
$L(10^{10} L_{\odot})$	—	1.8	0.02
M/L_b	—	3	—
Radius (kpc)	25	25	25
Form	exponential e^{-z/h_z}	exponential e^{-z/h_z}	exponential e^{-z/h_z}
Scale Length (kpc)	< 0.1	0.35	1
$\sigma_w (kms^{-1})$	5	16	35
$[Fe/H]$	> +0.1	−0.5 to +0.3	−2.2 to −0.5
Age (Gyr)	$\lesssim 10$	8	10

Note: Table was partially reproduced from [13]

Table 4: **Spheroidal galaxy properties**

Property	Central Bulge	Stellar Halo	Dark-Matter Halo
$M(10^{10} M_{\odot})$	1	0.3	190
$L(10^{10} L_{\odot})$	0.3	0.1	0
M/L_b	3	~ 1	—
Radius (kpc)	4	> 100	> 230
Form	boxy with bar	$r^{-3.5}$	$(r/a)^{-1}(1+r/a)^{-2}$
Scale Length (kpc)	0.1 to 0.5	3	170
$\sigma_w (kms^{-1})$	55 to 130	95	—
$[Fe/H]$	−2 to 0.5	< −5.4 to −0.5	—
Age (Gyr)	< 0.2 to 10	11 to 13	~ 13.5

Note: Table was partially reproduced from [13]

treatment of irregular galaxies was quite inadequate. In particular because spiral class does

Table 5: **Properties of spiral galaxies in the Hubble classification**

Property	<i>Sa</i>	<i>Sb</i>	<i>Sc</i>	<i>Sd/Sm</i>	<i>Im/Ir</i>
M_B	−17 to −23	−17 to −23	−16 to −22	−15 to −20	−13 to −18
M_\odot	$10^9 - 10^{12}$	$10^9 - 10^{12}$	$10^9 - 10^{12}$	$10^8 - 10^{10}$	$10^8 - 10^{10}$
$(L_{bulge}/L_{total})_B$	0.3	0.13	0.05	—	—
Diameter (D_{25} , kpc)	5 – 100	5 – 100	5 – 100	0.5 – 50	0.5 – 50
M/L_B (M_\odot/L_\odot)	6.2	4.5	2.6	~ 1	~ 1
V_{max} ($km s^{-1}$)	299	222	175	—	—
V_{max} range ($km s^{-1}$)	163 – 367	144 – 330	99 – 304	80 – 120	50 – 70
Pitch Angle	$\sim 6^\circ$	$\sim 12^\circ$	$\sim 18^\circ$	—	—
(B-V)	0.75	0.64	0.52	0.47	0.37
M_{gas}/M_{total}	0.04	0.08	0.16	0.25 (<i>Scd</i>)	0.5 – 0.9
M_{H_2}/M_{H_I}	2.2 (<i>Sab</i>)	1.8	0.73	0.03 – 0.3	~ 0

Note: Table was partially reproduced from [13]

Table 6: **Properties of elliptical galaxies in the Hubble classification**

Property	<i>cD</i>	<i>E</i>	<i>S0/SB0</i>	<i>dE</i>	<i>dSph</i>
M_B	−22 to −25	−15 to −23	−17 to −22	−13 to −19	−8 to −15
M_\odot	$10^{13} - 10^{14}$	$10^8 - 10^{13}$	$10^{10} - 10^{12}$	$10^7 - 10^9$	$10^7 - 10^8$
Diameter (D_{25} , kpc)	300 – 1000	1 – 200	10 – 100	1 – 10	0.1 – 0.5
M/L_B (M_\odot/L_\odot)	> 100	10 – 100	~ 10	~ 10	5 – 100

Note: Table was partially reproduced from [13]

not do justice to the great variety of morphologies of real galaxies. He proposed an elaborated classification and extended the prongs of Hubble's tuning-fork with another classes. In the next subsection De Vaucouleurs classification system will be thoroughly explained.

1.2.2 De Vaucouleurs' system

In 1959 de Vaucouleurs proposed a modified Hubble classification system with the aim to fit all galaxies with their morphological characteristics. New types of galaxies emerged like Sd, Sm and Im. Objects such as Sd overlaps with Sc type of Hubble classification but now containing extreme objects which are classified as Irr-I. The Sm and Im contains the remaining Irr-I galaxies and the "m" stands for 'Magellanic' because the LMC is classified as SBm. Other kind of objects were introduced to guarantee intermediate stages as E^+ intermediate galaxies between ellipticals and lenticulars, $S0^-$ structureless lenticular galaxies only distinguishable from ellipticals with a detailed study, $S0^0$ lenticulars with some kind of structure, $S0^+$ intermediate between lenticular and Sa type and "Pec" to denote peculiar for unclassifiable galaxies. Another feature taken into account by de Vaucouleurs was the bar. If a galaxy has no bar, it is classified as SA to match

SB types in the Hubble sequence while if it is weakly barred turns into SAB or a SB if the bar is conspicuous. If one cannot say whether it has a bar or not it is designated lenticular S0.

Barred galaxies have an extra feature in this system concerning the ring-like structures. According to a relation between the radius of a ring structure denoted by r and the bar's semimajor axis a given by r/a in this system we are able to say if rings are an important feature or if the objects keep on being conformed by purely spiral arms. They can be **nuclear**, **inner** or **outer**. It will be nuclear if $r/a < 1$, inner if $r/a \approx 1$ and outer if $r/a > 1$. De Vaucouleurs uses the symbols (r), (s) and (rs) to indicate systems with or without a ring or an intermediate type. it is worth to note here that (r) is just a convention which is independent of the radius of the ring structure r . In [Figure 3](#) it is shown three different galaxies classified in this system which exhibits structures mentioned above.

The de Vaucouleurs systems is interpreted as a three dimensional diagram. One dimension resembles a modified Hubble's system, a second dimension concerning barred features and the last one about the rings. In [Figure 4](#) one can observe the scheme proposed by de Vaucouleurs.

The line along E and Im is related to color and stellar population ages. A problem arises

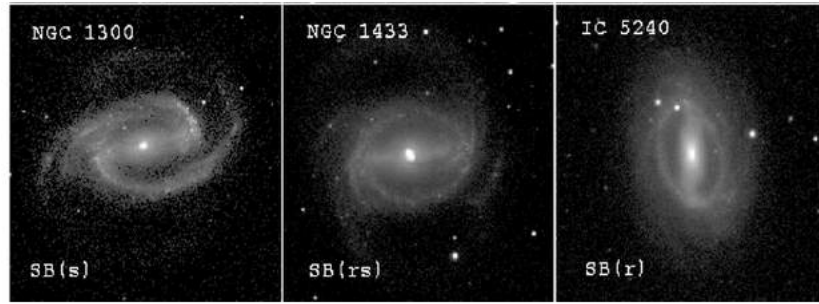


Figure 3: Examples of galaxies having different families and varieties in the de Vaucouleurs revised Hubble classification system. NGC 1300 presents a purely spiral structure, NGC 1433 is an intermediate and IC 5240 shows a ring structure. [\[5\]](#)

because along Sc-Sd-Sm sequence galaxies turn less luminous and bluer, leading to a fictitious entanglement between evolution and luminous effects. To the system is added a parameter T which helps to correlate integrated colors and associate it to the line across E and Im. [Table 7](#) indicates the correspondence between the Hubble and the de Vaucouleurs schemes and also defines the numerical Hubble stage T .

Table 7: Hubble stage T and correspondence with de Vaucouleurs scheme

Hubble	E	E-S0	S0	S0/a	Sa	Sa-b	Sb	Sb-c	Sc	Sc-Irr	Irr I
de Vaucouleurs	E	S0 ⁻	S0 ⁰	S0 ⁺	Sa	Sab	Sb	Sbc	Scd	Sdm	Im
T	-5	-3	-2	0	1	2	3	4	6	8	10

Note: The table was taken from [\[9\]](#)

1.2.3 Yerkes or Morgan's system

The galaxy classification system proposed by Morgan (1958,1959a) which is sometimes referred to as the Yerkes system, is a one-dimensional system based on central concentration of light. The arrangement of galaxies apparently correlates with the stellar content of the inner parts of the

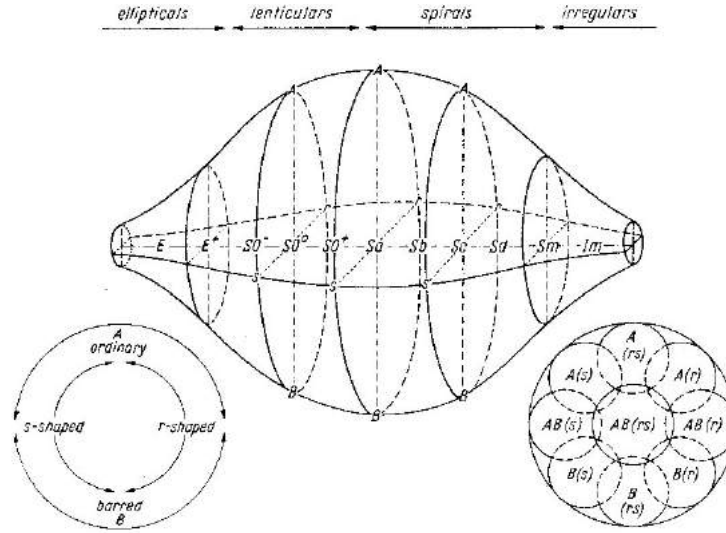


Figure 4: De Vaucouleurs' three dimensional representation of the revised classification scheme and notation system. From left to right are the four main classes: ellipticals E, lenticulars S0, spirals S and irregulars I. Above are the ordinary families SA, below the barred families SB; on the near side are the S-shaped varieties S (s), on the far side the ringed varieties S (r). [16]

galaxy as judged by integrated spectral types. Morgan arranged galaxies in a sequence a-f-g-k depending on the central concentration of light of the object where *a* are galaxies with little or no central concentration of light and *k* show the most extreme central concentration of light which corresponds to giant ellipticals and spirals. Also the Yerkes system allows intermediate types classified as 'af', 'fg' and 'gk'. Galaxies with Morgan type *a* tend to have early-type (A) spectra, whereas type *k* mostly exhibit late-type (K) spectra. That is why the Morgan's system contains information about the state of stellar evolution in the central regions of the galaxies. There is a link between morphology and spectral type, then centrally concentrated galaxies shows a dominant stellar old population while low concentrated tend to have a strong young population component [23].

Morgan's system recognizes standard forms from Hubble's system as *E* (Elliptical), *S* (Spiral), *SB* (Barred Spiral) and *Irr* (Irregular) but there are new categories like *L* (Low surface brightness) and *N* (Objects with bright nuclei superposed with a fainter background). This last one could stand for quasars, objects with active nuclei or centrally concentrated starburst galaxies. A *D* class was added comprising rotationally symmetrical galaxies without a pronounced spiral or elliptical structure. In this classification system exists an index which accounts for the apparent position of galaxy namely if it is edge-on or face-on going from seven to one. For example, a complete tagged galaxy on this system could look like *kE6* which means an object highly flattened centrally concentrated and elliptical or *afS1* a face-on spiral with a low concentration. Other subclass added to *D* galaxies were included by Matthews, Morgan & Schmidt (1964) and Morgan & Lesh(1965) called *cD*. Here "c" comes from early spectroscopists notation to denote narrow-lined supergiant stars. Most of these galaxies are located close to the center of rich clusters.

In Figure 5 one can observe a simplified diagram of the Yerkes or Morgan's classification system of galaxies.

Finally, Morgan's system can be reduced to the next families presented in Table 8 and the spectral type can be related to their stellar central component as shown in Table 9.

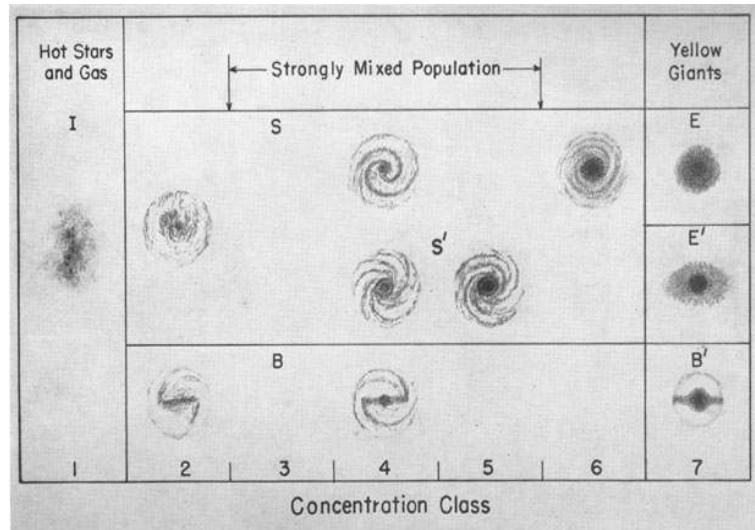


Figure 5: Simplified Yerkes classification system (Y') for galaxies. Diagram by J. W. Tapscott. [24]

Table 8: **Form Families of the Yerkes System**

Form family	Description
B	Barred spirals
D	Galaxies with rotational symmetry but showing neither spiral structure nor ellipticity
cD	Supergiant <i>D</i> galaxies, predominantly found in clusters and embedded in an extensive halo
db	Dumb-bell systems
E	Ellipticals
Ep	Peculiar ellipticals containing conspicuous absorption patches
I	Irregulars
L	Low-surface-brightness systems
N	High-luminosity nucleus superimposed on a considerably fainter outer envelope
Q	Quasi-stellar objects
S	Ordinary spirals

Note: Table was taken from [6]

Table 9: **Relation between spectral type (morphology) and stellar central component**

Spectral type	Description
a	Prominent A stars
af	Prominent A-F stars
f	Prominent F stars
fg	Prominent F-G stars
g	Prominent G stars
gk	Prominent G-K stars
k	Prominent K stars

1.2.4 DDO or Van den Bergh's system

By inspecting Palomar Sky Survey prints, Holmberg (1958) and Van den Bergh (1959,1966) noticed that dwarf galaxies presented low-superficial brightness opposite to giants. They compiled a set of objects (243 in total) into a catalog known as 243-DDO. Analysing the plates Van den Bergh noticed that the appearance of spiral arms was a step function of the absolute luminosity of

galaxies. The larger the luminosity then the longer and most developed the arms, whereas fainter the systems the poorest developed the arms. By inspecting the character of the spiral arms Van den Bergh was able to divide *Sb* types into five luminosity classes (I, I-II, II, II-III and III) by analogy with the Morgan's system. The *Sc-Irr* systems could be divided into eight half-classes (I to V with intermediates).

The Hubble classes *Sa, Sab, Sb, Sbc* and *Sc* were only applicable to giant, bright giant and supergiant spirals. For sub-giants it is only possible to assign types S^- (early) spirals with smooth structure, *S* (intermediate) and S^+ (late) spirals highly resolved. The symbols + and - divide the Hubble sequence more finely. Following the nomenclature, if the object has a presence of a strong bar it is added a *B*, whereas if the bar is weak is tagged by (*B*). In this system if a galaxy belongs to *S*, *S(B)* and *SB* can be matched respectively with de Vaucouleurs to *SA*, *SAB* and *SB*. Other symbols as '*' are used to denote patchy arms and *n* for nebulous or smooth arms. Tidal distortion is indicated by *t* or if the object belongs to an extreme case called by Van den Bergh 'anemic' a double symbol is used, then in this case, '*', *n* and *t* turns into '**', *nn* and *tl*. The system is two-dimensional, retains a, b and c Hubble types as a division along a linear sequence and adds the luminosity class as the second parameter. In Table 10 one can find the types of galaxies in the DDO system based on inspection of galaxies in blue light.

DDO system was mainly based on morphology of outer regions of galaxies. Van den Bergh

Table 10: **Classification types in the DDO system**

Sa I	Sab I	Sb I	Sbc I	Sc I	
Sa I-II	Sab I-II	Sb I-II	Sbc I-II	Sc I-II	
Sa II-III	Sab II	Sb II	Sbc II	Sc II	
Sa III	Sab II-III	Sb II-III	Sbc II-III	Sc II-III	Ir II-III
Sa III-IV	Sab III	Sb III	Sbc III	Sc III	Ir III
		Sb III-IV		Sc III-IV	Ir III-IV
	S^- IV	S IV	S^+ IV		Ir IV
	S^- IV-V	S IV-V	S^+ IV-V		Ir IV-V
	S V		V		Ir V

Note: Table was taken from [30]

proposed a preliminary classification for inner regions of galaxies. New categories are included as NN (no nucleus) for galaxies that appear to contain no nucleus, N (nucleus) shows a star-like nucleus, SSN (semi-stellar nucleus) having semi-stellar nuclei, CB (central bulge) characterized by a small bright central bulge or disk, NB (nuclear bar) in the galactic center presents a nuclear bar-like structure, and Tr (transitional) those intermediates between spirals which have central bulges and objects with central regions resolved into stars and knots.

A diagram comparing Hubble's sequence and Van de Bergh's proposed classification system is shown in Figure 6.

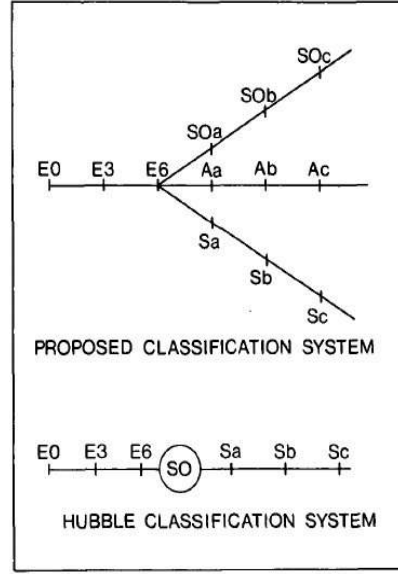


Figure 6: Comparison between Hubble (1936) classification system for ordinary spirals and for a system (van den Bergh 1976 b,c) in which anemic galaxies are postulated to be intermediate between lenticular (S0) galaxy and ordinary spirals. The latter classification system has been called the "trident diagram". [30]

1.2.5 The Color-Magnitude diagram (CMD)

An alternative way of classifying galaxies comes from the Color-Magnitude diagram (CMD). Galaxies do not split into the multiple families as in the Hubble's sequence or in the other classification systems shown above. The only feature that matters here is the color of an object and its magnitude. Then the classification is made taking into account a division by colors, so one could figure out a group of galaxies belonging to the same class by just assigning a color range.

The color of a galaxy is, on average, well correlated with its structural type. Early-type galaxies (E/S0) show a correlation between their colors and luminosities (or masses), brighter objects tend to be more massive and redder while fainter ones look less massive and bluer. CMD supply a convenient and informative display of several properties for different galaxy types. The y-axis contains the color which simply is a measure obtained from the difference of magnitude of a galaxy in two different regions of their spectra. In this particular case a difference between two petrosian magnitudes, one g around 4686\AA (blue region) and other r around 6165\AA (red region). Hence, $(g - r)$ is the color. Along the x-axis there is located the absolute magnitude of the object in the r band. The absolute magnitude (a measure of luminosity) is given by the whole galaxy spectrum together with the emission and extinction properties of the interstellar matter. Unlike the comparable Hertzsprung-Russell diagram for stars, galaxy properties are not necessarily completely given by their location on the color-magnitude diagram, but it shows considerable evolution through time.

An example presented by [17] is shown in Figure 7 corresponding to CMD for petrosian magnitudes g and i against absolute magnitude i corrected by cosmology.

Galaxies in the CMD falls into three distinct regions on it which are linked to their evolution.

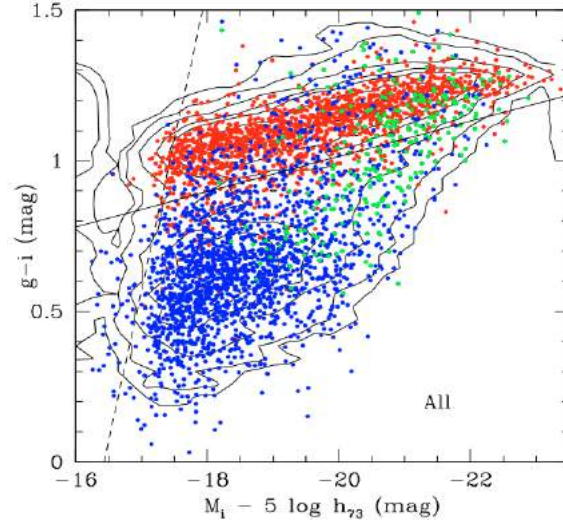


Figure 7: Color-Magnitude diagram for petrosian magnitudes g and i against absolute magnitude i corrected by cosmology. Image was taken from [17]

These three main features are known as the red sequence, the green valley and the blue cloud. The reddest objects according to the color are up in the diagram whereas the bluest are at the bottom. Bigger/brighter to the right and smaller/fainter to the left. The red sequence contains most red galaxies which are generally elliptical. Blue galaxies tagged as spirals, lie on the blue cloud. In between one can find a region known as green valley which contains early-type and late-type galaxies. Late-type galaxies lying on the green valley are thought to be objects where star formation has been quenched due to their gas shut off and exhaustion of their gas reservoirs while early-type are those where gas supplies and reservoirs were consumed so quickly. The CMD does not give specific information about all the possible features needed to classify a galaxy into some kind of class as those shown by the different galaxy classification system. But it is useful to notice global features of early-types and late-type objects and correlate them with their evolution stage.

1.3 PROPERTIES OF GALAXIES

Once astronomers applied the rules to classify galaxies in some kind of system, they started to look for some important properties that could be measured to answer the questions about their evolution and function in the Universe. Obtaining properties of these objects was essential as a first step to describe the physics of galaxies.

The classification proposed by Hubble shows a strong correlation with the dominance of central bulge, surface brightness and colors. In fact, properties are related among them such as metallicity, emission-line strength, luminosity in visual bands, neutral gas content, and the winding angle of spiral structure [12]. Important physical differences exist between the types of galaxies and since morphology is a powerful tracer of the structure of the galaxy those differences in properties are likely related with different evolutionary tracks. It is well known that elliptical galaxies appear redder, with high velocity dispersion, old stellar populations and a small fraction of gas while spirals are more gas-rich and have young stellar populations. Those features are intrinsically contained in the different classes of a given morphological classification and are

trends that astronomers know well. Properties of galaxies are helpful in order to understand theoretically how galaxies formed and acquired their current properties. Knowing exactly why they look today the way they do, helps to build a solid theory where physical parameters are related with the observational data (properties). All objects exhibit a wide range of features but they can be globally put into a few classes helping the understanding of their nature.

Some properties of galaxies will be described in this section to better understand how a given property relates with some physical phenomena and with the morphology of the object. All the physical parameters described belong to the Hubble sequence, and concerned to describe properties that are important for this work. It must be noticed the presence of two distinct categories of galaxy parameters. First of all those that measure the absolute scale as size, luminosity and mass, and those that describe more its morphology.

1.3.1 *Optical colors, luminosities and linear size*

Holmberg in 1958 took 300 galaxies to analyze their integrated magnitudes, colors and diameters. He found a strong correlation between the color and the morphological type of galaxy. The color indices (B-V) and (U-B) showed clearly differences for every type of object. The E and S0 galaxies which lie on the elliptical family are redder than spiral types and the trend from redder to bluer tend to be monotonic. In fact colors among Sa type overlaps those of the Sc type, where it is clear to see how the Sa sample can contain galaxies as blue as some Sc and how Sc sample can contain galaxies as red as some Sa [27].

The colors of galaxies depend strongly on luminosity, in the sense that more luminous galaxies are redder while bluer are fainter. It becomes evident in the Color-Magnitude relation for $(g - i)$ shown before, where blue and red objects are separated. Elliptical galaxies are slightly brighter than spirals because the optical luminosity is a scale parameter which slightly varies and only becomes clearly apparent when galaxies are contrasted with dwarfs.

Another property related with the size is the optical linear size and it also is a scale property as luminosity. The most evident feature is that the size is small for the late-type and large for early-types.

1.3.2 *Optical surface brightness: Galaxy profile shape and surface brightness*

Holmberg included photometric parameters with which he study the surface brightness of galaxies and internal extinction. The distribution of the surface brightness Σ_B is nearly constant for E,S0 and classical spiral galaxies but clearly different from dwarfs as Sm and Im. Maybe that constancy found across most of the classical galaxy sequence by [27] is because their catalog selection (biased against systems of low surface brightness).

The surface brightness can be expressed as a radial dependence profile. As proposed by Sérsic in 1968:

$$I(r) = A \exp[-(r/r_0)^{1/n}] \quad (1.1)$$

Late-type galaxies are those which have Sérsic index $n \sim 1$ with a nearly exponential profile

and early-type the ones with Sérsic index $n \sim 4$ showing a de Vaucouleurs profile. An important parameter at this time is the Petrosian inverse concentration index $1/c \equiv r_{50}/r_{90}$ where, r_{50} is the radius containing half the Petrosian flux and r_{90} that containing 90% of the Petrosian flux. It turns out that highly luminous galaxies are more concentrated and thus have large Sérsic index than their counterparts the lower luminous. For blue galaxies which are close to Sérsic index $n \sim 1$, n is independent of luminosity but for red galaxies is a strong function of luminosity.

At low luminosities, surface brightness and luminosity are well correlated but when luminosity turns extremely large, surface brightness declines as a function of luminosity. This occurs because highly concentrated galaxies which are indeed more luminous have low surface brightness, while low luminous galaxies such as those with an exponential profile have large surface brightness. Then, for galaxies with an exponential profile surface brightness increases as a function of luminosity but for the most bright galaxies (more concentrated) it decreases [12]. It is worth to note that for all type of galaxies, size increases with luminosity. In Figure 8 is summarized the behavior of surface brightness, size and concentration as a function of luminosity for spiral and elliptical galaxies.

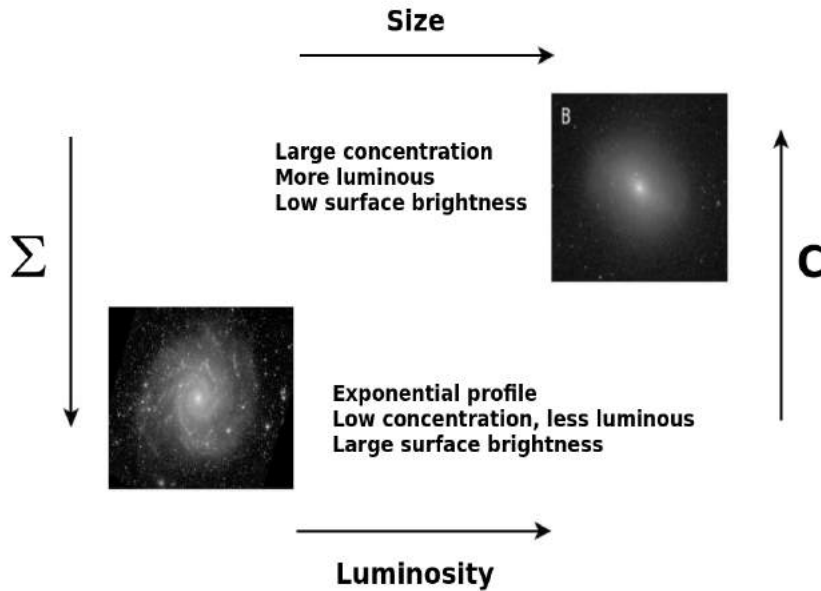


Figure 8: Surface brightness (y-axis left side), size (upper-side) and concentration (y-axis right side) as a luminosity (x-axis) function. Spiral galaxies are lower luminous than ellipticals and smaller but with large values of surface brightness. In the left-bottom corner where luminosity is pretty small and surface brightness is quite high both quantities are well correlated. Images were taken from [15] where the spiral galaxy at the bottom is NGC 628 and the elliptical at the top is NGC 584.

1.3.3 Far infrared emission

Far infrared (FIR) flux measurements show a clear distinction between elliptical and spiral galaxies. Elliptical galaxies generally appear with both low FIR luminosity and ratio L_{FIR}/L_B and also a poor detection rate. As explained by [27] the possible origins of FIR radiation are commonly:

- Dust can be heated by nearby young, massive stars which can reradiate in the infrared.

- Dust reradiating the heating by the general interstellar radiation field e.g. the Galactic cirrus cloud population.
- Thermal and/or nonthermal radiation from active galactic nuclear regions e.g. Seyfert galaxies.

If the dominant dust-heating source are the massive stellar populations as O-B stars the FIR is a good measure of star formation. A strong correlation between FIR and radio radiation for spirals can only be explained through massive stars as a heating mechanism but for elliptical galaxies no correlation is found.

1.3.4 *Radio continuum emission*

The radio continuum radiation can be emitted from two particular places in a galaxy. One within a nuclear or central region that may exhibit various levels of substructure as jets and knots and other one from a more extended region that also could present structure. In normal galaxies there are two possible mechanisms for the production of radio continuum radiation. The first one is through synchrotron radiation produced by relativistic electrons which are accelerated by supernova remnants and a second mechanism from free-free radiation from HII regions. Other mechanism that is only significant when the wavelengths < 1 mm comes from heated dust by starlight.

Many nearby early-type galaxies are radio-loud but most are of very low radio luminosity. When comparing radio emission with FIR for late-type galaxies a clear correlation is obtained but not for all ellipticals and just poorly for S0s. The reradiation from dust is associated to dust located near sites with active star formation while the synchrotron is a result from this active massive star formation.

1.3.5 *X-ray emission*

Most of the understanding of X-ray properties of galaxies comes from results of *Einstein Observatory* measurements. X rays have been detected for all type galaxies but for low luminosity dE and dS0 classes. The ratio between optical blue and X-ray flux varies with galaxy type. The X-ray luminosity for E and S0 galaxies varies as the square of their blue luminosity with large dispersion. Late-type objects show however a linear dependence with large dispersion.

Two distinct mechanisms are associated with the non-nuclear radiation. A pure stellar origin such as supernova remnants and X-ray binaries and a diffuse emission from hot gas at 10^6 - 10^7 K. In spiral galaxies the constituents can be both stars of population I and II: supernova remnants and high mass X-ray binaries and population II for low-mass X-ray binaries. For the early-type galaxies the principal source is the million degrees gas. Its origin comes from the mass lost by evolving stars, stars which in the bulge component of early-type systems have random motions of few hundred km s^{-1} . X-rays are seen from all galaxy types with the properties of radiation dependent on the fraction of the population types in each galaxy [27]. The variation is clarified by brighter elliptical galaxies which have large luminosities in soft X-rays and by the bright spirals having lower luminosity, harder X radiation.

1.3.6 Neutral Hydrogen Mass and Content

The 21 cm line has always been a useful tool to measure the content of neutral hydrogen (HI) and redshifts of galaxies. Neutral hydrogen HI is mainly present in disk galaxies. When analyzing the total HI content a few quantities are generally used: the total HI mass M_{HI} , the ratio M_{HI}/L_B and the HI surface density σ_{HI} . Furthermore, HI is a property which characterizes the disk so its main contribution comes from this however L_B has contributions from both the disk and the bulge so the morphological dependence of M_{HI}/L_B is quite complicated.

A feature related with the M_{HI} is that early-type galaxies as E and S0 contain lower HI masses relative to late-type spirals. Moreover, the HI content within S0s is found in an annulus exterior to the optical disk suggesting that the HI gas has an external origin maybe because tidal interactions or infall of material from a companion. A mechanism that could be responsible is the slow but close prograde tidal encounters that can finally remove a galaxy's interstellar HI content.

1.3.7 HII regions

In 1960, Sérsic produced the first quantitative description of HII regions (regions of ionized hydrogen) for a galaxy type range of *Sa-Im* and relating those features with galactic morphology. The next properties of HII regions are related to the morphological type:

- In late-type systems their brightest HII regions are on average ~ 50 times more luminous than the brightest HII regions in early-type spirals. Also, the number of bright HII regions expressed as a surface density is smaller for early-type spirals (Sab-Sb) and larger for (Sm-Im).
- To a given absolute magnitude in late-type systems, HII regions diameters are large.
- Late-type systems show a shallower slope of the luminosity functions for HII regions.

All of these trends indicates that the star-formation rate is given or related to the galaxy type, as noted in [27].

1.3.8 Chemical abundances

Measurements of chemical abundances exhibits a relationship between chemical abundance and other galactic parameters. O/H values are derived from emission line strengths measured in HII regions. A main trend is that the less massive, fainter and later-type galaxies are lower in O/H. Using absorption lines and colors it is found lower Fe values in fainter galaxies and a strong correlation between Fe/H in Es and S0s systems and luminosity. An smooth extension of the faint end of the abundance-luminosity relation is formed by dwarf elliptical and spheroidals regarding the O/H and Fe/H abundances.

The following tendencies emerge when abundances are taken into account:

- The lowest abundances (O/H or Fe/H) characterize the less luminous and less massive galaxies. Central regions of spirals and ellipticals (massive and luminous) galaxies are overabundant in heavy elements with abundances near to the solar.

- Most galaxies show an abundance gradient in the sense of lower metallicity in the outskirts. Early-type galaxies have shallower [O/H] gradients than do late-type.
- Among spirals and irregulars, earlier galaxies have higher abundance, a trend that reaches a constancy among the early spirals.

1.3.9 *Total Masses and Related Quantities*

The determination of total masses can be approached from two different techniques; Galaxy rotation curves and global HI profile widths. Along the spiral sequence from Sa to Im, the maximum rotational velocity decreases as if the morphological type could be understood as sequence of angular momentum at constant mass as noted in an early work performed by Brosche in 1971.

A small variation in total mass with luminosity and size was found by [24] among the classical spirals whereas dwarf systems show a pronounced decrease. The total mass surface density decrease along the spiral sequence from Sa to Sd. When studying the dark matter distribution, HI rotation curves are suitable since they extend beyond the point H_α is detected and thus better constrain the halo distribution. An evident feature from this analysis is that large elliptical galaxies contains substantial amounts of dark matter in contrast with spirals.

1.3.10 *Global Properties: the effect of environment*

Most properties described above as total mass surface density, HI surface density, HI mass to luminosity ratio, color and HII region luminosity have as aim to describe the star-formation in different type of galaxies. Through color one can measure the past and current star formation activity, HII regions relate current activity and the cool gas content measure the future reservoirs for star formation. Clearly, the morphological sequence of normal, isolated galaxies somehow measures the star-formation activity.

The strongest differences between galaxies of different morphological types are seen in clusters because the segregation and interactions with other members and their surroundings take place here. Dressler in 1980 quantified the concept of morphological segregation showing a decrease in spiral fraction and an increase of E/S0 population with local galaxy density. Thus, early-type galaxies are more clustered.

When galaxies are immersed in high density environments their shape can be altered, so their morphology changes. This can be produced by: galaxy-galaxy, galaxy-cluster and galaxy-intracluster interactions. In loosely groups, where the velocity dispersion is low, slow close prograde tidal encounters can remove significant fractions of a galaxy's interstellar material. Both, radio emission and FIR emission are then strongly enhanced in the instance of tidal interactions.

1.4 GALAXY FORMATION THEORY

Much of early work on galaxy evolution and formation was focused on understanding galaxies and answering questions of Cosmology. A successful galaxy formation theory must be able to explain what are the most important properties of these objects. It should be able to show how the luminosity and color of an isolated object evolve. Why the Universe is plagued of galaxies instead of a vast uniform ocean of stars?. What can we learn about our own system (the Milky Way)? in a

sense of formation and dynamical history. What is the physical origin of the fundamental plane of elliptical galaxies and the Tully-Fisher law for disk galaxies?. Galaxy formation theory should answer all of these questions through the physical history of galaxies. The goal is to describe how simple physics gives rise to a complicated set of phenomena which galaxies encompass.

Stellar dynamics play a central role in formation of galaxies and their characteristics, but to answer the questions a wide range of physics that extends beyond stellar dynamics has to be understood. External processes as mergers and internal as star formation, active galactic nuclei among others determine their gross properties and evolution. As seen before, properties of galaxies are strongly correlated among each other as the colors and gas contents with the Hubble type and luminosities. Then, this theory must help us to understand and explain these correlations.

Galaxy formation theory has been built up within the cosmological framework provided by the cold dark matter paradigm for structure formation. The structure formation tries to explain all the emergence of stars, galaxies, clusters and inhomogeneities from the nearly homogeneous early Universe. Understanding the dark matter (non-baryonic matter) distribution is essential for explaining the behavior of baryons (normal matter) which contributes to the 15% of the cosmic matter density. The remaining ~85% of non-baryonic matter is the not so well known dark matter which is believed to have no strong or electromagnetic interactions. Thus, at first approximation the contribution of baryons to gravitational forces involved in the galaxy formation can be neglected without the complications of the baryonic physics (radiation, fluid dynamics, star-forming etc ...).

Along the next sections will be discussed different mechanics that affect the galaxy formation process. It will be addressed the background material that supports the inferences about galaxy formation and evolution. Different properties of galaxies and dark matter halo connections will be taken into account. Structure formation and interactions between these objects also will be discussed.

1.4.1 *Cosmological Scenario*

Once the galaxies formation theory is built up within the CDM paradigm it is useful to learn how to measure distances, angular diameters among others in an Universe like this. The measurement of the Universe is important in the sense that if we want to reproduce it by computer techniques, one should know in a reliable way all the physical parameters involved that in most cases depend on distance. Knowing distances, angular diameters, luminosity distance and how they are affected by the expansion of the Universe is vital to understand how everything is performed.

1.4.1.1 *Parameters, Redshift, Comoving distance, Angular diameter and Luminosity distance*

The well known Hubble law that indicates a correlation between the distance to a galaxy and its recessional velocity (a relative velocity away from the Earth). Today, this law is expressed in terms of the distance of a galaxy and a constant which is identified as the Hubble constant referred to the present epoch ("0") because it could change with time. Thus,

$$v = H_0 d \tag{1.2}$$

where $H_0 = 100h \text{ km s}^{-1} \text{ Mpc}^{-1}$. The dimensionless parameter h helps us to encapsulate our ignorance about the real number have, but recent observations points out that it can be between $0.6 < h < 0.9$ [18]. Moreover, the Hubble time t_H and Hubble distance D_H are given in terms of the Hubble constante by,

$$t_H \equiv \frac{1}{H_0} = 3.09 \times 10^{17} h^{-1} \text{ s} \quad (1.3)$$

$$D_H \equiv \frac{c}{H_0} = 3000 h^{-1} \text{ Mpc} \quad (1.4)$$

The mass density (ρ) and the cosmological constant Λ which are dynamical properties can be treated as kinematical quiantites contained into dimensionless density parameters evaluated at the presen epoch as,

$$\Omega_M \equiv \frac{8\pi G \rho_0}{3H_0^2} \quad (1.5)$$

$$\Omega_\Lambda \equiv \frac{\Lambda c^2}{3H_0^2} \quad (1.6)$$

A third density parameter that measures the curvature of space can be obtained in terms of the last two: $\Omega_M + \Omega_\Lambda + \Omega_k = 1$. Then, if the space is euclidean the curvature density parameter is $\Omega_k = 0$. In Table 11 some usual values of Ω_M and Ω_Λ can be checked.

On the other hand, the doppler effect is useful to given a fractional shift of the emitted light of an

Table 11: **Values of density parameters for specific models**

	Ω_M	Ω_Λ
Einstein-de-Sitter	1	0
low density	0.05	0
high lambda	0.2	0.8

Note: The table was taken from [18]

object due to the radial motion which is well known as the *Redshift* and is given in terms of the emitted frequency and wavelenght and the observed ones by,

$$z \equiv \frac{\nu_e}{\nu_o} - 1 = \frac{\lambda_o}{\lambda_e} - 1 \quad (1.7)$$

In special relativity the redshift can be related to the velocity by Equation 1.8, which is true in one particular coordinate system, but not any of the traditionally used coordinate systems [18].

$$1 + z = \sqrt{\frac{1 + v/c}{1 - v/c}} \quad (1.8)$$

There exists a difference between an object's measured redshift z_{obs} and its cosmological redshift z_{cos} due to its peculiar velocity v_{pec} . The cosmological one is referred as that part of the redshift due solely to the expansion of the Universe or the Hubble flow. These quantities are related by

$$v_{pec} = c \frac{(z_{obs} - z_{cos})}{(1 + z)} \quad (1.9)$$

where $v_{pec} \ll c$, so from here on $z = z_{cos}$ [18]. When v/c or distance is small, in the expanding Universe, the velocity is proportional to the distance and can be expressed in terms of the Hubble distance D_H by Equation 1.10 which is only true for small redshifts,

$$z \approx \frac{v}{c} = \frac{d}{D_H} \quad (1.10)$$

Finally, redshift can be related with the size of the Universe through the scale factor $a(t)$ evaluated at a time when the light is emitted and when the light is observed to, by,

$$1 + z = \frac{a(t_o)}{a(t_e)} \quad (1.11)$$

Another useful quantity to be defined is the "*Comoving Distance*" which is sometimes referred as a distance measured at the same time the object is being observed. If two objects are moving with the Hubble flow, the comoving distance is a distance which remains constant with time. Integrating those small comoving distances between nearby events from $z=0$ to the object it is possible to obtain the total comoving distance D_c . The total line of sight comoving distance is given by integrating the contributions by,

$$D_c = D_H \int_0^z \frac{dz'}{E(z')} \quad (1.12)$$

where $E(z) = \sqrt{\Omega_M(1+z)^3 + \Omega_k(1+z)^2 + \Omega_\Lambda}$. The line of sight comoving distance is a fundamental distance because it helps to define other distances. The comoving distance between two points close in redshift is the distance which one could measure if those two points were locked into the Hubble flow [18].

Another common quantity is the "*Angular Diameter Distance*". It is defined as the ratio of an object's physical transverse size D_M and to its angular size in radians. If the redshift at which the object is observed is small the transverse size can be approximated to the line of sight comoving distance. Thus,

$$D_A = \frac{D_C}{1 + z} \quad (1.13)$$

At high redshift the angular diameter distance is such that 1arcsec is on the order of 5kpc [18].

Finally, other commonly used distance is the "*luminosity distance*". It is defined in terms of the bolometric flux S and bolometric luminosity L which is related to the comoving transverse distance D_M and the angular diameter size D_A through $D_L = (1+z)D_M = (1+z)^2 D_A$.

$$D_L \equiv \frac{L}{4\pi S} \quad (1.14)$$

1.4.2 Background Material

A combination of experimental measures including CMB (cosmic microwave background), large scale structure, the type Ia supernovae magnitude-redshift relation and galaxy clusters, have constrained the parameters of the CDM cosmogony. Thus, the energy density of the Universe attached to these studies indicates that dark energy density is $\Omega_\Lambda = 0.728^{+0.015}_{-0.016}$, dark matter density $\Omega_c = 0.227 \pm 0.014$ and baryonic matter density $\Omega_b = 0.0456 \pm 0.0016$ with a Hubble parameter of $70.4^{+1.3}_{-1.4}$ km/s/Mpc. Given this picture, the Universe is 13.75 ± 0.11 Gyr old and galaxies probably began forming when first sufficiently deep dark matter potential wells formed to allow gas to cool and condense at redshift $z \sim 20 - 50$ [8].

As predicted by inflation, initial slight perturbations in dark matter density expanded to cosmological scales, seeding the formation of large scale structures. In the linear regime the early evolution of these perturbations are well understood, once the perturbations become non-linear evolution turn a bit complicated but simple arguments provide insights into a basic behavior. N-body simulations and empirical methods predict the formation of large scale structure that looks like a cosmic web where halos string along walls and filaments. Thus, the final result of a non-linear evolution is the formation of dark matter halos, which are near equilibrium structure supported against its own self-gravity by the random motions of its constituent particles. So, once the first generation of halos have formed, latter halos will be formed by mergers of earlier generations according to a hierarchical Universe where big structures are formed by accretion of small ones.

There are two important properties of dark matter halos for galaxy formation:

- Distribution of masses at any redshift.
- Distribution of formation histories (statistical properties of the halos from which they formed).

According to Press and Schechter (1974), if one considers a gaussian random density field for dark matter, the peaks in the early Universe could be associated to dark matter halos. Under this approximation the form for the distribution of dark matter halo masses such that the number of halos per unit volume in the mass range M to $M+\delta M$ is $\delta M(dn/dM)$, is:

$$\frac{dn}{dM}(M, t) = \left(\frac{2}{\pi}\right)^{1/2} \frac{\rho_0}{M^2} \frac{\delta_c(t)}{\sigma(M)} \left| \frac{d \ln \sigma}{d \ln M} \right| \exp \left[-\frac{\delta_c^2(t)}{2\sigma^2(M)} \right] \quad (1.15)$$

where, ρ_0 is the mean density of the Universe, $\sigma(M)$ is the fractional root variance in the density field smoothed using a top-hat that contains, on average, a mass M , and $\delta_c(t)$ is the critical overdensity for spherical top-hat collapse at time t .

The expression is remarkably accurate given its simplicity, but does not provide an accurate description of modern N-body measures of halo mass function. The most accurate fitting formulae available are those of Tinker *et al* (2008):

$$\frac{dn}{dM} = f(\sigma) \frac{\bar{\rho}}{M} \frac{d \ln \sigma^{-1}}{dM} f(\sigma) = A \left[\left(\frac{\sigma}{b} \right)^{-a} + 1 \right] \exp \left(-\frac{c}{\sigma^2} \right) \quad (1.16)$$

over here, A, a, b and c must be given by fitting to the results of N-body simulations and mass variance $\sigma^2(M)$ must be given from the power spectrum of density fluctuations:

$$\sigma^2(M) = \frac{1}{2\pi^2} \int_0^\infty P(k) T^2(k) \hat{W}_H^2(k) k^2 dk \quad (1.17)$$

$P(k)$ is the primordial power spectrum, $T(k)$ cold dark matter transfer function and $\hat{W}_H(k)$ fourier transform of the real-space top-hat window function.

In the same way, with similar arguments of Press and Schechter (1974) a statistical description of halo formation can be achieved taking into account merging event and masses involved. Progenitor masses M_1 at redshift z_1 form a halo of mass M_2 at redshift z_2 given by:

$$\frac{dN}{dM_1} = \left(\frac{2}{\pi} \right)^{1/2} \frac{d \ln \sigma}{d \ln M_1} M_2 \frac{\sigma_1^2}{M_1^2} \frac{\delta_{c1} - \delta_{c2}}{(\sigma_1^2 - \sigma_2^2)^{3/2}} \exp \left[-\frac{(\delta_{c1} - \delta_{c2})^2}{(\sigma_1^2 - \sigma_2^2)} \right] \quad (1.18)$$

where $\sigma_1 = \sigma(M_1)$, $\sigma_2 = \sigma(M_2)$, $\delta_{c1} = \delta_c(z_1)$ and $\delta_{c2} = \delta_c(z_2)$. This formula is useful to model the merger history of halos. A limitation using this approximation, is that merger rates are not symmetric, in the sense that switching M_1 and M_2 are two completely different scenarios.

Dark matter halos are characterized by their large overdensity Δ (corresponds, approximately, to the virialized region of a halo) with respect to the background density. Overdensity of a just collapsed halo is approximately 200, and depends on cosmological parameters as shown by spherical top-hat collapse models.

The virial radius can be defined in terms of the overdensity as:

$$r_v = \left(\frac{3M}{4\pi\rho_0\Delta} \right)^{1/3} \quad (1.19)$$

where r_v is the radius for the transition from ordered inflow of matter on large scales to virialized random motions on small scales. In fact, the virial theorem is obeyed within it.

The dark matter halos have a triaxial shape and in cold dark matter cosmologies the density

profiles have an approximately universal form, better described by the Einasto profile than the Navarro-Frenk-White profile (now on NFW). Einasto density profile is expressed as:

$$\rho(r) = \rho_{-2} \exp\left(-\frac{2}{\alpha} \left[\frac{r}{r_{-2}}^\alpha - 1\right]\right) \quad (1.20)$$

here r_{-2} is the characteristic radius where logarithmic slope of density profile equals -2 and α is a control parameter. This parameter correlates well with the height of the peak from which a halo formed.

The NFW profile has a simpler form:

$$\rho(r) = 4 \frac{\rho_s}{(r/r_s)[1 + r/r_s]^2} \quad (1.21)$$

r_s corresponds to a characteristic scale radius, ρ_s is the density at $r = r_s$. The concentration for the NFW profile can be defined as $C_{NFW} = r_v/r_s$. Concentrations are found to depend weakly on halo mass and on redshift and can be related to the formation history of a halo.

Once the background material about the galaxy formation theory is clear, the physical properties of galaxies and halos and the mechanisms that affect their evolution come out. New questions about how they evolve must be answered. In the next sections the physical behavior of dark matter halos will be addressed according to the baryonic matter evolution and their interactions.

1.4.3 Pre-galactic Evolution of Baryons: Mechanisms of cooling and heating

Clearly after introducing dark matter halos and baryonic matter the following step is to explain how the matter distributes in the Universe to form galaxies and what are the processes involved.

At first, baryons are distributed near uniformly but to form galaxies one needs gravity to pull them together. That gravity is mainly dominated by the distribution of dark matter. Baryonic matter is expected to concentrate towards the deep potential wells of dark matter halos where galaxies will be formed. Baryonic material will be, then, dragged along by the gravitationally dominant dark matter. The depth of the potential well and the pressure of baryons are really important because the amount of accreted material depends upon them. In some interval δt , after the Universe has been reionized, the mass of baryons (M_b) accreted by a dark matter halo depends on a timescale for gas to evaporate from the progenitor halo, denoted by (t_{evp}) and the time interval. This is given by:

$$M_b = M'_b + M_{acc} \quad M'_b = \sum \exp\left(-\frac{\delta t}{t_{evp}}\right) M_b \quad (1.22)$$

where the timescale of evaporation depends on a temperature T_{evp} below which the gas will be heated and evaporate from the halo. For a given sound speed c_s , T_{evp} is modelled as:

$$t_{evp} = \begin{cases} r_v/c_s & \text{if } T_v < T_{evp} \\ \infty & \text{if } T_v > T_{evp} \end{cases} \quad (1.23)$$

$$M_{acc} = \begin{cases} \frac{\Omega_b}{\Omega_0} & \text{if } T_{vir} > T_{acc} \\ 0 & \text{if } T_{vir} < T_{acc} \end{cases} \quad (1.24)$$

An accretion shock is expected whenever the gas accretes supersonically, as it will do, if the halo virial temperature exceeds the temperature of the accreting gas. When cooling times are long compared to dynamical times, shock occurs at a radius comparable to the virial radius. Masses in the range $10^{10} - 10^{12} M_\odot$ cool so efficiently that they always collapse at the free-fall rate, and probably quickly fragments into stars.

Gas which experience a strong virial shock will have its kinetic infall energy thermalized and therefore be heated to a temperature of the order of the virial temperature 1.25. Also, the gas will produce a hydrostatically supported atmosphere obeying the hydrostatic equilibrium equation 1.26.

$$T_v = \frac{2}{3} \frac{GM_v}{r_v} \frac{\mu m_H}{\kappa_B} \quad (1.25)$$

$$\frac{dP}{dr} = - \frac{GM(r)}{r^2} \rho(r) \quad (1.26)$$

where P is the pressure, $\rho(r)$ the gas density and $M(r)$ the total mass (dark matter and baryonic matter).

On small scales the distribution must be modified due to other contributions to support halo against gravity, such as turbulence, cosmic ray pressure and magnetic pressure. The gas is able to cool radiatively and so will eventually lose energy and consequently pressure support. At this point, it must fall towards the center of the gravitational potential of the dark matter halo, increasing its density. Gas which does not experience a shock close to the virial radius can fall almost basically towards the halo center. It must lose its infall energy at some point, shocking closer to the halo center, near the forming galaxy, where it would be eventually heated and must cool down again later.

Gas must to cool down to form a galaxy. Thus, cooling mechanisms are in charge of this task. Mechanisms as atomic, compton and molecular hydrogen cooling will be briefly described in next sections.

1.4.3.1 Atomic

The primary cooling mechanisms at low redshifts are a combination of several atomic processes including recombination radiation, collisional excitation and subsequent decay and Bremsstrahlung for metal rich gas, or gas hot enough ($T \gtrsim 10^4 \text{K}$).

A usual cooling rate for atomic processes depends upon the squared number density of Hydrogen (neutral and ionized) and a cooling function $\Lambda(T, \mathbf{Z})$ which depends not just on overall metallicity, but on detailed chemical composition of the gas. This cooling rate is then expressed as:

$$\mathcal{L} = n_H^2 \Lambda(T, \mathbf{Z}) \quad (1.27)$$

1.4.3.2 Compton Cooling

Unlike low redshifts, at high redshifts the density of cosmic microwave background becomes sufficiently high that the frequent Compton scattering of these photons from electrons in the ionized plasma inside the dark matter halos result in a cooling of the plasma. Compton cooling timescale can be estimated through:

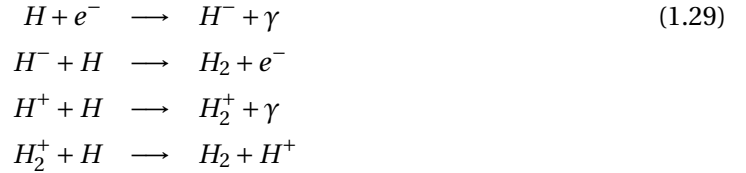
$$\tau_{Compton} = \frac{3m_e c(1 + 1/\chi_e)}{8\sigma_T a T_{CMB}^4 (1 - T_{CMB}/T_e)} \quad (1.28)$$

where χ_e corresponds to the ratio between electron number density n_e and number density of all atoms and ions n_t , T_e is the electron temperature of the gas and T_{CMB} is the cosmic microwave background temperature.

CMB photon density is the same everywhere, so independent of local gas density, Compton cooling rates scales linearly with density in contrast with atomic cooling which scales as the square. If the gas is considered isothermal and has the same electron function everywhere the Compton scattering can happen at all radii.

1.4.3.3 Molecular Hydrogen Cooling

On the other hand, at high redshifts gas in dark matter halos is too cold to cool any further. In halos with virial temperature below 10^4K , even shock heated gas will be mostly neutral and therefore unable to cool via the usual atomic processes. The dominant coolant in such case becomes the small fraction of hydrogen in form of molecular hydrogen. This process, is crucial for star formation of first stars and galaxies and of course the source that caused the reionization of the Universe. The molecular hydrogen forms via the gas-phase reactions:



The cooling time scale of this process is found by first estimating H_2 abundance f_{H_2} , a cooling function Λ_{H_2} of molecular hydrogen, temperature T_V and hydrogen number density n_{H_I} in cm^{-3} [Equation 1.30](#).

$$\tau_{H_2} = 6.56419 \times 10^{-33} T_V f_{H_2}^{-1} n_{H_2}^{-1} \Lambda_{H_2}^{-1} \quad (1.30)$$

Although gas needs to cool down in order to collapse and form a galaxy, several physical processes heat the gas instead of cooling it. Thus, heating processes are really important to know how they affect the formign galaxies inside the dark matter halos. Processes as photoheating, feedback heating, thermal conduction and preheating will be addressed.

1.4.3.4 *Photoheating*

After the recombination, the cosmological background light consists of blackbody radiation of the CMB. Once stars begin to form they emit photons on a wide range of energies, some greater than the ionization energy of some coolants such as hydrogen, helium and heavier metals. Then, those photons can photoionize atoms and ions inside the dark matter halos changing the ionization balance heating the gas and altering the way gas cools to form a galaxy. Heating becomes important for temperatures $T < 3 \times 10^4 \text{ K}$.

1.4.3.5 *Heating from Feedback*

A longstanding issue that arise about gas cooling is known as the overcooling problem. Gas can cool at sufficiently large rate that, by the present day, galaxies much more massive than any observed will have formed. A way to avoid this problem is through heating the cooling gas.

In the massive halos where overcooling is a problem, energy input from supernovae is insufficient to offset cooling, so a new idea of heating caused by AGN (active galactic nuclei) may be responsible for solving the overcooling problem. The mechanism by which energy output from AGN is coupled to the surrounding atmosphere remains unclear.

1.4.3.6 *Preheating*

Prior to the collapse into the dark matter halo, heating can occurs and later evolution of baryons can be affected. Before virial collapse and any associated shock heating, the gas evolves approximately adiabatically maintaining a constant entropy. A preheating will be remembered by the gas because the entropy is a conserved quantity. It is worth to notice that entropy distribution of preheated gas is the same as the non-preheated but with a floor of minimum of entropy. Then, the so called entropy floors lead to a density core in the halo center increasing the cooling times in the halo core and helping to prevent the formation of super massive galaxies via the overcooling problem.

1.4.3.7 *Thermal Conduction*

The shock heated gas in dark matter halos forms a ionized plasma, so it is expected to have a thermal conductivity. For the inner regions of the atmosphere, conductivity can act as a heat source. As they cool, heat is conducted inwards from the outer and hotter regions of the atmosphere. This, could be a mechanism to solve the overcooling problem, but it has been demonstrated that it is not sufficient to offset cooling rates.

In summary, the simplest picture is a gas which cools below the virial temperature loses pressure support and flows smoothly towards the minimum of gravitational potential well, setting there to form a galaxy. Cooling then fragments into two phases: Cold ($T \approx 10^4 \text{ K}$) dense clouds in pressure equilibrium with a hot (approximately virial temperature), diffuse component which can persist for cosmological periods of time due to a long cooling time. Those clouds masses are given by thermal conduction limit, Kelvin-Helmholtz instabilities and conductive evaporation, which destroy clouds. The rate of gas supply to a forming galaxy depends on the rate at which dense clouds infall due to hydrodynamical drag happen and cloud-cloud collisions.

Other important processes related with the dynamics of every dark matter halo are of such importance for the forming galaxies. Mergers, tidal forces and harassment can affect the evolution

of baryonic matter and the cloud infall process. Next sections will address interactions between dark matter halos and their main implications.

1.4.4 Interactions: Mergers, harassment and hydrodynamical interactions

Many galaxies seem to be evolving in isolation, while many others seem to interact with the environment. The hierarchical nature of structure formation in a cold dark matter Universe has a first consequence and is it that the dark matter halos are built through the merging of earlier generations of less massive halos.

As shown by current highest resolution simulations, multiple levels of subclustering can coexist (subhalos within subhalos within subhalos). Thereby, halos can persist as subhalos within large halos into which they merge. Each subhalo acts as a site of galaxy formation and so may contain a galaxy which could host a satellite in the host potential. Subhalos are gravitationally bound to their host halo and, as such, will orbit within it. A subhalo's orbit can take him into regions where interactions affect the properties of any galaxy that it may contain. Thus, properties of galaxies can be modified by the internal dynamics of subhalos which is of main importance to know the final state of a formed galaxy.

Merging, tidal destruction, harassment and ram pressure will be addressed to relate changes in the properties of galaxies within dark matter halos and subhalos.

1.4.4.1 Mergers

Orbiting subhalos are gravitationally bound to their host halos, so to induce gravitationally bound interactions between subhalos and their galaxies requires a dissipative process to reduce their orbital energies [8]. This role is fulfilled by dynamical friction which tends to drag the orbital energy of subhalos making them to spiral to the center of their host halo, where they merge with the central galaxy which finds itself there.

Merging timescales for subhalos in isothermal dark matter halos depend on the orbital parameters of the subhalo, angular momentum of the satellite and angular momentum of a circular orbit of the same energy, E , as the actual orbit and the radius of the circular orbit. All this summarized in [Equation 1.31](#)

$$T_{df} = \frac{f(\epsilon)\tau_{dyn}}{2B(1)\ln\Lambda} \left(\frac{r_c}{R_v}\right)^2 \left(\frac{M_v}{m_v}\right) \quad (1.31)$$

where $f(\epsilon)$ encapsulates the depending on the orbital parameters in $\epsilon = J/J_c(E)$ where J is the angular momentum of the satellite and $J_c(E)$ is the angular momentum of a circular orbit with energy E at the actual orbit and radius r_c . The dynamical time $\tau_{dyn} = R_v/V_v$ depends on both virial radius and velocity. The virial mass of the satellite is given by m_v and the Coulomb logarithm $\ln\Lambda = \ln(r_v V_v^2/Gm_v)$ in terms of virial parameters.

This approximation has a lot of problems because dark matter halos are not isothermal. Recent attempts have been made to find an empirical formulae to describe the merging timescale which begins with similar expressions as [Equation 1.31](#) but add empirical dependencies on subhalo mass and orbital parameters which are constrained to match results of N-body numerical simulations as those presented by Boylan-Kolchin et al. (2008) and Jian et al. (2008) [8].

1.4.4.2 *Tidal Destruction*

The galaxy and an orbiting subhalo will experience tidal forces which may strip away the outer regions or, in extreme cases, entirely disrupt the galaxy resulting in a stellar stream. The effective tidal field felt by the satellite depends on the mass enclosed within a radius r in the host halo and the instantaneous angular velocity ω of the satellite. Beyond the tidal radius material becomes unbound from the satellite, forming a stream of dark matter and probably stars which continue to orbit in the host potential.

Tidal interactions could take away mass from the system. If tidal mass loss depends on density profile of the satellite and on the velocity distribution of the constituent particles, those particles on an orbiting satellite that are on prograde orbits are more easily stripped than those on radial orbits, which are in turn more easily stripped than those on retrograde orbits [8].

1.4.4.3 *Harassment*

A less extreme form of tidal interaction arises when tidal forces are not strong enough to actually strip material from a galaxy. The tidal forces can nevertheless transfer energy from the orbit to internal motion of stars in the galaxy, heating the galaxy. The result of that heating is to expand the galaxy and to destroy cold, ordered structures such as disks.

The harassment process works via tidal shocking in which the stars in a galaxy experience a rapidly changing tidal field along its orbit and gain energy in the form of random motions, leading to the expansion of the system and making it dynamically hotter.

1.4.4.4 *Hydrodynamical Interactions (Ram Pressure)*

It has been said that collisionless dark matter can only be affected by gravity, but baryonic content of galaxies (and their surrounding atmospheres of gas) can be strongly affected by both gravity and hydrodynamical forces.

Ram pressure is one of those hydrodynamical forces that can affect the evolution of galaxies within dark matter halos. The orbital motion of a subhalo through the hot atmosphere of a host halo leads to a large ram pressure. This pressure, may be expected to efficiently remove the hot atmosphere of satellite galaxies and the ISM (interstellar medium) of the galaxy, a process with several aliases including strangulation and starvation.

It plays an important role in mediating the transition of cluster galaxies from the blue cloud of star-forming galaxies to the red sequence of passively evolving galaxies.

1.4.5 *Galactic Structure*

Preceding sections described how gas achieves high density to allow a galaxy to form, specifically concentrated in the formation of disk galaxies. So, once all of those processes as merging, interactions, cooling and heating of gas have occurred the next question to address is about the structure of the galaxy. What is the structure that will have the galaxy which forms within the dark matter halo. It all depends on the amount of angular momentum present in the infalling gas. Thus, structure is given by the baryonic and dark matter component, and the specific angular momentum distribution of the fraction of infalling gas that will cool and settle down to form the galaxy [14].

In this section we will address the structure of disk and spheroidal components, as well as issues related to size distribution on stability of such systems.

1.4.5.1 Disk Structure

All galactic disks owe their origins to the same fundamental process as other astrophysical disks: conservation of angular momentum in a system collapsing under gravity, eventually leading to arrest of the collapse by rotational support. Tidal torques from surrounding large structure provide the angular momentum of the gas which will eventually form the galaxy. This is the same process whereby dark matter halos obtain their angular momentum. The magnitude of angular momentum of baryonic matter of a halo is a scaled version of that of the dark matter. Thus, the distribution of differential specific angular momentum j [8] is given by:

$$\frac{1}{M} \frac{dM}{dj} = \frac{1}{j_d^\alpha \Gamma(\alpha)} j^{\alpha-1} e^{-j/j_d} \quad (1.32)$$

where M is the total mass of gas, $j_d = j_{tot}/\alpha$ and j_{tot} is the mean specific angular momentum of the gas. Earlier generations of hydrodinamical simulations found that disk galaxies lost significant fractions of their angular momentum, and as a result, they were too small. Recent simulations show approximate angular momentum conservation and this leads to disks with sizes as the ones observed. Certainly, gas cannot lose significant fractions of its angular momentum if it is to form a disk comaprable size to observed galactic disks.

During the early phase of protogalactic collapse gas and dark matter are well mixed-up so they get the same specific angular momentum distribution. If the angular momentum is conserved during gas infall, the disk size is going to be directly related to the specific angular momentum λ' of the surrounding dark matter halo, which is given by:

$$\lambda' = \frac{J}{\sqrt{2} M_{vir} V_{vir} R_{vir}} \quad (1.33)$$

with R_{vir} and $V_{vir}^2 = GM_{vir}/R_{vir}$ the virial radius and virial velocity of the halo respectively, and M_{vir} its the virial mass [14].

The angular momentum of the mass in the disk tracks that of the dark matter halo as a whole, growing as expected during the linear regime and remainning nearly constant after halo collapse. If there is a weak energy feedback heating the gas, the final result is a catastrophic collapse of the gas leading to a large spheroid. Its angular momentum also grows during the linear regime but then declines rapidly due to angular momentum transfer from dense, progenitor blobs to the surrounding, diffuse dark matter [8]. Feedback processes are so important here because during the formation of protogalaxies can raise up the angular momentum and prevent angular momentum loss heating the gas [14], via forces associated with HII regions and SNe blast waves.

Now, the size of the forming galaxy will be given by angular momentum. Once the angular momentum of baryonic matter which cooled to form a galaxy is known, the structure of a rotationally supported disk is governed by the equation:

$$\frac{j^2(M)}{R^3(M)} = \frac{\partial}{\partial R} \Phi(R) \quad (1.34)$$

where $j(M)$ is the specific angular momentum enclosing mass M and $\Phi(R)$ is the potential for a disk. This equation describes the size and structure of a disk galaxy which is supported by rotation. The potential is a sum of self-gravity of the disk and that of any external potential. For a thin disk with surface density $\Sigma(R)$ the potential is generally given by:

$$\Phi(R, 0) = -4G \int_0^R \frac{da}{\sqrt{R^2 - a^2}} \int_a^\infty dR' \frac{R' \Sigma(R')}{\sqrt{R'^2 - a^2}} \quad (1.35)$$

An exponential surface density profile as [Equation 1.36](#) simplifies the potential [Equation 1.35](#) to [Equation 1.37](#):

$$\Sigma(R) = \Sigma_0 \exp\left(-\frac{R}{R_d}\right) \quad (1.36)$$

$$\Phi(R, 0) = \pi G \Sigma_0 R [I_0(y) K_1(y) - I_1(y) K_0(y)] \quad (1.37)$$

Adopting a flat rotation curve, the disk scale length R_d can be obtained in terms of the specific angular momentum distribution as:

$$R_d \approx 8 \left(\frac{\lambda'}{0.035} \right) \left(\frac{H_0}{H} \right) \left(\frac{v_{max}}{200 \text{ km s}^{-1}} \right) \text{ kpc} \quad (1.38)$$

where v_{max} is the maximum rotational velocity in the disk and H is the Hubble parameter [\[14\]](#).

A complication arises in the sense that the external potential in which the disk forms is likely to change in response to the formation of the disk. So, the gravitational potential changes while galaxy forms.

Galaxy disks show a vertical extent. There are two possible origins to the origins of the vertical extent of galaxy, external and internal. External origins are related with accretion. Galactic disk can accrete pre-existing smaller stellar systems whose stars form a thickened disk structure in the same plane as the pre-existing disk of the galaxy. Dynamical friction will drag satellites towards the plane of the disk where forces tear it and leave its stars orbiting in that plane. On the other hand, the thick disk stars can be formed by accreted gaseous systems during an early, chaotic period of merging.

Internal origins, turn to be related with dynamical heating. A significant contribution to the thickening of galaxy disks, arise from the interactions with orbiting dark matter substructures which dominate the heating depending on the merger history of each galaxy's dark matter halo and the orbital properties of those massive substructures. Moreover, stars can be scattered by molecular clouds transforming some of their orbital energy in perpendicular motions thickening the disk. Or self spiral arms waves that can act as scatterers of stars increasing the velocity dispersion in the plane of the galaxy.

Finally, once the disks formed, itself stability is crucial to maintain over large timescales a given structure. Toomre (1964) derived an expression for the local stability of thin disks to axisymmetric modes in the tight-winding approximation:

$$Q = \frac{\kappa \sigma_{gas}}{\pi G \Sigma_{gas}} \quad (1.39)$$

where κ is the epicyclic frequency, σ_{gas} is the velocity dispersion of the gas and Σ_{gas} is the surface density of the gas. Then, Q gives the local stability so if $Q < 1$, disks will be unstable to axisymmetric modes. For a disk composed by gas and stars the stability criterion is given by:

$$Q = \frac{\kappa \sigma_{gas}}{\pi G \Sigma_{gas} g(\alpha, \beta)} \quad (1.40)$$

here $g(\alpha, \beta)$ is a function given by Efstathiou (2000) where α is the ratio of stellar to gas velocity dispersions and β is the ratio of stellar to gas surface density. The stability of a two-component disk can be approximated by: $Q = (Q_*^{-1} + Q_{gas}^{-1})^{-1}$. More recent studies have proposed improved stability criteria taking into account the kinetic energy T , the potential energy of the system W , the Jeans frequency Ω_j in the radial direction and the mean angular velocity Ω as found by Christodoulou et al. (1995b),

$$\alpha = \frac{T/|W|}{\Omega/\Omega_j} \quad (1.41)$$

Finally, global instabilities lead to the formation of a very strong bar which disrupts the disk leaving a boxy bulge or a disky bulge. Then, perturbations in the disk affect the structure. Resonant scattering from spiral arms can make a significant fraction of stars undergo large migrations in radius. This can lead to the formation of an outer stellar disk made up of stars scattered from the inner regions of the galaxy. This process smooths out ages and metallicity gradients than otherwise will result in a tendency to be older from inside out in the disk and less metal rich in the center.

1.4.5.2 Spheroidal Structure

The object formed within the dark matter halo does not need to have a disk structure. Spheroids can be formed via two distinct ways. The first, through violent mergers which destroy pre-existing stellar systems and a second, secular evolution of galactic disks as a consequence of the dynamics of self-gravitating disks. Bulges have been divided into two broad classes. The first called "classical" bulges which are elliptical in terms of its light distribution and kinematics but happen to live inside a disk and "pseudo-bulges" those which do not look ellipticals. There is strong evidence that the "pseudo-bulges" are formed through secular evolution of galactic disks while the "classical" form through major mergers.

Mergers are often separated into major (mergers between galaxies of comparable mass) and minor (mergers in which one galaxy is significantly less massive than the other). When the sizes

of the galaxies are comparable we may expect significant changes in the structure of the merger remnant. Those mergers are known as major mergers and they are thought to be responsible for the formation of spheroidal galaxies (ellipticals) which could have been disk galaxies, spheroidals or something intermediate before the merging. In violently relaxed systems an effect of hysteresis can arise because the final state of the system depends on how it goes from the initial state to a final state. In the merging system, mergers are expected to trigger a very large enhancement in the star formation rate. The strength of such star bursts depends on the properties of the merging galaxies. All major mergers do not end up forming a spheroid, it has become clear that under certain conditions major mergers of rich gas systems can lead to the reformation of a disk once the merger is over.

As it was shown before, major mergers are not the only way to build up a spheroid. The internal secular processes within galaxies can disrupt the cold and fragile disks. Bars, which is a disk phenomenon, can redistribute the angular momentum and the mass leading to a dense central mass concentration that lasts as a memory of bulges formed through mergers. These kind of bulges formed through secular processes are referred to as "pseudo-bulges". The secular processes likely operate in all galaxies because they are the result of generic dynamical considerations, involving the interaction of stars (or gas elements) with collective phenomena as bars or spiral arms. When the bar begins to form, it transfers angular momentum to the outskirts and increases in amplitude. The gas as a response accelerates if it enters and decelerates as it leaves, the bar potential. This leads to shocks forming in the gas and these shocks lead to a dissipation of orbital energy and consequently inflow of the gas. The increase in the concentration of gas in the inner regions leads to build up a "pseudo-bulge". The increase of central mass prevents the bar instability from working so bar eventually destroys itself this way.

The sizes of the spheroidal galaxies formed through major mergers can be derived knowing the properties of the progenitors and their orbit and some knowledge to the extent to which mass and energy is conserved. Energy is at least approximately conserved if the galaxies are dissipationless, that is purely stellar systems (dry merger). In gas rich (wet merger) the gaseous component is likely to radiate significant amounts of energy prior to forming stars [8].

1.4.6 *Properties of the dark matter halo and the connection with the host galaxy*

Dark matter halos are strongly connected with the properties of the host galaxies as seen in the last sections. The angular momentum distribution, mass, interactions among others are responsible of the appearance or the shape and size a galaxy will have. Within the cold dark matter paradigm, galaxies are expected to form through collapses of dark matter to form small halos which can accrete matter and merge to form larger halos. Later on, gas can cool down and collapse to the center of the dark matter halos where a galaxy will be build up. Thereby, galaxy properties should be strongly related to the dark matter halos in which they are embedded.

In general, many structural properties of dark matter halos depend on the halo mass. For example, massive halos are less concentrated and more prolate on average. Also, parameters as spin can present correlations at high redshifts but no dependence on mass at low redshifts [25].

Next sections will take care about different parameter of dark matter halo and its direct consequences on the galaxy properties. Correlations among each mass, spin, shape with mass will be addressed.

1.4.6.1 Concentration Parameter

The concentration of the halo is related to the density profile of the galaxy because it tells us which galaxy is more concentrated than others. As shown before, the most widely used profile to fit the dark matter halo distribution is the NFW (Navarro-Frenk-White profile):

$$\frac{\rho(r)}{\rho_c} = \frac{\delta_c}{(r/r_s)(1+r/r_s)^2} \quad (1.42)$$

Thus, the concentration of the halo can be defined using the virial radius of a halo R_{vir} and the characteristic scale radius r_s as $C \equiv R_{vir}/r_s$. The virial radius is often set as a radius where mean density of a sphere of radius R_{200} is 200 times the critical density $\langle \rho \rangle = 200\rho_{crit}$ where the Einstein-de Sitter critical density is given by $\rho_{crit} = 3H^2/8\pi G$. This radius separates the virialized and infall regions [2]. On the other hand, the scale length r_s is a characteristic radius and a free parameter of the NFW density profile.

The concentration depends strongly on the virial mass M_{vir} . As shown by [25], the relation $c_{vir} - M_{vir}$ in a log space follows an almost linear relation. At a redshift $z = 2$ the linearity seems to break in agreement with other authors. Their fitting power law to this behavior is given by:

$$\log(c) = a(z)\log(M_{vir}/[h^{-1}M_\odot]) + b(z) \quad (1.43)$$

where $a(z)$ and $b(z)$ are functions of the redshift. Typically, the median halo concentration declines with increasing mass and redshift. Klypin et al. (2010) found a novel feature at high redshifts where the concentration flattens and then increases slightly for high masses [26].

The virial radius increases for all mass scales with decreasing redshift. R_{vir} is given by:

$$R_{vir}(z) = \left[\frac{3M_{vir}(z)}{4\pi\Delta_{vir}(z)\rho_c(z)} \right]^{1/3} \quad (1.44)$$

virial radius, then, grows at low redshift due to the growth of the halo mass $M(z) \sim \exp(-az)$. But at low redshift the halo mass growth rate becomes weaker than the factor $[\Delta_{vir}(z)\rho_c(z)]^{-1/3}$ decreasing the virial radius. this behavior shows a strong dependence of the halo mass. The growth rate of the concentration depends on the halo mass, where low-mass halos experience a faster concentration evolution. For massive halos in recent time concentration starts to grow at faster rate due to the collapse of the inner part.

1.4.6.2 Spin Parameter

The spin parameter is defined in terms of the virial mass M_{vir} within the virial radius R_{vir} and the total angular momentum of the mass distribution J_{vir} and it is given by:

$$\lambda' = \frac{J_{vir}}{\sqrt{2}M_{vir}V_{vir}R_{vir}} \quad (1.45)$$

This quantity is a measure of the amount of rotation of a dark matter halo and it is dimensionless. For low redshift the spin parameter is almost mass independent. For high redshift emerges a mass dependence that develops with high-mass halos. Thus, spin parameter and mass are weakly correlated. On average, more massive halos have lower values of the spin parameter.

1.4.6.3 *Shape Parameter: Relaxed-Unrelaxed halos*

The shape of halos is triaxial. The major, intermediate and minor axes of the halo distribution are $a_1 \geq a_2 \geq a_3$ so one can define the axial ratios $s = a_3/a_1$ and $p = a_3/a_2$. If the halo obey a relation between the axial ratios as $s \sim p < 1$ it is known as oblate, but if fits $s < p$ with $p \sim 1$ is known as prolate. Of course a condition for a halo to be spheric is $s \sim p \sim 1$. Triaxiality will be any other different form which do not fulfill the last ones.

On average halos are preferentially triaxial. Most massive tend to be most ellipsoidal, while lower mass tend to be closely spherical and this trend is independent of the redshift [25]. Thus, massive halos are the less concentrated and the more extended ones (ellipsoidal), and more affected by tidal torques.

OBSERVATIONAL DATA

2.1 INTRODUCTION

In this section we present all the repositories used to make the characterization of galaxies used in this work as the SDSS [7], NYU-VAGC [11] and Huertas [19] sample. All the connections between these different repositories and the data extracted are explained in a sense to address our problem. Indeed, along this section the selection criteria are explained and the extracted sub-samples under our criteria are justified to obtain the final data. Constraints in the probabilities obtained by Huertas [19], behaviors in the fundamental plane, well measured properties of galaxies (expected ranges), redshift constraints and so on was taken into account to get a final sample. Something which is really important in this chapter are the units used by the SDSS and the way we convert them into physical units to finally relate them with any other observational data to ensure a good sample before comparing it with a model to obtain information about the dark matter halo.

The main aim is to simplify the problem and obtain a robust sample of disk galaxies to compare them later on with a model for disk galaxies [22]. Although some interesting relations and behavior of the whole sample are explored throughout the chapter and some comments are done about it. Ideas and different points of view are discussed to clarify why some objects are rejected and why some makes-up the final sample.

2.2 RESEARCH DATA REPOSITORIES

Data repositories are really important when one wants to analyse the properties of celestial objects. In this case, properties of galaxies. They are useful in the sense that surveys are in charge of developing a well defined data base where the Astronomers or resercher can extract information. This is related with the mining of data. However, when other authors have enriched some samples it is useful to connect them all to have a wide range of properties of galxies and a detailed study. Data repositories are widely used by Astronomers to achieve their goals and in this case the Sloan Digital Sky Surver (SDSS) is the target because most of the cataloges employed here are extracted from it.

In the next sections a wide explanation about the repositories and the methods used to obtain the final samples of galaxies used to develope our work are thoroughly explained. First of all, the Sloan Digital Sky Survey (SDSS) which provides the main data sample in every case is addressed. Photometric and spectroscopic data can be found here, mainly in the DR7 which is used, both in the SDSS and the automated classification of galaxies. Later on, we describe the NYU Valued-Added Galaxy Catalog (VAGC) is described because most of the main properties of galaxies as colors, velocity dispersion and Sérsic's parameters are found in some of their repositories. So the VAGC, which indeed is built from the SDSS is vital for the analysis of general properties of the galaxies. Finally, the most important repository is explained and the different methods used to classify the galaxies achived by [19] in an automated way. Multiple connections between SDSS,

VAGC and Huertas catalog are important to enrich the first sample and to do a detailed analysis of galaxy properties and classification.

2.2.1 Sloan Digital Sky Survey (SDSS) Data

The Sloan Digital Sky Survey began a decade ago, with the goals of obtaining spectroscopy of a million galaxies and 100,000 quasars, and CCD imaging in five broad bands over $10,000 \text{ deg}^2$. It has been used to explore the structure and kinematics of our galaxy through the Sloan Extension for Galactic Understanding and Exploration (SEGUE), and an imaging survey that has discovered more than 500 spectroscopically confirmed Type Ia supernovae with amazing light curves.

A wide-field 2.5 m telescope is used, located at Apache Point Observatory, Sacramento Peak, New Mexico. It works with two instruments. The first is a wide-field imager with 24 2048×2048 CCDs, covering the sky in drift-scan mode with five filters (*riuzg*). The effective exposure time per filter is 54.1 s and 18.75 deg^2 are imaged per hour in each of the five filters [7]. Images are mostly taken with moonless photometric nights and under good seeing conditions. SDSS judges photometricity monitoring fluctuations in the night sky measured by a wide area infrared camera sensitive to $10 \mu\text{m}$ where the clouds are emissive. then, if the night is photometric it means that the fluctuations remains constant and small through the night. The 95% completeness limits of the images are $u, g, r, i, z = 22.0, 22.2, 22.2, 21.3, 20.5$ but the values may change because they depend on seeing and sky brightness. The photometric calibrations are done in two ways. The first comparing to standar photometric stars measured by another 0.5 m telescope and the other one by a process called ubercalibration which overlaps adjacent imaging runs to tie the photometry of all imaging observations together.

The second intrument is a 640-fiber-fed pair of multiobject double spectrographs covering from 3800\AA to 9200\AA at a resolution of $\lambda/\Delta\lambda \approx 2000$. A template in an aluminium spectroscopic plate is formed by 640 objects in each tile, where the targets are arranged. The holes in the plate are drilled with optical fibers that feed the spectrographs. Exposures are 15 minutes long, and three or more are taken for given plates to reach predefined requirements of signal-to-noise ratio $((S/N)^2 > 15)$ per 1.5\AA pixel for stellar objects of fiber magnitude $g = 20.2$, $r = 20.25$ and $i = 19.9$. For SEGUE faint plates exposures are deeper (eight of 15 minutes). The vast majority of the spectra of galaxies and quasars yield reliable redshifts. A separate pipeline is in charge of processing stellar targets to determine surface temperatures, metallicities and gravities.

Additional imaging products were run apart from CAS as Legacy, SEGUE, Stripe 82 among others. "Stripe 82" is a SDSS stripe along the celestial equator in the Southern Galactic Cap which has been imaged multiple times in the Fall months. the data were taken under optimal seeing, sky brightness and good photometric conditions. However, reruns were performed and added to the SDSS supernovae survey which was taken often under less optimal conditions as poor seeing, bright moonlight and nonphotometric conditions.

In brief, SDSS includes five-band imaging over 10^4 deg^2 with 2% rms errors or better in photometric calibration, and spectroscopy of 10^6 galaxies and 10^5 quasars. The main goals were met, and extesive stellar spectroscopy of close to a half a million stars, and repeat imaging over 250 deg^2 to search for supernovae were carried out.

2.2.2 The NYU Value-Added Galaxy Catalog (VAGC)

The NYU-VAGC is a value-added catalog built from SDSS containing objects mostly below $z \approx 0.3$ based (initially) on the SDSS DR2. Actually, DR7 contains at least 930.000 galaxies, 120.000 QSO's, and 460.000 stars and approximately 1.6 million spectra in total. It includes contiguous imaging and spectroscopy over 7500 deg² of the Northern Galactic Cap (Legacy Survey) and imaging and spectroscopy of stellar sources over an additional 3500 deg² of lower Galactic latitudes to study the structure of the Milky Way. Additionally, it contains calibrations, geometric descriptions and a small size, specifically designed for studying galaxy properties and large-scale structure statistics using the SDSS spectroscopic catalog. Generally catalogs are built up of terabytes of data too unwieldy to simply download onto a small workstation and investigate directly. Then, they created a galaxy redshift catalog designed to aid in the study of the local Universe where the SDSS form the basis for the work of studying luminosity function, power spectrum, correlation function, and a number of other galaxy properties and galaxy cluster statistics.

Some catalogs do not care about the geometry on the sky. On the NYU-VAGC, the geometry on the sky was stored as a set of disjoint convex spherical polygons because it brings advantages as easy determination if whether a point is inside or outside and simple methods to transform them into spherical harmonic components [11]. Moreover, the catalog is a mix of the SDSS, (FIRST) Faint Images on the Radio Sky at Twenty cm, (2MASS), Two-Degree Field Galaxy Redshift Survey (2dFGRS), the IRAS, the Point Source Catalog Redshift Survey (PSCz), and the Third Reference Catalogue of Bright Galaxies (RC3).

First of all, the SDSS uses u, g, r, i, z CCD imaging of 10⁴ deg² of northern galactic sky, and 10⁶ targets for spectroscopy from the imaging. Those bands used by the SDSS belongs to the modified Petrosian system. It is useful because it measures a constant fraction of the total light, independent of the position and the distance of the object [12]. In the Figure 9 it is shown the estimated response of the five bands in the SDSS as a function of the wavelength. SDSS filters are located

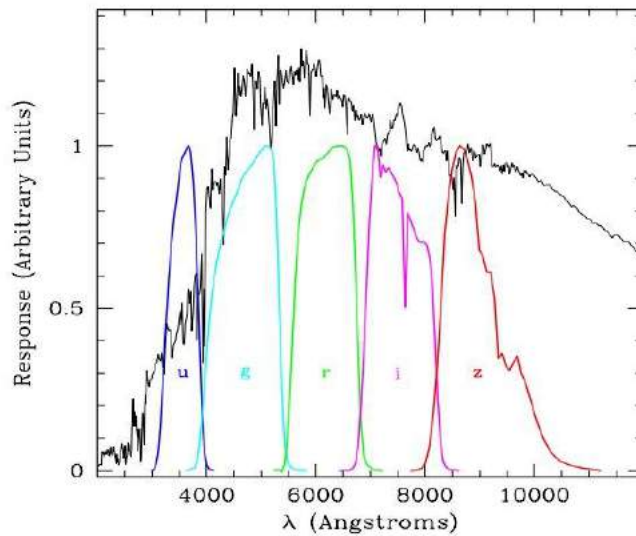


Figure 9: SDSS response to all five Petrosian bands u, g, r, i, z . It accounts for the mirrors, the filters, the atmosphere and the CCDs [10].

in a specific wavelength as follows: Ultraviolet(u) 3543Å, Green(g) 4770Å, Red(r) 6231Å, Near infrared(i) 7625Å and Infrared(z) 9134Å [4].

On the other hand, an automated software is in charge of performing all the data processing: astrometry, source identification deblending, and photometry calibration, photometric determination, spectroscopic target selection, spectroscopic fiber placement and spectroscopic data reduction [11].

It is important to notice that the SDSS's quantities are expressed in some peculiar units, thus:

- All fluxes f are given in "nanomaggies", a flux relative to that of the AB standard source with $f_v = 3631$ Jy. Then, an astronomical magnitude is related with the flux via $m = 22.5 - 2.5 \log_{10} f$.
- The zero point of the system are the same of the Archive Services.
- Uncertainties are expressed in terms of the inverse variance or in terms of the standard variation.

Now let's focus on some interesting features of the other catalogs composing the NYU-VAGC. The FIRST mapped 10,000 deg² of the northern sky, it overlaps the SDSS with a detection limit of 1mJy and a resolution of 5". It is better described with detail in the Princeton photometric reduction. The 2MASS is an all-sky map in the J, H, and K_s bands. Two catalogs were developed from this map as the Point Source Catalog (PSC K_s ~ 15, Vega relative) and the Extended Source Catalog (XSC a galaxy catalog K_s ~ 13.5). The 2dFGRS is a galaxy redshift survey which uses the 2dF multiobject spectrograph, targeted off of the Automated Plate Measuring survey. The IRAS-PSCz is redshift catalog point sources in the IRAS survey. Finally, RC3 catalog of nearby galaxies developed by de Vaucouleurs et al. (1991).

In the NYU-VAGC extra quantities were measured to perform the reduction of the data and to add new characteristics to the sample. Some galaxies are missing in the spectroscopic sample as a result of collided fiber constraints (two fiber cannot be placed more closely than 55") then collisions correlations were made. To make such corrections objects need to meet next conditions:

- Group galaxies with a friends-of-friends procedure were analyzed with a 55" linking length.
- If a galaxy does not have a redshift in the SDSS, a search for a galaxy or galaxies with redshift in its group is performed.
- If so, to the galaxy without redshift, it is assigned that of the galaxy of the group that is closest.

Another correction to the objects is done through the K-correction. All galaxies are treated as if they are normal galaxies, thus, the k-corrections are not going to be appropriated for QSO's. Then, an estimate of the u, g, r, i, z, J, H, K_s k-corrections and absolute magnitudes of each object are calculated using a $\Omega_0 = 0.3$, $\Omega_\Lambda = 0.7$ cosmology with $H_0 = 100h \text{ km s}^{-1} \text{ Mpc}^{-1}$ for $h = 1$. The J, H, K_s fluxes all come from 2MASS, XSC extrapolated magnitudes.

One of the most important quantities for this work it is related with the Sérsic profile. The NYU-VAGC catalog uses a Sérsic fit to the azimuthally averaged radial profiles of each object. Thus, for each galaxy it was fitted an axisymmetric Sérsic model of the form:

$$I(r) = A \exp \left[-(r/r_0)^{1/n} \right] \quad (2.1)$$

This is the same profile shown in [Chapter 1](#). However, Sérsic model is not a perfect model for galaxy profiles, for real data the fits apply unrealistically high changes to the sky level to attain slight decreases in the χ^2 . The resulting sizes and fluxes of the largest and brightest galaxies are obviously wrong.

At very low redshifts, many of the photometrically defined "galaxies" are not galaxies at all but instead are double stars. Generally, double stars are resolved, bright ($m_r < 16$), and small angular diameter $\Theta_{50} < 2''$ [11]. Treating low-redshift galaxies ($0.0033 < z < 0.05$) is of special care in order to study low luminosity in galaxies.

The main improvements of the catalog over the standard SDSS release (in addition to the matches to other catalogs) are a better calibration and explicit description of the geometry. In brief, it includes structural measurements, k-corrections, peculiar velocity corrections, and quality checks of many objects which help the treatment of data for specific analysis.

2.3 AUTOMATED MORPHOLOGICAL CLASSIFICATION OF THE SDSS-DR7 SAMPLE

Morphological classification has its issues. First of all, at high redshifts most galaxies seem to not fit in the Hubble's tuning-fork diagram. Second, there is a large kind of objects which seems to not fit in any class or fall in a clear box of galaxies defined by certain features [19]. Most of the problems arise by visual inspection and the parameters used to classify an object in a given type. The definition of early-type and late-type is not very clear, even today fundamental questions raised after Hubble's definition remains unanswered.

Concerning this situation, [19] instead of defining a closed type with its specific characteristics, use a continuous population of galaxies with some canonical objects. Then each galaxy does not belong to a certain type but a probability of belonging to a given class is assigned. To check the method, visual inspection can be performed if the sample is small but becomes an impossible task if the sample is like the SDSS. Thus, determining morphology in an automated way could be achieved using a few parameters as concentration, asymmetry, clumpiness, colors and color gradients. The classification of galaxies conducted by [19] was based on support vector machines (galSVM) which assign probabilities instead of unique classes.

The sample used by [19] was based on the SDSS DR7 spectroscopic sample. Data with redshift $z \leq 0.25$, good photometry, clean spectra (not too close edges, not saturated or not properly deblended) were chosen. In total, 698.420 objects for automated classification were used.

Support vector machines (SVM) is a machine learning algorithm that tries to find the optimal boundary between clouds of points in a N-dimensional space. Benefits that can be obtained using this method lies in the way it deals with the number of dimensions that can be unlimited and it does not deliver a binary tag but a probability of belonging to a given class. The SVM needs a training sample, which in this case is typically built using a visually classified subsample. Misclassification can raise up because most of visual catalogs are built up with the brightest objects, leading to problems when classifying fainter ones. The goal when using the SVM is to group galaxies into four main classes: E, S0, Sab and Scd, where E/S0 belongs to early-type and Sab/Scd to late-type. The morphological index T is the direct way a galaxy is assigned into a class. E: $T < 1$, S0: $T = 1$, Sab: $2 < T < 4$ and Scd: $4 \leq T \leq 7$. Irregular objects $T = 6$ are no a big population so they are included into Scd class.

The sample was processed in two steps. First, objects are cataloged as early-type containing

elliptical and S0 galaxies, or late-type which goes from Sa to Scd/Im. Later on, objects are re-classified but the training set now only contains early-type and late-type galaxies. It can be interpreted as a conditional probability where one wants to know the probability of being S0 or E given that it is an early-type or the probability of being Sab or Scd given that it is a late-type object. Thereby, finally an object is tagged with six probabilities. Two broad classes early-type and late-type and four subclasses E,S0,Sab,Scd. The different steps used to select the final sample is shown in [Figure 10](#). There are a lot of parameters in the SDSS database which are related to

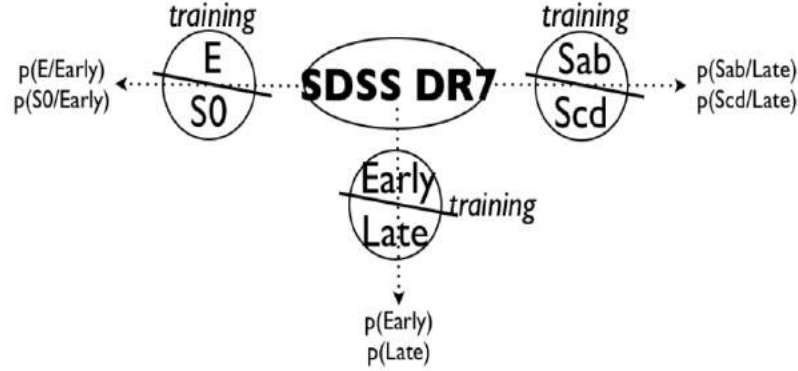


Figure 10: Scheme showing the procedure used to classify galaxies with the SVM. It is shown the two broad classes of early-type and late-type which is the first training sample and the four subclasses which are the result of a conditioned probability on the first sample [19].

morphology. A few of them were used as color ($g - r, r - i$) k-corrected, shape (ISOB/ISOA in the i-band and $DEVAB_I$) and a high concentration ($R90/R50$) in the i-band. The parameters ISOA and ISOB are the isophotal minor and major axes and $DEVAB_I$ is the De Vaucouleurs fit b/a. R90 and R50 are the radii containing the 90% and the 50% of the petrosian flux. They observed obvious correlations with the probabilities like if concentration increases and color turns redder, probability of being elliptical increase too.

It has been remarked that maybe fainter objects are not well represented in the training which could lead to a misclassification. However, the probability values seems to be independent of the galaxy brightness as [19] has checked, at least up to the magnitude limit of the sample. Then, even for the faintest objects the algorithm can find the closest class. To check the robustness of the sample, ten new runs with different training sets were performed. As a result, changing the training set affects the probability of a given galaxy in $\sim 12\%$. This scatter is compaible and even less than when people performs visual classifications on the same sample. Only a 0.4% of the whole sample is classified as uncertain but the majority are therefore close to one or two morphological classes.

An extra test was performed comparing *Galaxy Zoo* samples. They found a clear correlation between the number of votes given by people to classify an object into a given type and the probability computed in an automated way by the galSVM. Thus, the probability measurement indeed measures the robustness of the classification for a given object. Finally, it is important to notice that expected trends are observed like elliptical and S0 are less scattered and redder, while Sab and Scd are bluer. It seems to be two distict populations for Sab and for some Scd galaxies. One red population and the other one lying in between the blue cloud and the red sequence in the green valley. Most of those objects are in fact edge-on spirals probably reddened by the dust.

2.4 SELECTION CRITERIA AND CORRELATIONS

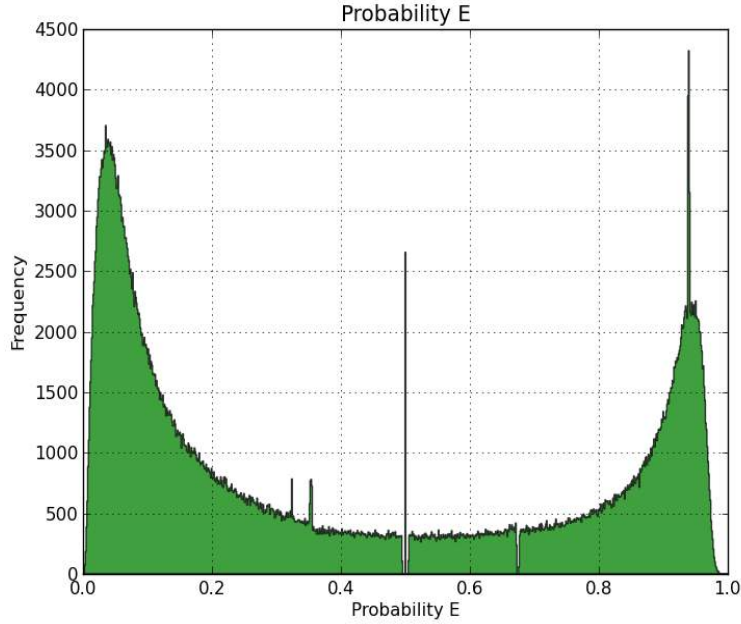


Figure 11: Probability distribution for early-type objects is shown. The probability computed is indicated in the x -axis and the frequency on the y -axis. Then, an object is tagged with a global probability of belonging to the early-type which can be E or $S0$ if the probability is high, or Sab and Scd if it is low. A segregation between early-type (left-hand) and late-type (right-hand) objects can be seen in the diagram.

According to Huertas-Company et al. (2010) [19] we count with a total of 698.420 objects which have four probabilities of belonging to a given subclass ($E, S0, Sab, Scd$) and a probability of belonging to a main class as early-type. Late-type probability is implicit since $P(Early - Type) + P(Late - Type) = 1$. First of all, the probabilities were checked to find out a criteria to cut off the different subclasses and obtain a range where it is safe to assume that an object belongs to an specific class. Thus, Figure 11 and Figure 12 shows respectively, the un-normalized histograms for the different probabilities extracted from the database mentioned above.

In Figure 11, it has been plotted the global probability of the sample of being an early-type object. Galaxies which have been tagged by the galSVM as purely early-type must be to the right-hand side which contains the largest probabilities, while spiral types as Sab and Scd must be on the left-hand side where the low probabilities reign. There is an obvious segregation between two global categories covering two populations with different features. It can be noticed how the probability decreases while approaching to the 50% where galaxies cannot be put into an specific sample but into two different classes. From this point up to the end (to the left-side) it begins to increase again.

Additionally, as shown in Figure 12, the probability for the four subclasses was plotted in the same way. It is important to understand that the same object is tagged with four probabilities fulfilling the constraint that $P(E) + P(S0) + P(Sab) + P(Scd) = 1$. Then, as shown before there is not a closed class but a continuous classification of an object. In Figure 12, individual probability of subclasses distributions are shown. In general, all histograms tend to decrease while approaching

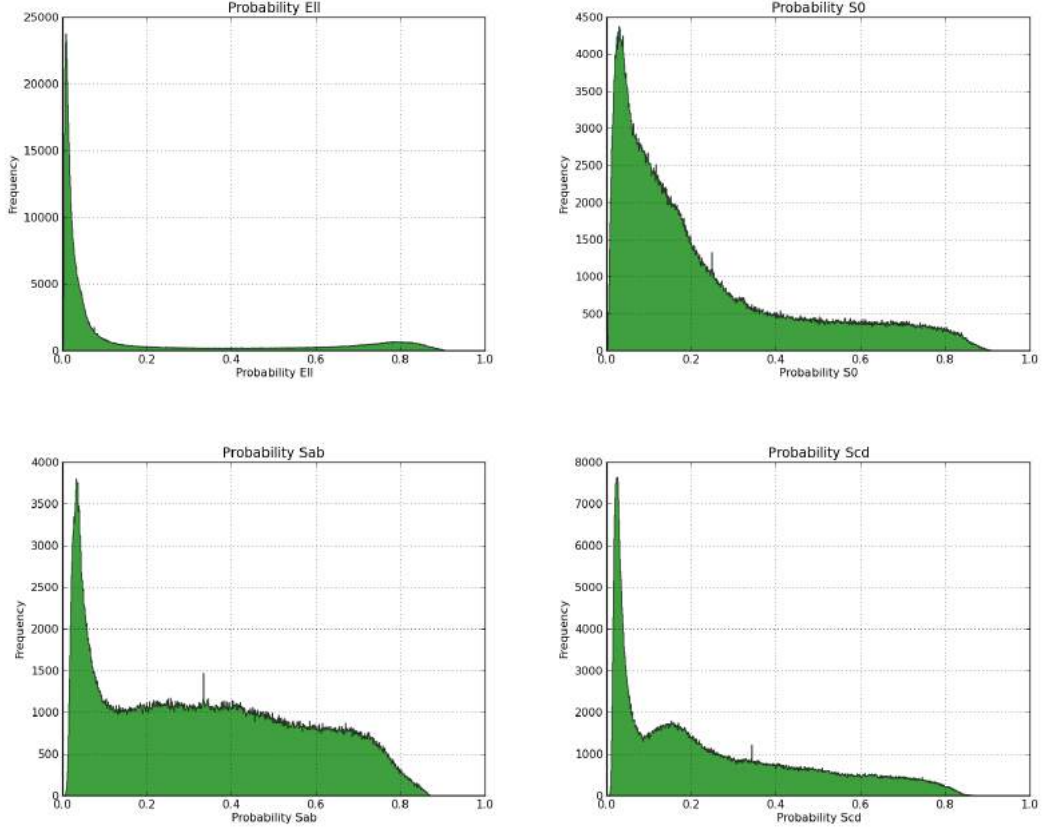


Figure 12: Distribution of the E,S0,Sab and Scd probabilities. (a) panel shows the probability of a galaxy of being Elliptical, (b) is the probability of being S0-type, and (c),(d) the probability of being Sab,Scd respectively.

to a probability of one. Something that is not new because objects cannot be classified into a stiff subclass, so we can not have objects classified with 100% certainty. Low probabilities in all the subclasses consequently mean that the galaxy is really far away from that specific subclass. Constraints over the early-type probability must be performed to split the main sample into galaxies which really seems to be early-type and late-type. In [Figure 11](#) we can see that in the middle of the distribution one is not able to clearly see if a given galaxy is spiral or elliptical because both probabilities are equal or really close to each other. Therefore, we took as a cut-off point $P(\text{Early} - \text{Type}) > 0.8$ to ensure that we have a sample of elliptical galaxies (*E or S0*) and $P(\text{Early} - \text{Type}) < 0.2$ for a sample of spiral galaxies (*Sab or Scd*). So we can compute a conditional probability using these conditions and get the new probability distributions for the four subclasses (*E,S0,Sab,Scd*).

So, In [Figure 13](#) we can see the new probability distributions once their probabilities have been conditioned. In panel (a) there are represented the probability distributions for elliptical objects as *E* and *S0*. In panel (b) there are those probability distributions for the spiral sample (*Sab,Scd*). We ought to take in mind that these distributions correspond to the case when we filtered by objects having high values of early-type probability ($P(E)$). Late-type galaxies show up here the lowest probabilities to be found as expected while early-type the largest. Clearly our new sample is built by elliptical objects which indeed show the same feature as the global probability which is

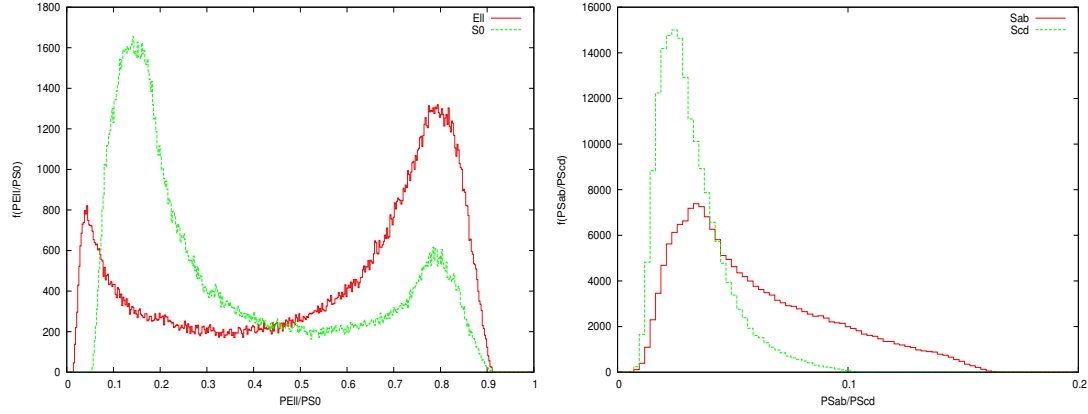


Figure 13: Conditional probability distributions for early-type sample. On the left side is shown in the x -axis the probability of being E (red line) or S0 (green line) and in the y -axis the frequency. On the right side is plotted in the x -axis the probability of being Sab (red line) or Scd (green line) and in the y -axis the frequency

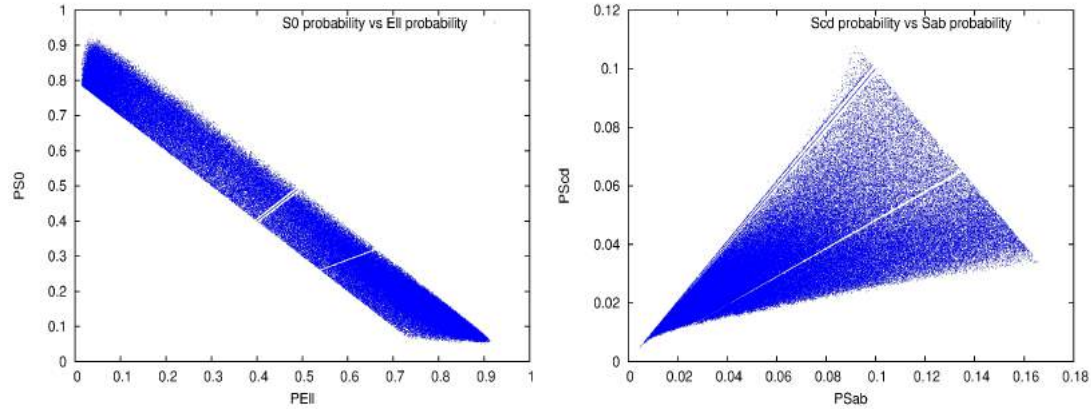


Figure 14: Correlations between the conditional probability (early-type sample) of subclasses belonging to the same global class. (a) shows the correlation between the probability of being S0 against being E. (b) correlation between the probability of being Scd against being Sab.

that E and $S0$ objects mix-up due to the nature of the classification method. Thus, we can assess this in Figure 14 where we can see in panel (a) how elliptical galaxies are strongly correlated while spiral sample in panel (b) is really spread out showing a weak correlation. The higher the probability of being E the lowest of being S0 and vice versa. We cannot say the same thing for Sab and Scd, so a large difference between both types can be observed.

Same analysis is done but now with the late-type sample which has been obtained conditioning the global probability to be $P(E) \leq 0.2$ as shown before. Thus, the new sample is for galaxies which have a high probability of being early-type, either Sab or Scd. in Figure 15 probability distributions for late-type samples are shown to find out the new features and correlations. For E and S0 subclasses, the lowest probabilities are found as expected because now it has been chosen the late-type objects from the main sample. Again, two different populations are observed which are built up from Sab and Scd types. Then, correlations between the probabilities of galaxies of the same global class is expected to happen because the sample is *biased* to late-type galaxies.

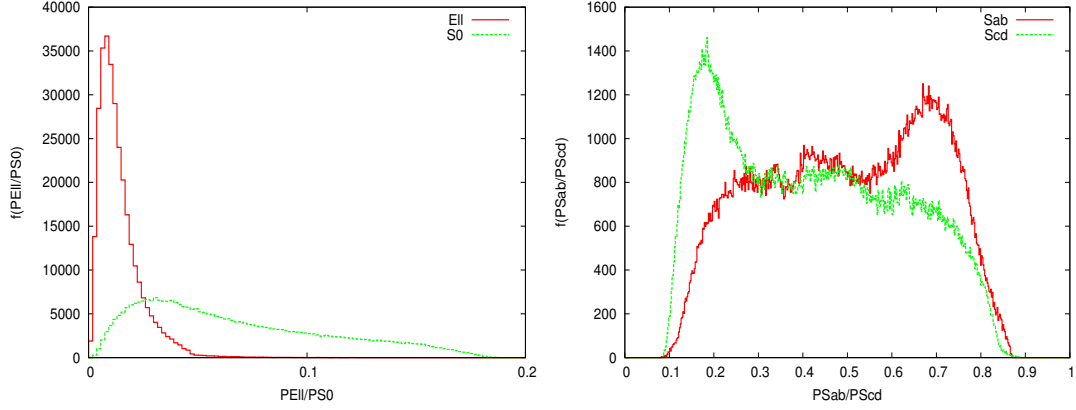


Figure 15: Conditional probability distributions for late-type sample. On the left side is shown in the x -axis the probability of being E (red line) or S0 (green line) and in the y -axis the frequency. On the right side is plotted in the x -axis the probability of being Sab (red line) or Scd (green line) and in the y -axis the frequency

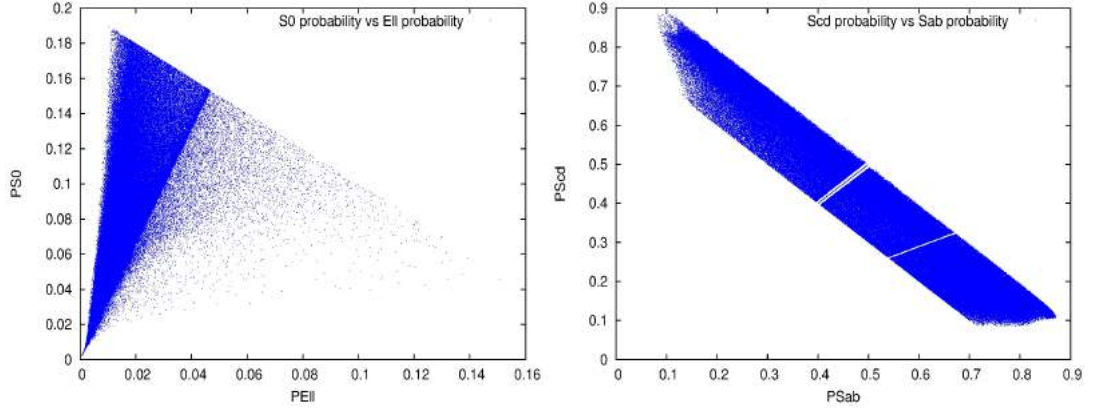


Figure 16: Correlations between the conditional probability (late-type sample) of subclasses belonging to the same global class. (a) shows the correlation between the probability of being S0 against being E. (b) correlation between the probability of being Scd against being Sab.

In [Figure 16](#) correlations between conditional probabilities for same global classes are plotted. Thus, higher the probability of being Sab the lower of being Scd and vice versa. There is a strong correlation for late-type objects and a weak one for early-type as expected.

Once we have carefully selected our new dataset where we are sure that we have those objects that better fit into a spiral or elliptical type, it is easy through the correlations shown in [Figure 14](#) and [Figure 16](#) to define a criterion to distinguish between the subclasses. This is, in [Figure 14](#) if $P(S0) \geq 0.5$ and $P(E) \leq 0.5$ the galaxy is a S0 type while if $P(S0) \leq 0.5$ and $P(E) \geq 0.5$ the galaxy is an E type. Same way, focusing on the (b) panel of [Figure 16](#) late-type constraints over the probability can be achieved. If $P(Scd) \geq 0.5$ and $P(Sab) \leq 0.5$ the galaxy is a Scd type, while if $P(Scd) \leq 0.5$ and $P(Sab) \geq 0.5$ the galaxy is a Sab type. Then, the whole sample proposed by [19] was safely divided into subsamples which contain galaxies with less uncertainty of belonging to that given category.

2.5 DATA TESTS

Data must be checked to verify the integrity and physical reliability. Thus, checking if the probabilities are biased against the redshift or if the galaxies does not follow the regular shapes of the fundamental plane must be taken into account.

Plotting probabilities against the redshift as shown in [Figure 17](#) helps us to understand if there is a kind of data error or bias in the classification scheme. Different probabilities seem to be well distributed. There is not an specific redshift where a given type of galaxy group in. The redshift goes from 0 to 0.25 as expected from the main sample given by [\[19\]](#).

2.5.1 Fundamental Plane

Before describing the units conversion and the fundamental plane performed for our whole sample, let's see what is our final dataset and why certain objects were rejected. As it was said before, Huertas-Company et al. (2010) [\[19\]](#) provided us a dataset with a total of 698.421 objects. A few of them have negative values of redshifts which means of course that cosmological relations can not be used to estimate the distance to those galaxies. Thus we took this into account in the final sample to get objects with well measured distances. The first step is to match the VAGC and SDSS properties with those in Huertas-Company, then, after performing this we reduce our original sample to 677.886 because a few *Object-Id* from Huertas-Company changed in other data releases. Once this is done, we selected our spiral and elliptical sample taking into account the criteria about their probabilities exposed above and adding that they must satisfy that $z \geq 0.005$ with $zwarning \equiv 0$ which is a flag provided by the data to select given objects of interest. In this data set there is a total of 173.747 elliptical galaxies and 292.281 spiral galaxies. However, we must split these samples into the four subclasses *E*, *S0*, *Sab*, *Scd* according to each selection criteria given form [Figure 14](#) and [Figure 16](#) and same redshift constraints. Therefore, we end up with a total of 114.754 *E-type*, 48.769 *S0-type*, 151.031 *Sab-type* and 106.606 *Scd-type*. Finally our final sample was reduced from 698.421 to 421.160 galaxies which fit more in a given classification type.

A relation found by Sandra Faber and Roger Jackson similar to the Tully-fisher relation but for elliptical galaxies it is known as the Faber-Jackson relation. It is a relation between the velocity dispersion in the center of ellipticals (σ_o), and the luminosity, which scales as: $L \propto \sigma_o^4$, or in logarithmic form: $\log(\sigma_o) = -0.1M_B + Const.$

Various relations exist between the parameters of the elliptical galaxies. So, the fundamental plane emerges from asking if whether a relation exists between observables of elliptical galaxies for which the dispersion is smaller than that of the Faber-Jackson relation [\[28\]](#). It is known that the effective radius of normal elliptical galaxies is related to the luminosity, i.e, it is related to the surface brightness. Thus, the average surface brightness follows: $R_e \propto <I>_e^{-0.83}$, so that $L = 2\pi R_e^2 <I>_e$. From these relations it is valid to ensure that: $L \propto R_e^2 <I>_e \propto <I>_e^{-0.66}$ or $<I>_e \propto L^{-1.5}$. Then, a relation with the luminosity emerges and tell us that more liminous ellipticals have smaller surface brightness. From all the relations shown above, it can be noticed that L is related to σ_o , and therefore, σ_o , $<I>_e$, and R_e are related to each other.

The distribution of elliptical galaxies in the 3-dimensional parameter space (R_e , σ_o , $<I>_e$), are located near a plane defined by $R_e \propto \sigma_o^{1.4} <I>_e^{-0.85}$. This is the "*Fundamental Plane*" which in logarithmic form look like:

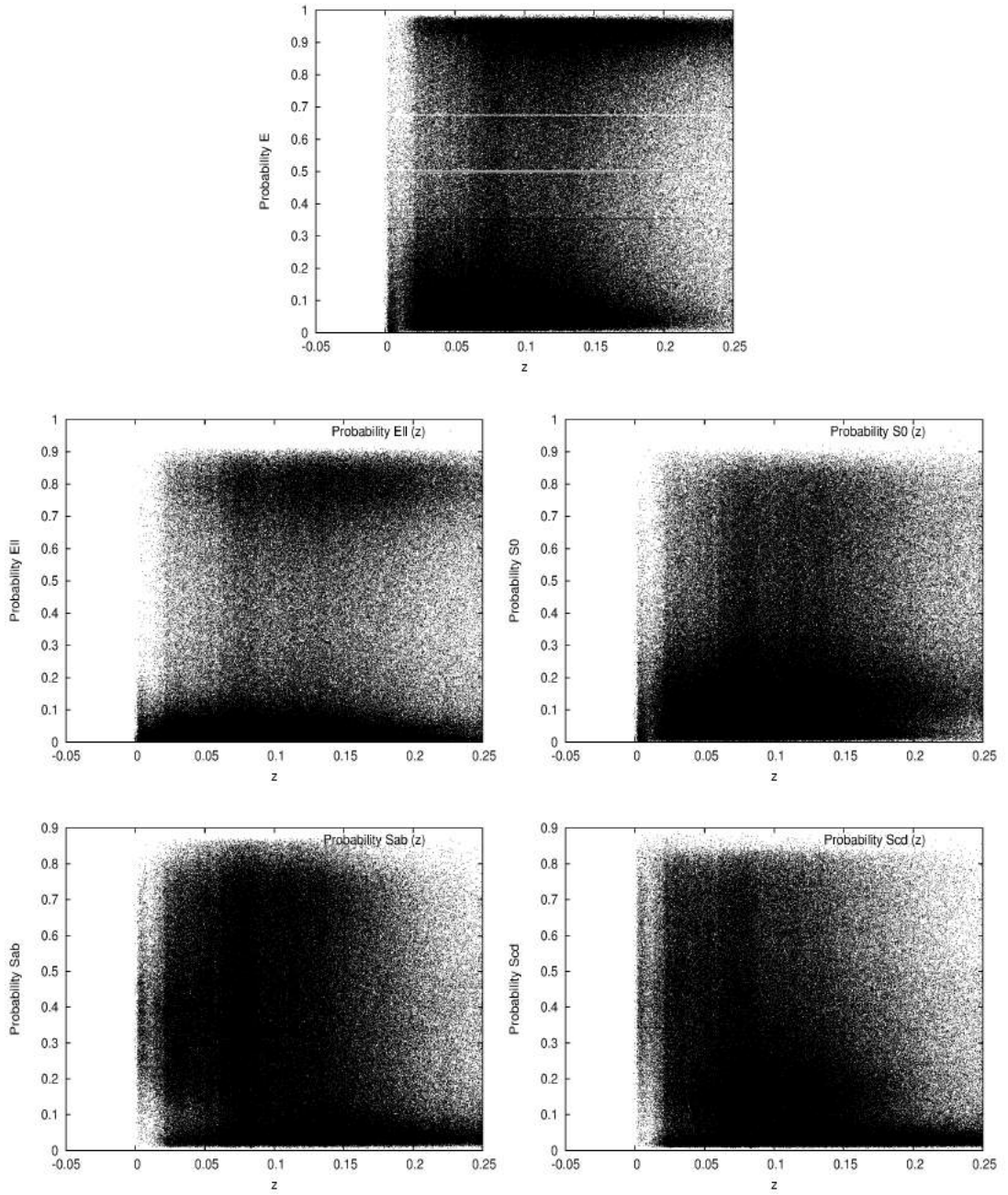


Figure 17: Probabilities distribution against the redshift. In the x -axis is the redshift while in the y -axis there is the probability. The first plot shows the probability of being an early-type galaxy while the other four panels from left to right shows the probability of being E, S0, Sab and Scd respectively.

$$\log R_e \equiv 0.34 < \mu >_e + 1.4 \log \sigma_o + \text{Constant}$$

As shown by [28] in the Figure 18, the fundamental plane is decomposed in four projections which show the different relations and correlations between the parameters that comprise it.

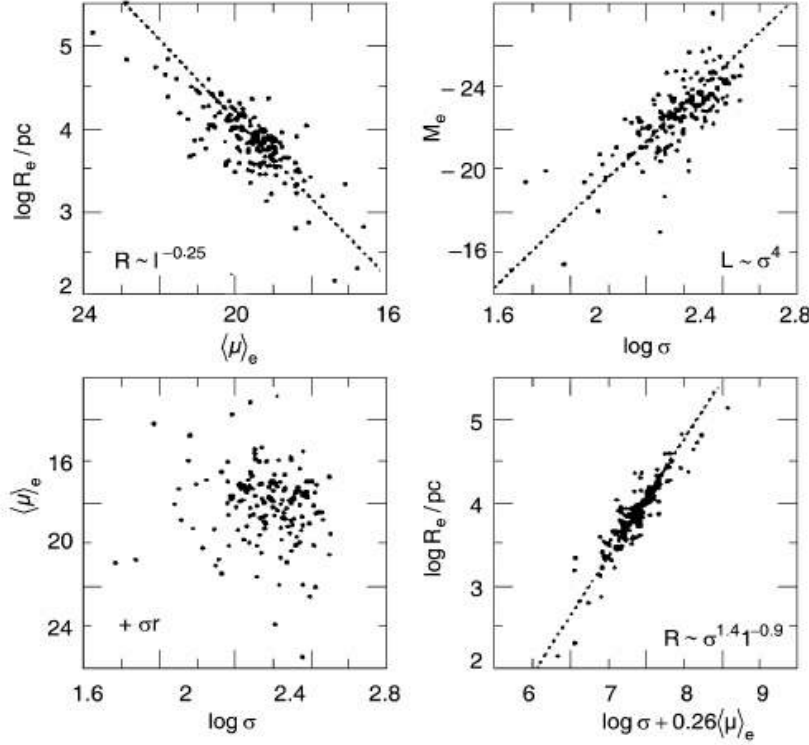


Figure 18: Fundamental plane projections onto different two parameters planes. Upper left: relation between radius and mean surface brightness. Upper right: Faber-Jackson relation. Lower left: mean surface brightness and velocity dispersion relation. Lower right: linear relation between radius and a combination of velocity dispersion and surface brightness [28].

2.5.2 SDSS units: Fundamental Plane

The units of the VAGC follows the prescription of the SDSS main sample. It is useful to change the units to physical units to analyze the distribution of the early-type galaxies in the fundamental plane. Of course, we have early-type and late-type objects in our sample, then the fundamental plane analysis will be carried out to everyone of them, albeit is strictly often performed for elliptic objects.

First of all, it must be noticed that velocity dispersion σ is given in $[km s^{-1}]$ which it is not needed to be transformed. However, the characteristic radius R_0 is given in $arcsecs$. This measure corresponds to the angular size of the object, then we must be able to compute the distance of a given object to calculate the characteristic radius in some known physical units as parsecs for example. Thus, from Equation 1.12 in Chapter 1 the integral can be computed once the

redshift for every object has been extracted from the data. Here, the $\Omega_M = 0.3$ and $\Omega_\Lambda = 0.7$, thus $\Omega_k = 0$ because these three quantities can not be higher than one. The Hubble distance $D_H = c/H_0$ where $c = 300000 \text{ km s}^{-1}$ and $H_0 = 100 h \text{ km s}^{-1} \text{ Mpc}^{-1}$. It is important to notice that throughout this procedure the value of h has been taken equal to one. All comovig distances are calculated to every object which has been classified into one of the four sub-samples as Ell, S0, Sab or Scd types. Once the comovil distance is known, it is possible to apply the Equation 1.13 in Chapter 1 which corresponds to the angular diameter distance of an object and it is related to the comoving and the redshift (z) of an object. Finally, knowing the angular diameter distance of every object and using the characteristic radius in $R0' [\text{arcsec}]$, the characteristic radius in Mpc can be obtained through $R0 [\text{Mpc}] = D_A R0'$. The scheme shown in Figure 19 exposes the different parameters obtained to compute the characteristic radius in physical units.

According to the data we have been working with, surface brightness obtained from Sérsic's profile fit is given in some kind of tricky units used by the SDSS as *nanomaggies/arcsec*². A "maggie" is the flux f of the source relative to the standard source f_0 (which defines the zeropoint of the magnitude scale). Therefore, a "nanomaggy" is 10^{-9} times a maggy. To relate these quantities to standard magnitudes, an object with flux f given in $n\text{Mgy}$ has a Pogson magnitude [3]:

$$m = (22.5 \text{ mag}) - 2.5 \log_{10}(f) \quad (2.2)$$

Then is easy to obtain our surface brightness parameter in mag/arcsec^2 which is much easier to work with, just by replacing it into the flux of Equation 2.2. Moreover, the standard source for each SDSS band is close to, but not exactly the AB source (3631 Jy), meaning that a *nanomaggy* is approximately $3.631 \times 10^{-6} Jy$.

Once the parameters have been tranformed to physical units, comparing our samples with the distributions on the fundmental plane is the next main step to verify if our data is behaving in a proper way. As shown by [28], the four projections of the characteristic radius, surface brightness and velocity dispersion must be performed, however it has to be plotted for each band used. Therefore, there is no just one fundamental plane but five where one is able to follow a given feature in each band. From Figure 20 to Figure 24 the fundamental plane in each band in order (u, g, r, i, z) is shown for the four sub-samples namely Ell, S0, Sab, Scd.

Thus, Figure 20, Figure 21, Figure 22, Figure 23 and Figure 24 are the plots of the fundamental plane for each petrosian band u, g, r, i, z . All the panels are listed in the same order, thus each one shows up the behavior of the same population with the same parameres in different bands. So let's focus just in a general description of each panel per galaxy type to give a general view of those distributions.

In general u and z bands are noisy, thus the scatter in each panel is obviously more prominent for these specific bands. However, there is an evident feature which all bands share when the velocity dispersion is used (panel b, c, d) caused by the sensivity of the instrument. A cut-off line near $\log_{10}(\sigma) = 1.57$ which we identified as the lower velocity which can be measured by the intrument corresponding to $\approx 37 \text{ km s}^{-1}$. Additionally, an upper cut-off line can be observed but this one is caused by the maximum value of velocity which can be measured so can be interpret as a saturation induced by the same intrument.

While we move from u to z according to panel a , it is evident how elliptical galaxies tend to occupy places where the surface brightness and the scale length are smaller. A curious feature

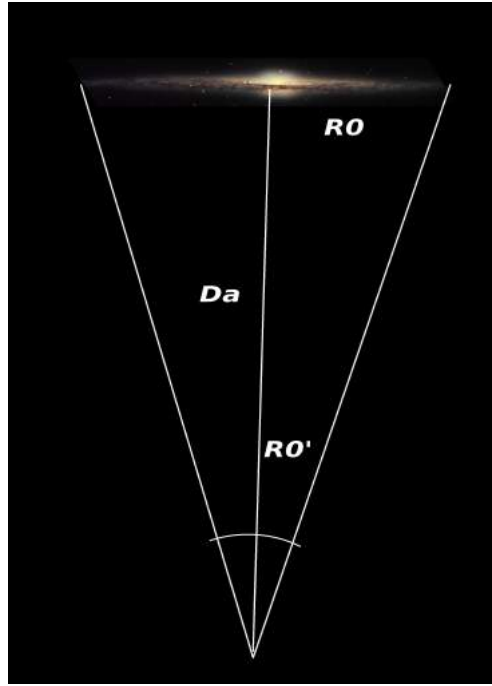


Figure 19: Relation between the angular diameter distance and the Sérsic parameter $R0'$ in this case to obtain the same quantity $R0$ but in Mpc .

corresponds to a population of disk galaxies (*Sab, Scd*) which lie exactly by the side of the elliptical ones. Evidently, these galaxies were classified as disks but maybe with parameters similar to the ellipticals because they look redder by the dust or their bulge is more predominant than their own disks as noted by [19]. When we observe panel *b*, which represents the well-known Faber-Jackson relation between the absolute magnitude in a given band and velocity dispersion, we see how all samples look more luminous while going from bluer to redder bands. All distributions show an increase in luminosity with velocity dispersion, as expected from Faber-Jackson. Moreover, elliptical galaxies are more luminous and have higher velocity dispersion than spiral ones as expected.

Panel *c* represents a relation between the surface brightness and velocity dispersion. Elliptical galaxies are located in a specific place which looks like a little spheroid as expected. It is interesting how spiral galaxies of type *Sab* superpose just a little bit with the ellipticals while *Scd* tend to be really separated from them. Of course the same behavior described above for surface brightness and velocity dispersion depending on the classified type is valid here.

Finally, panel *d* shows a relation between the scale length and a combination of surface brightness and velocity dispersion. Once again two populations are evident either for spirals or ellipticals. When we introduce scale lengths we see how this features appear, then those populations are marked by this parameter. However, the distributions here shows a wide range and a different behavior of the mixed parameters which is specific of a given sample.

Fundamental plane analysis as has been said before, is only valid for those galaxies with an spheroidal shape. We performed it to the full sample just because we wanted to check-out some special features which can show up differences between different types of galaxies and indeed to check-up the integrity of this dataset.

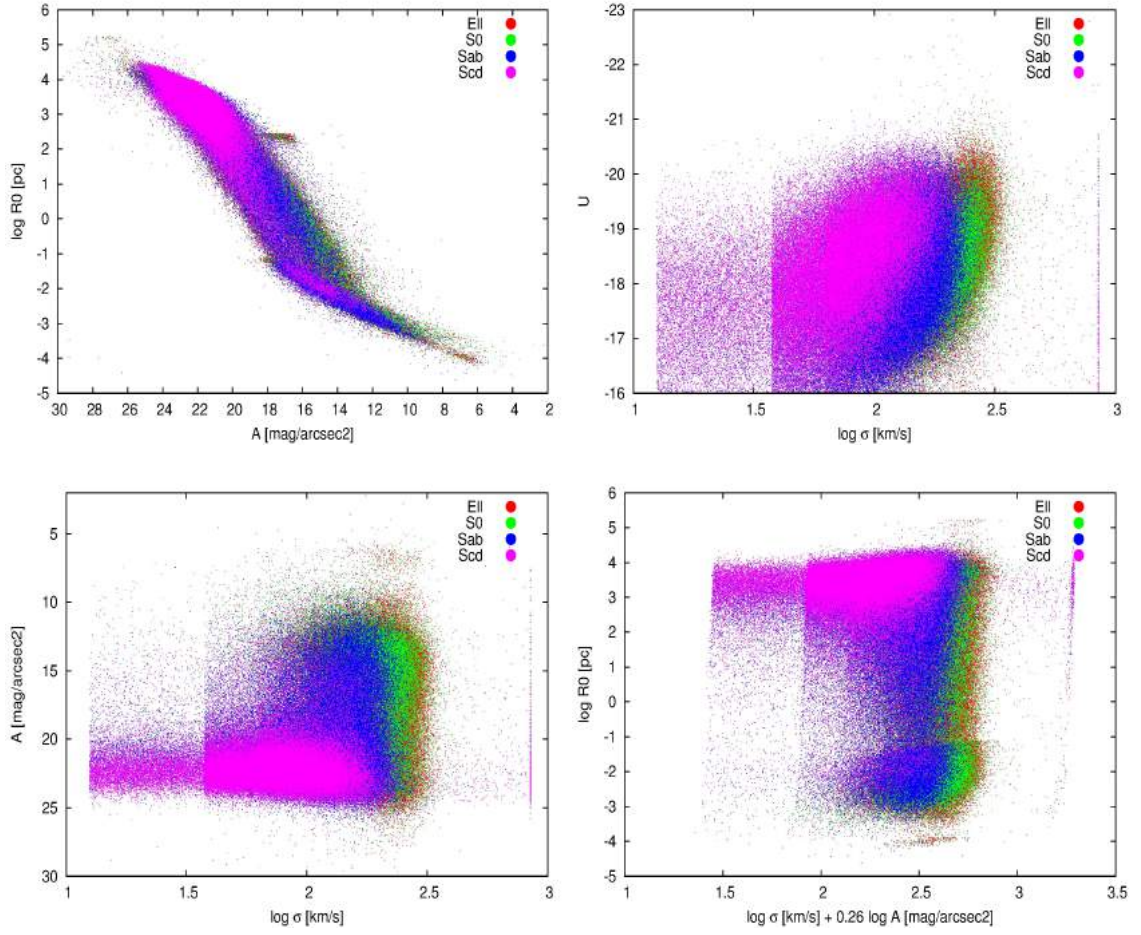


Figure 20: Fundamental plane in the u-Band. (a) panel shows the R_0 [pc] and A [mag/arcsec²] logarithmic Sérsic's parameters. A relation between the radius and the surface brightness. (b) panel shows the relation between magnitude in a Petrosian band with the velocity dispersion known as the Faber-Jackson relation. (c) the surface brightness - velocity dispersion correlation. Velocity dispersion is in $km\ s^{-1}$. Finally (d) panel is a relation between the radius and a combination of surface brightness and velocity dispersion.

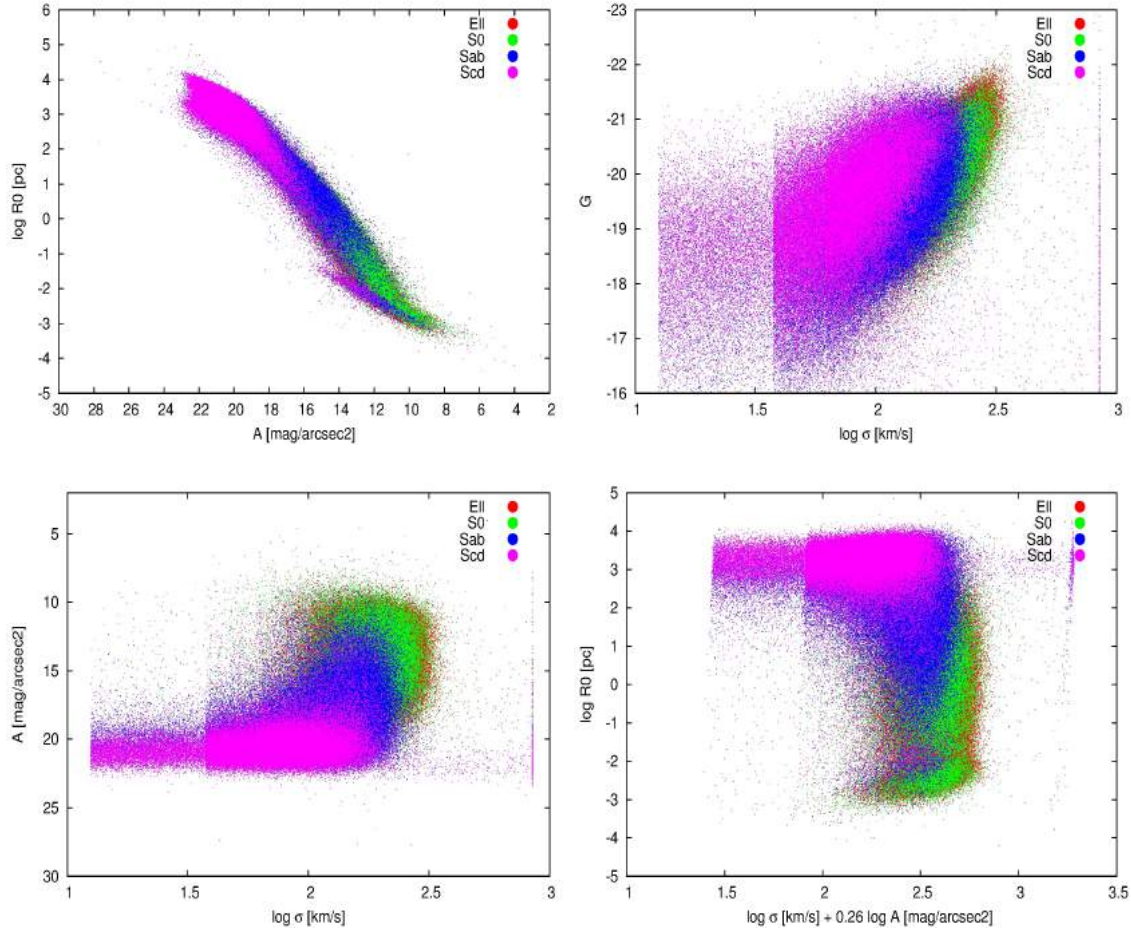


Figure 21: Fundamental plane in the g-Band. (a) panel shows the R_0 [pc] and A [mag/arcsec²] logarithmic Sérsic's parameters. A relation between the radius and the surface brightness. (b) panel shows the relation between magnitude in a Petrosian band with the velocity dispersion known as the Faber-Jackson relation. (c) the surface brightness - velocity dispersion correlation. Velocity dispersion is in $km\ s^{-1}$. Finally (d) panel is a relation between the radius and a combination of surface brightness and velocity dispersion.

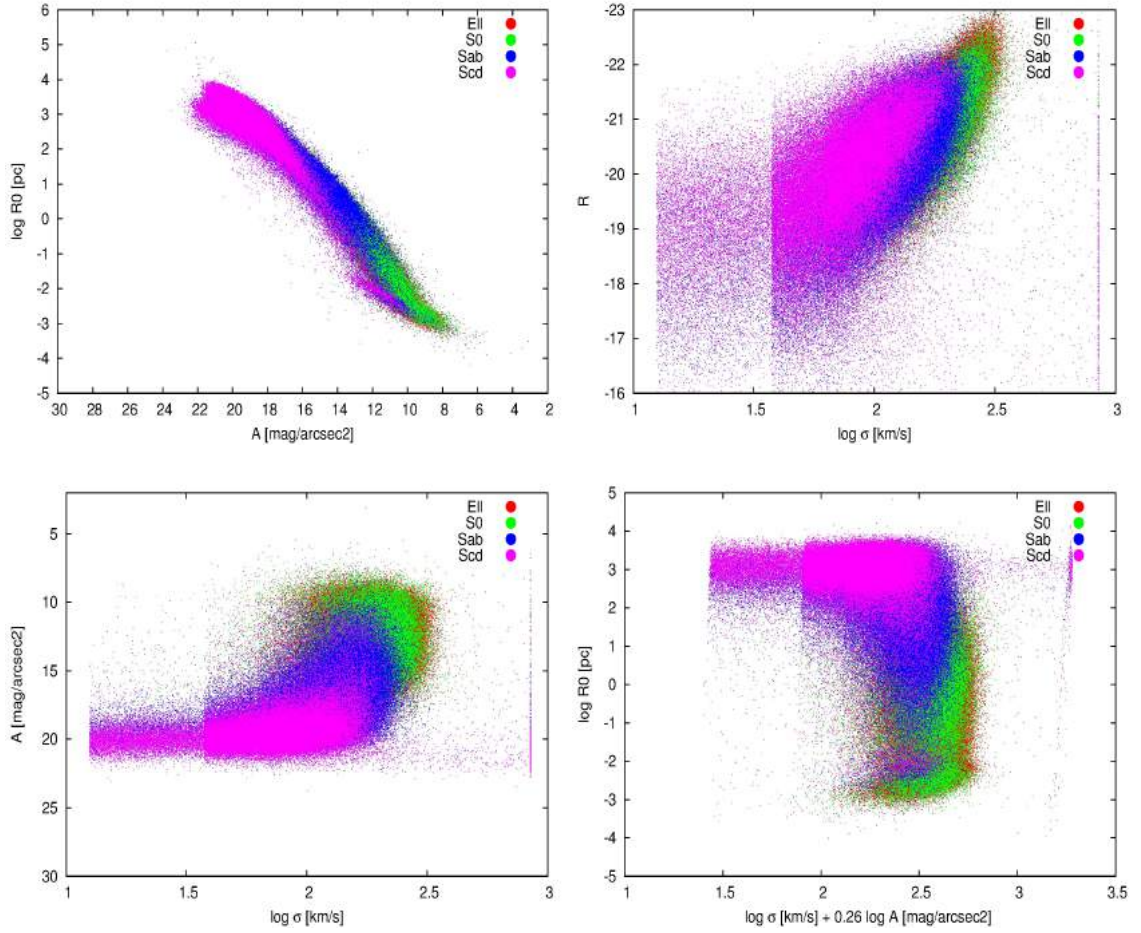


Figure 22: Fundamental plane in the r-Band. (a) panel shows the R_0 [pc] and A [mag/arcsec²] logarithmic Sérsic's parameters. A relation between the radius and the surface brightness. (b) panel shows the relation between magnitude in a Petrosian band with the velocity dispersion known as the Faber-Jackson relation. (c) the surface brightness - velocity dispersion correlation. Velocity dispersion is in $km\ s^{-1}$. Finally (d) panel is a relation between the radius and a combination of surface brightness and velocity dispersion.

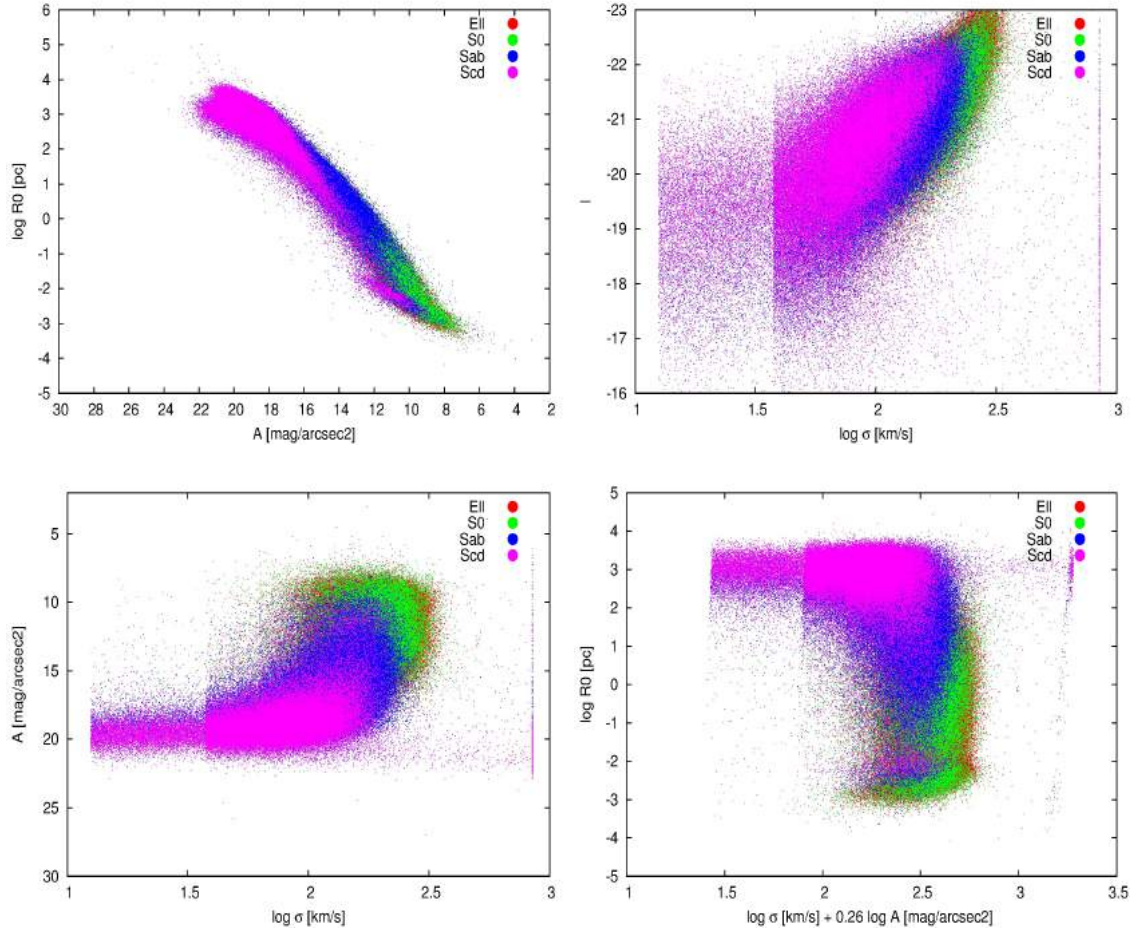


Figure 23: Fundamental plane in the i-Band. (a) panel shows the R_0 [pc] and A [mag/arcsec²] logarithmic Sérsic's parameters. A relation between the radius and the surface brightness. (b) panel shows the relation between magnitude in a Petrosian band with the velocity dispersion known as the Faber-Jackson relation. (c) the surface brightness - velocity dispersion correlation. Velocity dispersion is in $km\ s^{-1}$. Finally (d) panel is a relation between the radius and a combination of surface brightness and velocity dispersion.

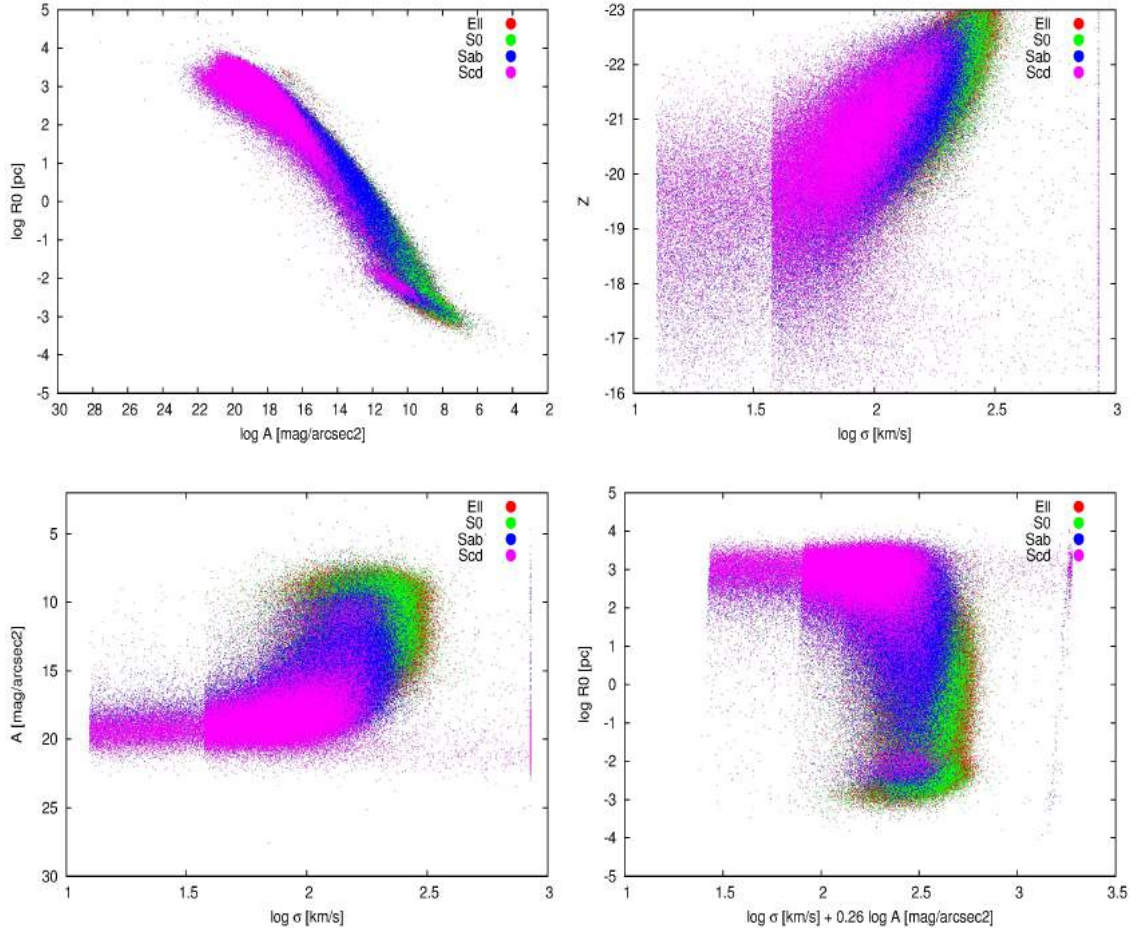


Figure 24: Fundamental plane in the z-Band. (a) panel shows the R_0 [pc] and A [mag/arcsec²] logarithmic Sérsic's parameters. A relation between the radius and the surface brightness. (b) panel shows the relation between magnitude in a Petrosian band with the velocity dispersion known as the Faber-Jackson relation. (c) the surface brightness - velocity dispersion correlation. Velocity dispersion is in $km\ s^{-1}$. Finally (d) panel is a relation between the radius and a combination of surface brightness and velocity dispersion.

2.6 SÉRSIC'S PROFILE PARAMETERS

Data have been already checked through the fundamental plane relations to ensure a good behavior of the selected samples. However, the distributions of each type helps to observe features that are properly of a given object. Galaxies are meant to show up a variety of properties which can vary from type to type, thus specific properties can be assigned to a canonical type which contains a continuous sea of physical parameters. Nature do not behave splitting galaxy types with absolute properties but with an uniform distribution where near types can overlap other ones. Figure 25 shows the CMD for the four sub-samples galaxies (Ell,S0,Sab,Scd). The

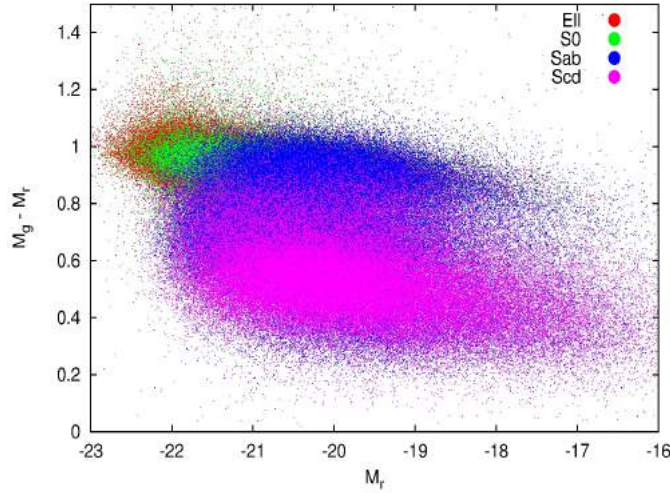


Figure 25: Color-magnitude diagram (CMD) built up with the Petrosian magnitudes g and r . In the y -axis it is plotted the color computed through the difference of magnitude in two distinct bands. In the x -axis the r -band magnitude. Ell type objects are plotted in red, S0-type in green, Sab in blue and Scd in purple. It can be observed how elliptical sample tend to be located in the red sequence while Scd type prefer the blue cloud, and a transition between early-type and late-type through Sab-type which locates in the so-called green valley.

petrosian bands used are the g and r with which one can obtain the color through the difference between two bands. Thus, plotting the color against a given magnitude which for this case is the r -band one can obtain a distribution of objects segregated by color. At the blue cloud are located the Scd galaxies (purple ones) but a piece of Sab type overlaps them (blue ones). However, Sab type are widely spread out in the so-called green valley overlapping the red sequence which is the place where S0 and Ell types are located. A considerable amount of Sab galaxies lie in the red population (ellipticals) and another on the green valley. Also as noticed by [19], most of these spiral galaxies seems to be two distinct populations, where the red ones by visual inspection were confirmed as edge-on galaxies reddened by dust. Moreover, expected features as a color segregation can be noticed where elliptical sample is in the upper-side where objects can be considered redder and Scd are low where objects are bluer. A continuous distributions of objects is detected from early-type to late-type filling the space. Though, galaxies are spread throughout in the magnitudes, it can be noticed how elliptical sample tends to have bigger magnitudes while spiral types tend to be less bright.

Color and magnitudes are not the only properties of galaxies which characterizes them. Velocity dispersion is indeed an important property which varies from type to type. In Figure 26, velocity

dispersion as a function of the r -band magnitude is shown. In [Figure 26](#) blurred line near 37

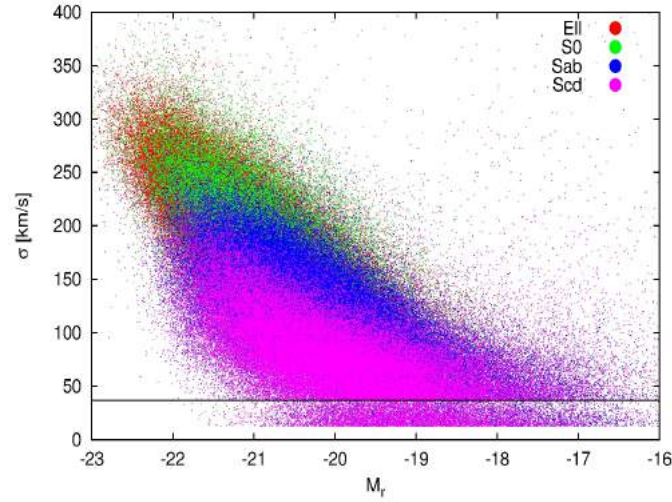


Figure 26: Velocity dispersion in [$km\ s^{-1}$] as function of the Petrosian r -band magnitude. Ell and S0 types tend to present the higher velocities while spiral ones the lower. An important feature can be observed at $37\ km\ s^{-1}$ where a horizontal line is blurred by data which is the limit of the survey in the measurment of this quantity. Data below this probably have wrong measures.

$km\ s^{-1}$ corresponds to the survey's limitation in measuring the velocity dispersion of a galaxy. the lowest velocity dispersion are registered by the Scd type which locates at the bottom of the plot. From spiral sample to elliptical sample there is an increase in the velocity dispersion where galaxies catalogued as Ell-type tend to have the higher ones. Even though galaxies are spread through different magnitudes, there is present a little tilt that shows how brightest objects tend to be indeed those which expose higher velocity dispersions. So, spiral and elliptical samples tend to occupy distinct places in the σ -magnitude diagram where the redder are those with higher velocity dispersion and the bluer those with lower velocity dispersion. Populations segregate in a proper way showing that instead of being a well splitted distribution of objects the nature of galaxies is a continuous where intermediate types overlaps each other.

However, as it has been shown the profile adjusted to the light distribution of galaxies is the Sérsic one, then a segregation of different types is expected because galaxies must be represented by some characteristic values of the Sérsic's parameters. Then, from [Equation 2.1](#) which corresponds to the Sérsic's brightness profile, which indeed the objects were fitted to, one is able to obtain the three different parameters that may play an important role in the light distribution of a given object as A , $R0$ and n . Those parameters were taken from the NYU-VAGC catalog in the five Petrosian bands (u, g, r, i, z). In [Figure 27](#) is shown the four type (Ell, S0, Sab, Scd) distributions in each plot for the three parameters ($A, R0, n$) from left to right, in the five bands (u, g, r, i, z) from top to bottom.

In general, the same features can be observed in g, r, i, z bands because u -band seems to look a little bit different. Four types tend to be distributed in different locations as expected, with characteristic values of the parameters. In the first column reading the parameter A from top to bottom one is able to see how Ell and S0 types are located where the surface brightness is higher while Sab and Scd is lower. In particular, both samples, the elliptical and spiral types tend to be closer in the u and z bands. The distributions tend to shift to the left side where objects are brighter when going from blue to red bands. While Ell and S0 are always really closer, the

Sab type tends to be always intermediate between Scd and ellipticals. The g,r,i bands are the best ones to show up the segregation between the used samples. All distributions shift to greater values of A as one goes through blue bands to the redder ones. Two distinct populations of redder galaxies are clearly observed, where a bit of them locate at higher values of A and the other one tend to be closer to the Sab types where both mix-up as shown in the CDM diagram.

The parameter $R0$ shows a different behavior compared with the surface brightness. Here, elliptical sample exhibits the lower values of the characteristic radius while the spiral sample tend to locate in the upper values. An obvious segregation into two distinct populations of Ell and S0 types is observed where a little amount of them locate at the bottom or the lowest values of $R0$. However, there is a significant cloud of Ell and S0 types which overlaps with Sab types in the middle of all distributions. In the u -band as always the distributions are kind of noisy because some constant values of the parameter where objects tend to locate are detected. Indeed the segregation in this band is not obvious because objects are well spread through the plot. As for the A parameter in the z -band segregation is less obvious than in other bands and a mix between early-type and late-type becomes notorious. In general, Scd type segregate very well and tend to occupy higher values of the characteristic radius and Ell and S0 the lower values. Sab type keep on being an intermediate kind of objects in the range of values taken by the distribution of galaxies. Once again, when going from bluer bands to redder all distributions shift to the higher magnitudes where the elliptical sample, in general, are more luminous. The range of magnitudes of spiral types is more widely spread.

For the n parameter in the u -band there is no an evident feature between different kind of objects. It looks like a cloud where all objects are collected in. Although they locate in a vast space it is important to notice how horizontal lines which corresponds to same n index values appear. The lowest and the uppermost horizontal lines belongs to a natural limitations where the observations were made. Then, n index is limited between 0 and 6 in value. Comparing with the other parameters the segregation observed here is lower. Elliptical galaxies Ell and S0 locate at upper values while spirals as Sab and Scd show lower values. The distribution of Scd which have been characterized for not being so spread out, over here looks like distributed in a wide range cloud as same as Sab. Only Ell and S0 types are in a tiny place of the diagram showing a smaller range of possible values. Once again, all distributions shift to the left side where brighter object place. There is no the same two population distribution shown by elliptical types as in later parameters. A few horizontal lines (saturation of objects in an specific value) can be observed.

2.6.1 *Distribution of the Sérsic Parameters Respect Petrosian Magnitudes*

Sérsic's parameters are too important to classify the main sample of *Ell*, *S0*, *Sab*, *Scd* galaxy types because knowing that those objects are apparently different like splitted into two main samples (Spiral and Elliptical), then one may think that all of them should have a defined range of Sérsic parameters which can help us to recognise some special features.

The new data have now correct redshifts and physical units which means that the surface brightness is in magnitudes per squared arcseconds and the characteristic radius is in parsecs. The histogram analysis then is made splitting the sample into the four subclasses and into the five Petrosian bands. Thus, for a fixed class and Sérsic's parameter the histograms can be analyzed according to the Petrosian magnitude. Moreover, a magnitude bin splitted data were extracted which is for a given Sérsic's parameter and Petrosian magnitude the behavior of each class can be tracked down through lower to higher magnitudes. Following this the histograms

shown in Figure 28 to Figure 33 were done. The first three figures are plotted for a fixed Sérsic's parameter and type, showing the behavior through Petrosian bands. The other three figures show the magnitude bin behavior.

First of all, in Figure 28 each plot shows the parameter A . From the top to bottom can be found the four subclasses *Ell*, *S0*, *Sab*, *Scd*, while from left-hand to right-hand the Petrosian bands are located in order u, g, r, i, z and color lines represent a specific sample covering magnitudes from -17 to -22 . Let's focus in the first row which are elliptical galaxies. Observing these objects it is evident two different populations reflected in a bimodality of more luminous distributions, reflecting the nature of our dataset. The shape of the distributions does not change much apparently which is important in a way that this parameter is well behaved through different filters and magnitude bins. Although, distributions tend to become thinner when going from blue to red bands and distributions move to lower values of A parameter. In the case of *S0* distributions are less spread out and show same behavior as *Ell* albeit there exists an evident feature and is that *S0* occupy slightly higher values of the parameter showing distributions shifted to the right opposite to *Ell* and independent of magnitude.

Looking at *Sab* objects we notice more tightened distributions in comparison with ellipticals. However, they move to lower values of A when going from blue to red bands as ellipticals independent of magnitude bins which can be interpreted as a global behavior of the parameter in different filters (because *Scd* shows up same behavior). A second population is visible only in noisy bands thus we are not able to assess this result. Galaxies between -19 and -21 in magnitude have higher frequencies than more luminous ones. Same is valid for *Scd* galaxies, although these are more tightened than firsts and are shifted to the right where occupy higher values of the parameter in comparison with other spirals. As it has been seen until now spiral galaxies *Scd* seems to be a well behaved dataset because the sample is less contaminated. It is remarkable how bands u and z are more noisy than others because distributions look more puffy along different types.

In Figure 29 from top to bottom we can find the four subclasses *Ell*, *S0*, *Sab*, *Scd*, while from left-hand to right-hand Petrosian bands are located in order u, g, r, i, z and color lines represent a specific sample covering magnitudes from -17 to -22 . All these plots are made for radius scale length R_0 . Elliptical galaxies in the first row show a strong feature which has been also observed in the fundamental plane analysis as two populations which become stronger when we use scale length parameter. Though, distributions move once again to lower values of scale length when going from band u to z . However, the second peak which is more tight and pronounced does not show an evident change as the second one. Here band u keeps on being more contaminated because it deviates from all other shapes observed in other bands. Same behavior is observed in *S0* type because they are still classified as ellipticals by [19] and tend to behave as same as *Ell*. There is something interesting in those distributions and is that *S0* objects have slightly high values of R_0 which is expected because the transition between galaxy types.

Observing the second big sample corresponding to spiral galaxies it is easy to see in comparison with ellipticals that they are shifted to the right which indicates higher values of R_0 in general. *Sab* type shows a second population really small unless in bands as u, z is more strong. These galaxy distributions are shifted to left side where are low values of R_0 when moving from blue to red bands. *Scd* galaxies behave as *Sab* but they have different features that mark the sample as their tight distributions, more regular and less contaminated. Second population here is smaller than in the first case but still evident. As expected from what has been said above these distributions are shifted to right side or to higher values of R_0 . Thus if we set a band it is possible to observe

how when going from elliptical to spiral types the samples shift to higher values of R_0 and become slimmer. Additionally, these distributions for spiral galaxies look like a log-normal distribution independent of band and magnitude as would be expected from analytical forms that scale length can have.

Finally, in [Figure 30](#) from top to bottom we can find the four subclasses *Ell*, *S0*, *Sab*, *Scd*, while from left-hand to right-hand petrosian bands are located in order *u,g,r,i,z* and color lines represent a specific sample covering magnitudes from -17 to -22 . All these plots are made for Sérsic's index n . In general there is a vertical line at the right side for every distribution which corresponds to the maximum value that can be measured by the instrument which is nearly $n = 6$. Other vertical line mostly visible in the *u* band are galaxies with really small Sérsic's index although it is magnified by the poor quality of the data in this band. Elliptical galaxies of type *Ell* show an expected behavior where all distributions are shifted to the right-hand where high values of Sérsic's index n lie. Distributions do not change when moving through different bands albeit *u* band is always irregular. However and in disagreeing with last behaviors of distributions according to other parameters, in this case distributions remain stable in different bands and they do not shift to a privileged side. Same things happen in the case of *S0* types where galaxies are characterized by higher values of n . Nevertheless, this is expected because it is well-known that elliptical galaxies are characterized by a De Vaucouleurs profile which takes $n = 4$. Thus, *Ell* and *S0* must be shifted to right in our plots as seen.

Spiral galaxies contrary to other parameter distributions are puffy instead of remain tight. *Sab* and *Scd* types in comparison with elliptical ones are shifted to lower values of n , which is expectable because disks models show that spiral galaxies use $n = 1$. Both distributions do not change significantly when moving from blue to red bands, although *Scd* type looks just a little bit shifted to smaller values of the parameter which shows the nature of these objects who are more "purely" disk objects than *Sab*. Although we are not able to distinguish between *Ell* or *S0* and *Sab* or *Scd* because they share similar values of their Sérsic parameter, it is obvious how elliptical galaxies are an independent dataset from spiral ones because they completely split off in certain values of this parameter.

After watching interesting features in each distribution for every galaxy type we decided to perform an analysis of same images but this time between ellipticals and spirals galaxies varying bin magnitude and petrosian magnitude. In [Figure 31](#), [Figure 32](#) and [Figure 33](#) are shown from top to bottom petrosian magnitudes *u,g,r,i,z* while from left-hand to right-hand there is each magnitude bin from -17 to -22 . Global behavior of parameters A, R_0, n keep on being equal to what has been said above because they are the same distributions analyzed before. Features, shifts and double population are still valid. However, what is most important here is to observe variations of parameters for a given type with magnitude. Indeed, in this case it is possible to compare each dataset, as spirals with ellipticals and clearly observe their differences.

According to what has been said in [Figure 8](#) from [Chapter 1](#), spiral galaxies have large surface brightness than ellipticals. In [Figure 31](#) it is possible to observe how each distribution segregates to given values of the surface brightness parameter. Elliptical galaxies have lower surface brightness values in comparison with spirals no matter the petrosian band nor the magnitude bin. Ellipticals *Ell* and *S0* have almost the same behavior, a difference arises in the spiral dataset because although they are shifted to large values of surface brightness, objects tagged as *Sab* type in comparison with *Scd* type have lower values of the parameter as expected. It is evident the transition between types of galaxy because there is a continuum between spirals and ellipticals due to the nature of the classification method.

In [Figure 32](#) distributions also splits out into two distinct populations. The higher values of $R0$ which is the Sérsic's scale length are shown by the spiral sample *Sab* and *Scd* while lower values characterizes the elliptical sample. Over here, there exists still a continuum where part of the spiral sample mix-up with the ellipticals. However, we can observe how the second population which is stronger in the elliptical sample, occupy near values where the second population of spirals are. Then, the second population in both distributions must be related through the parameters due to a misclassification because of their own look or the method. Elliptical dataset follows almost the same behavior and spiral sample tend to have larger values for *Scd* than *Sab*.

Finally, when we observe [Figure 33](#) distributions for Sérsic's index n tend to be more puffy than distributions in the another parameters. As seen before, most of the distributions for spiral data are quite slim and ellipticals tend to be just a little wide but in this specific parameter both spread out and tend to occupy a large range in values of n most of all the spiral sample. *Scd* type have the lowest values of the whole sample which indicates that they are more close to pure spiral type than *Sab* which are close to the elliptical sample like a transition state. By the way elliptical sample are totally shifted to the right side to higher values which indicates that this sample is close to a de Vaucouleurs profile.

Then, all the sample is behaving as expected for different types of galaxies so we will proceed to perform a specific analysis centered in disk galaxies as *Sab* and *Scd* data set because the model that we are going to apply was developed only for disk galaxies.

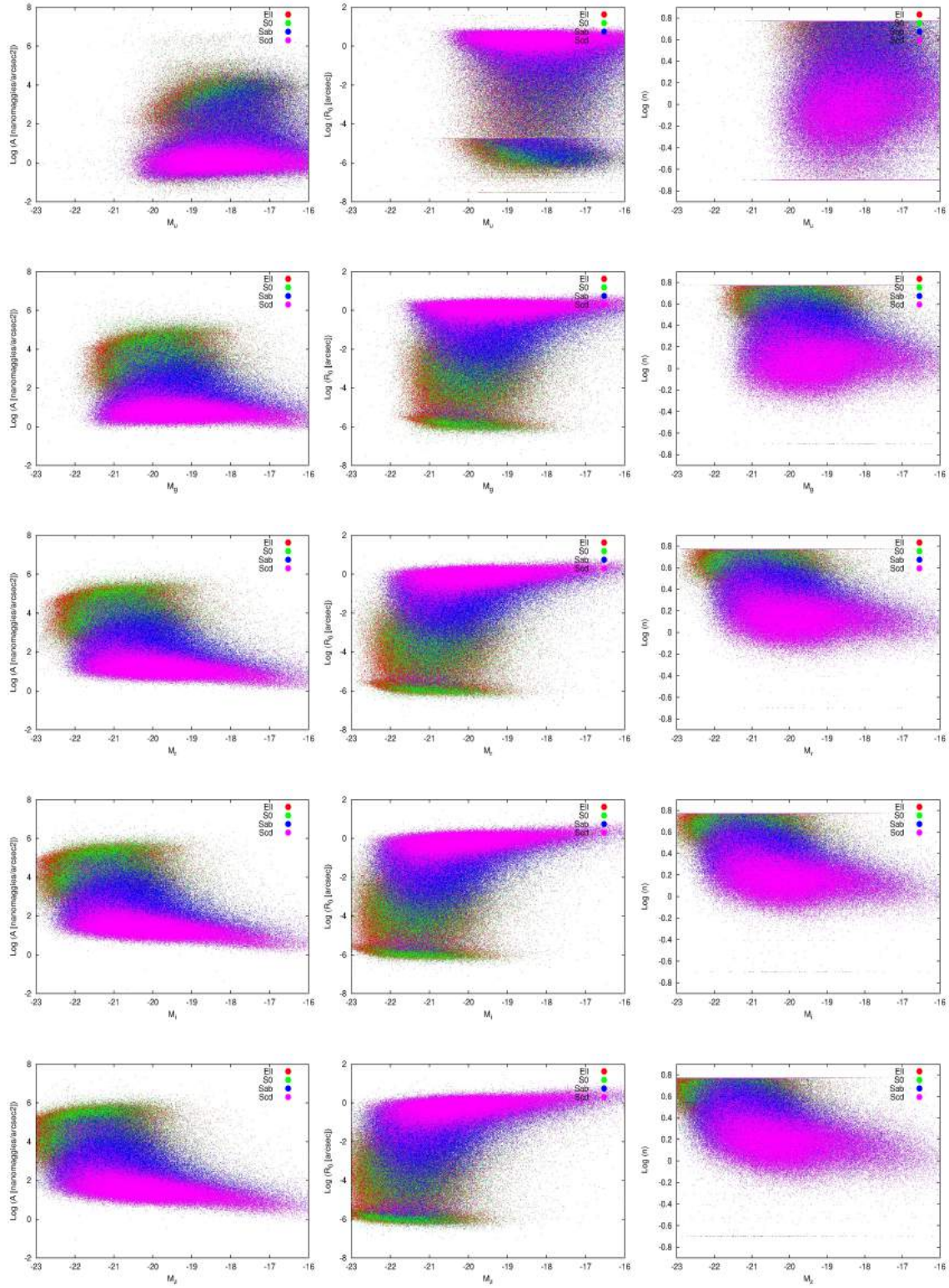


Figure 27: Sérsic parameters A, R_0, n as a function of Petrosian magnitudes u, g, r, i, z . Reading from left to right one can observe in the first column the parameter A in [$nMgy/arcsec^2$], R_0 in [$arcsec$] and n . From top to bottom the Petrosian magnitudes in order u, g, r, i, z . In each plot can be found the four subsamples Ell (red dots), S0 (green dots), Sab (blue dots) and Scd (purple dots).

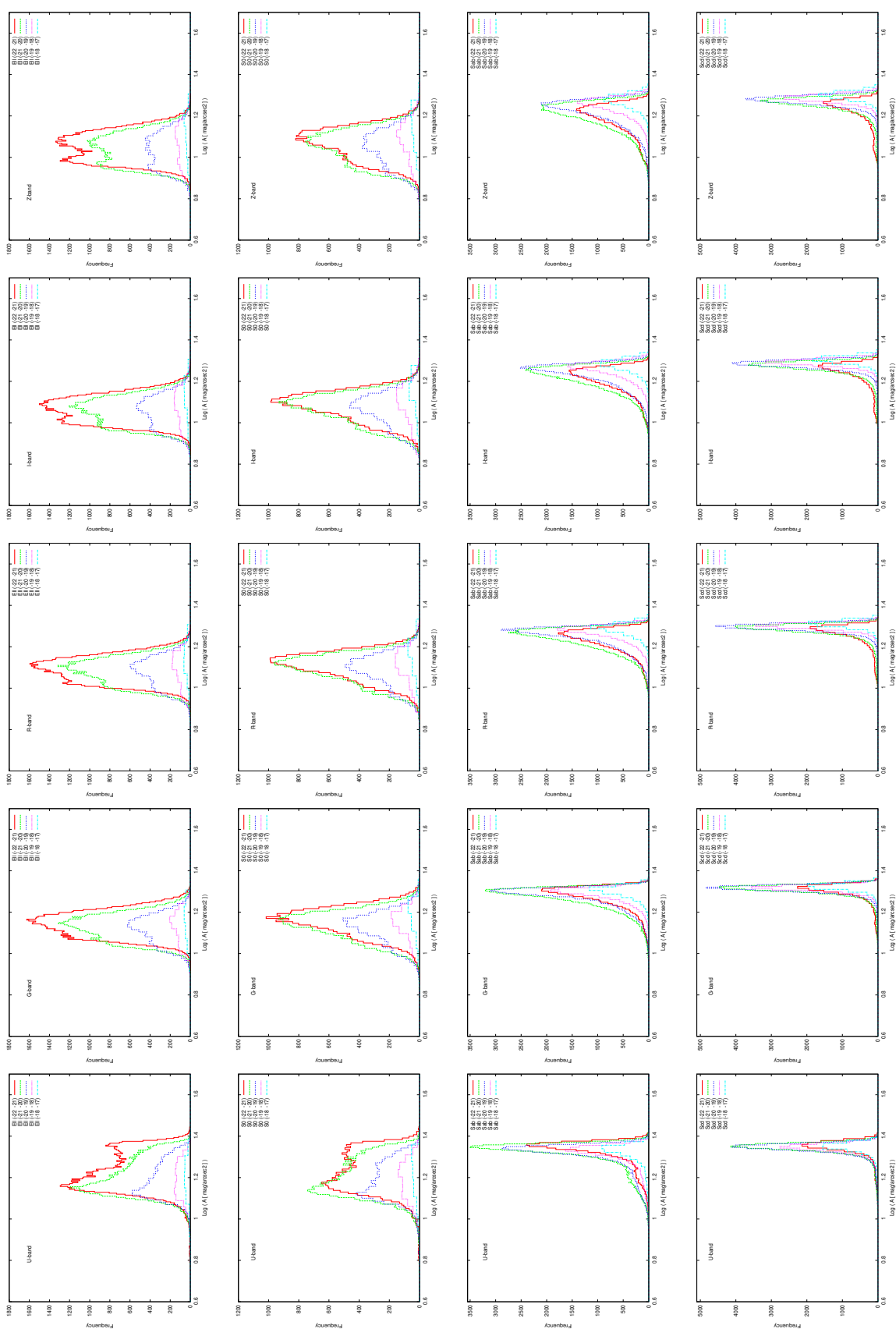


Figure 28: Sérsic’s parameter A [$\text{mag}/\text{arcsec}^2$] histograms per Petrosian bands u, g, r, i, z , per type galaxy Ell, SO, Sab, Scd and per magnitude bin.

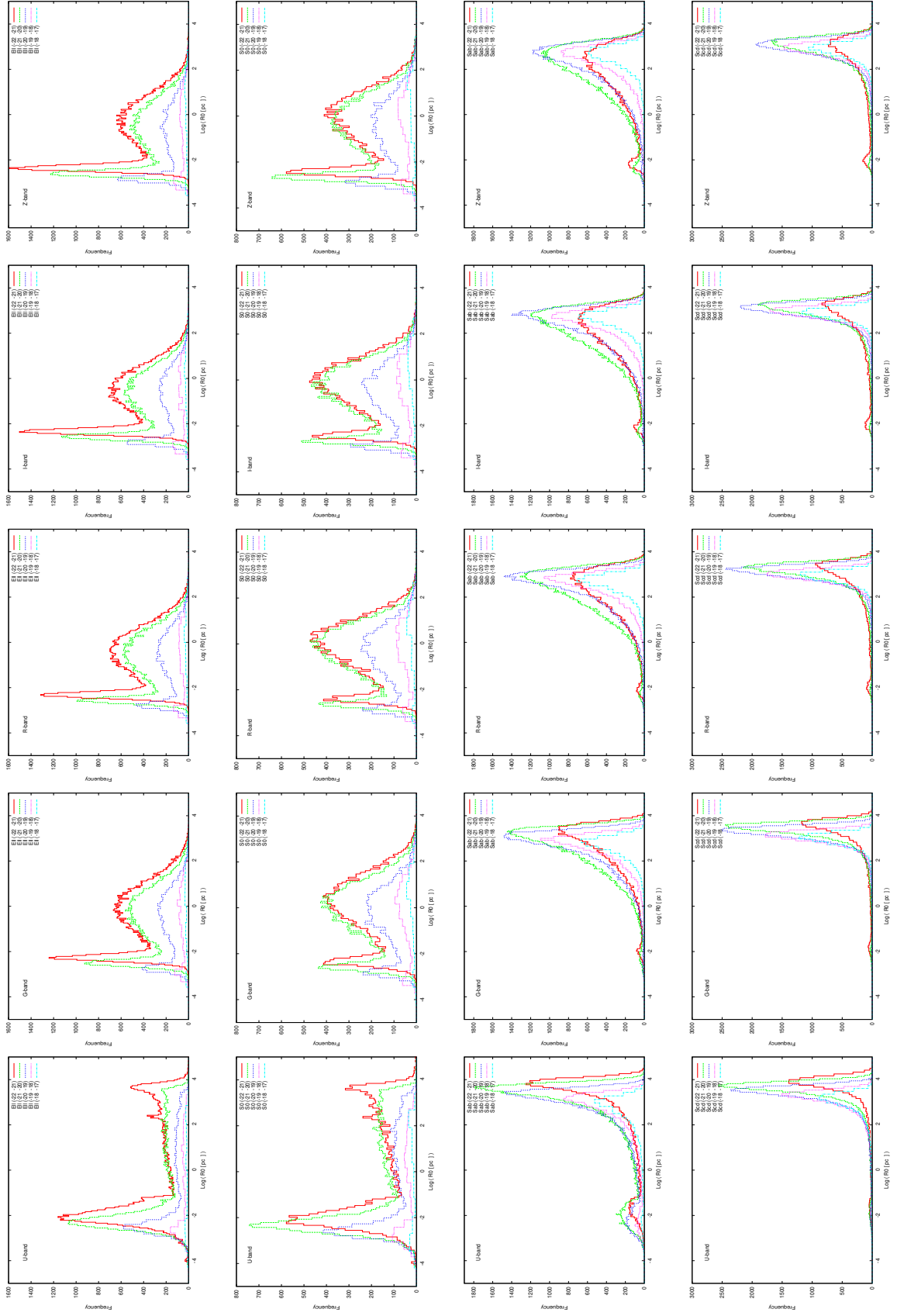


Figure 29: Sérsic's parameter R_0 [parsecs] histograms per Petrosian bands u, g, r, i, z , per type galaxy Ell, S_0, Sab, Scd and per magnitude bin.

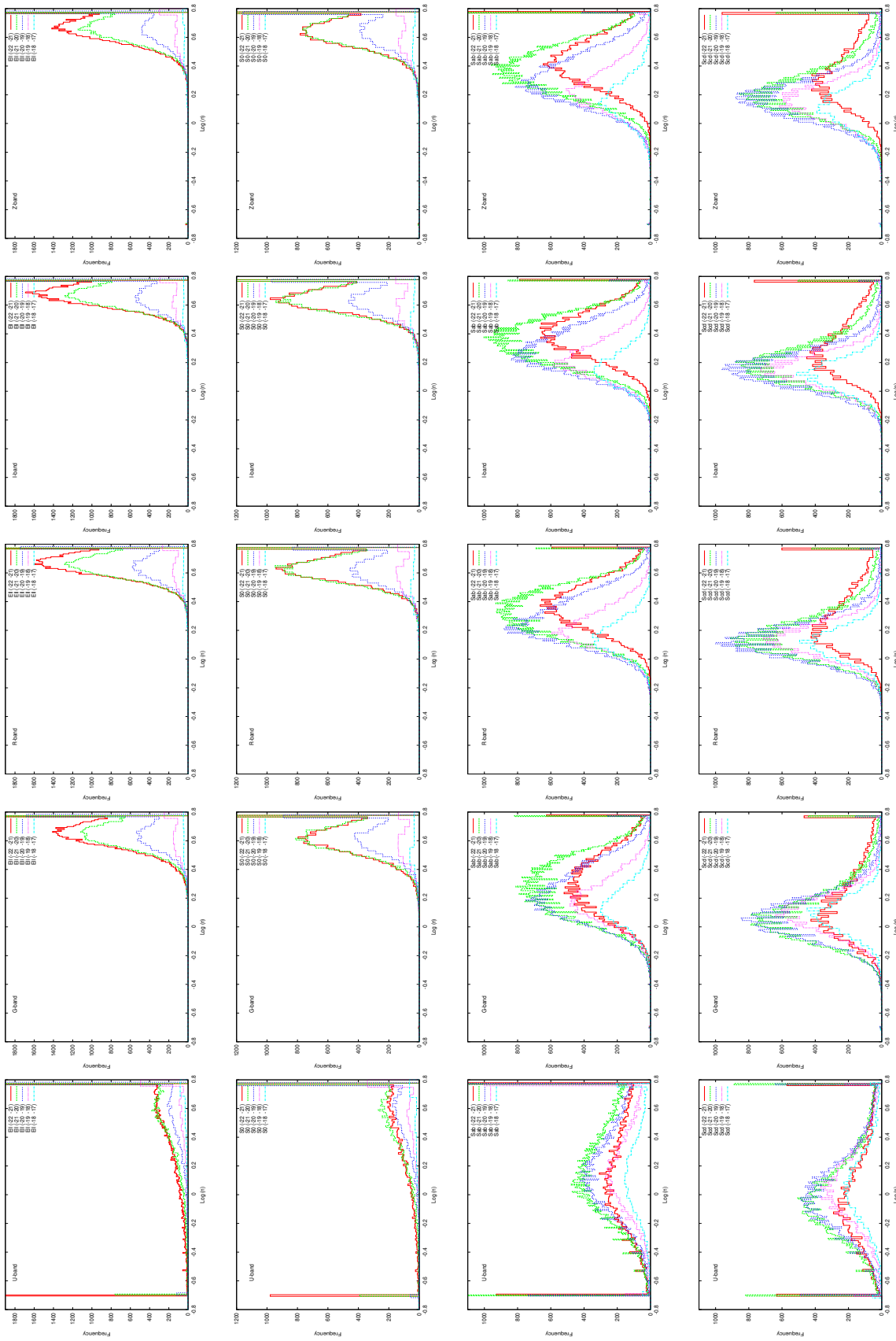


Figure 30: Sérsic's parameter n histograms per Petrosian bands u, g, r, i, z , per type galaxy $Ell, S0, Sab, Scd$ and per magnitude bin.

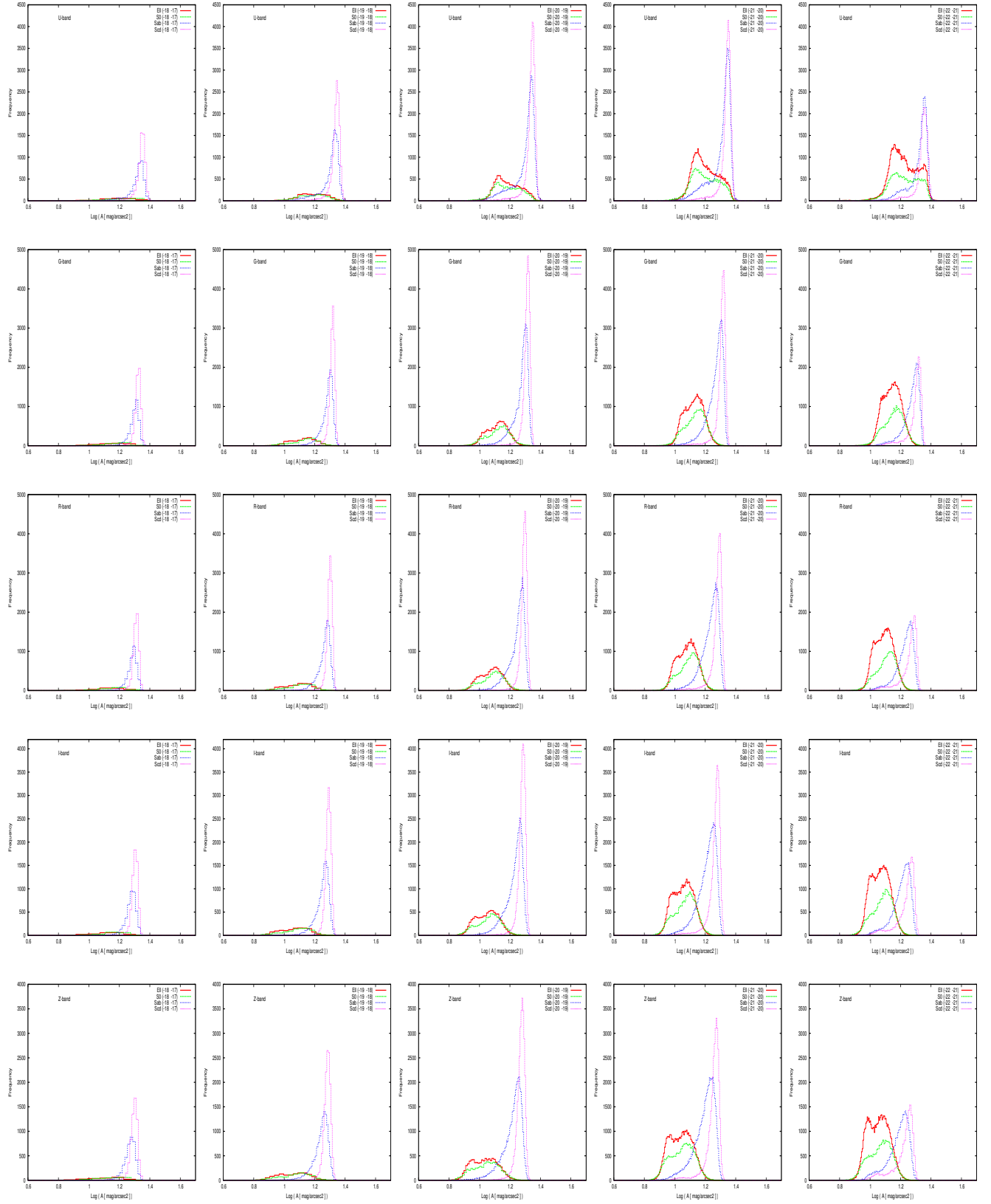


Figure 31: Sérsic's parameter A [mag/arcsec²] histograms per Petrosian bands u, g, r, i, z , per magnitude bin between -17 and -22 for the four types Ell , SO , Sab , Scd .

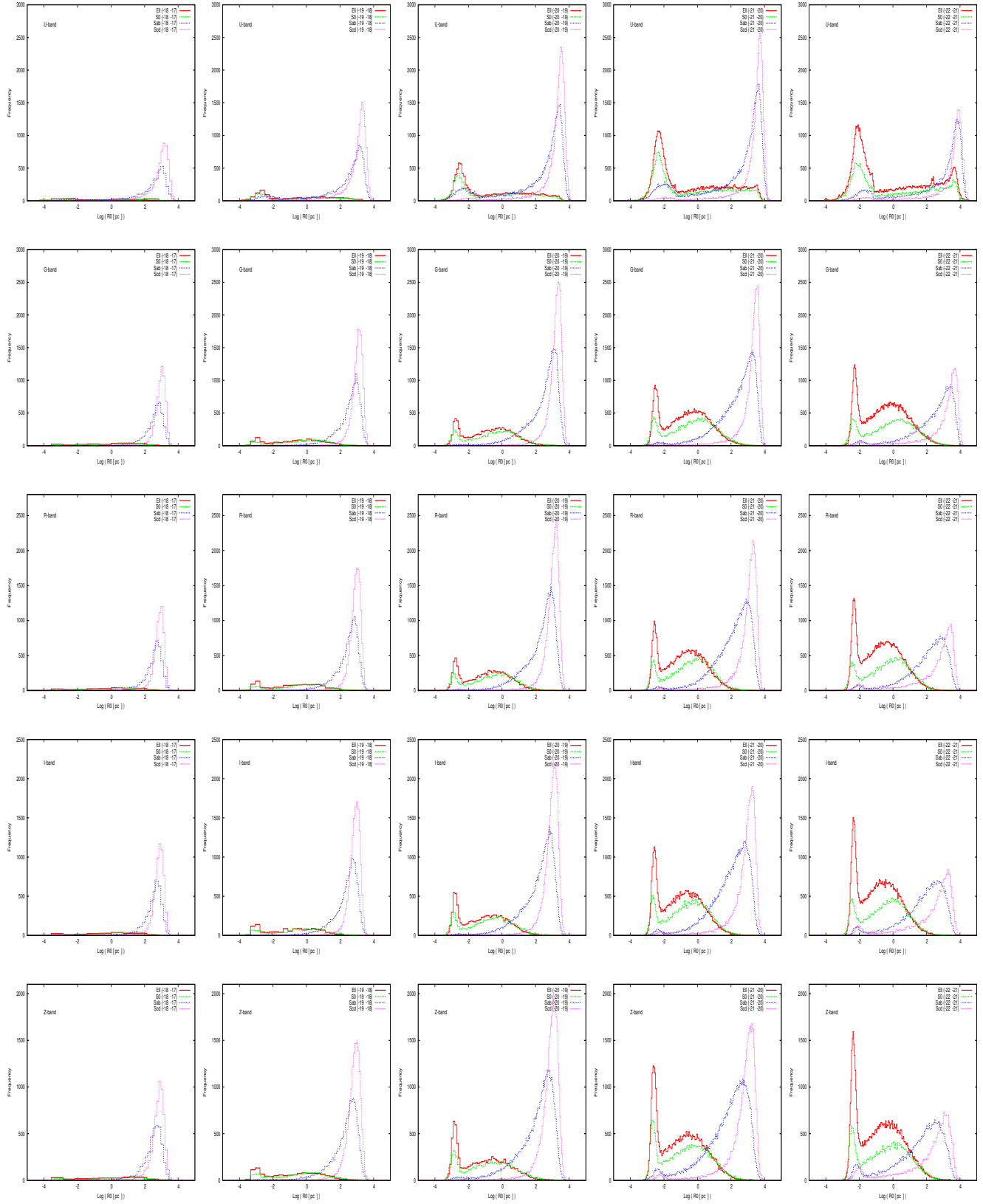


Figure 32: Sérsic's parameter R_0 [parsecs] histograms per Petrosian bands u, g, r, i, z , per magnitude bin between -17 and -22 for the four types Ell , S_0 , Sab , Scd .

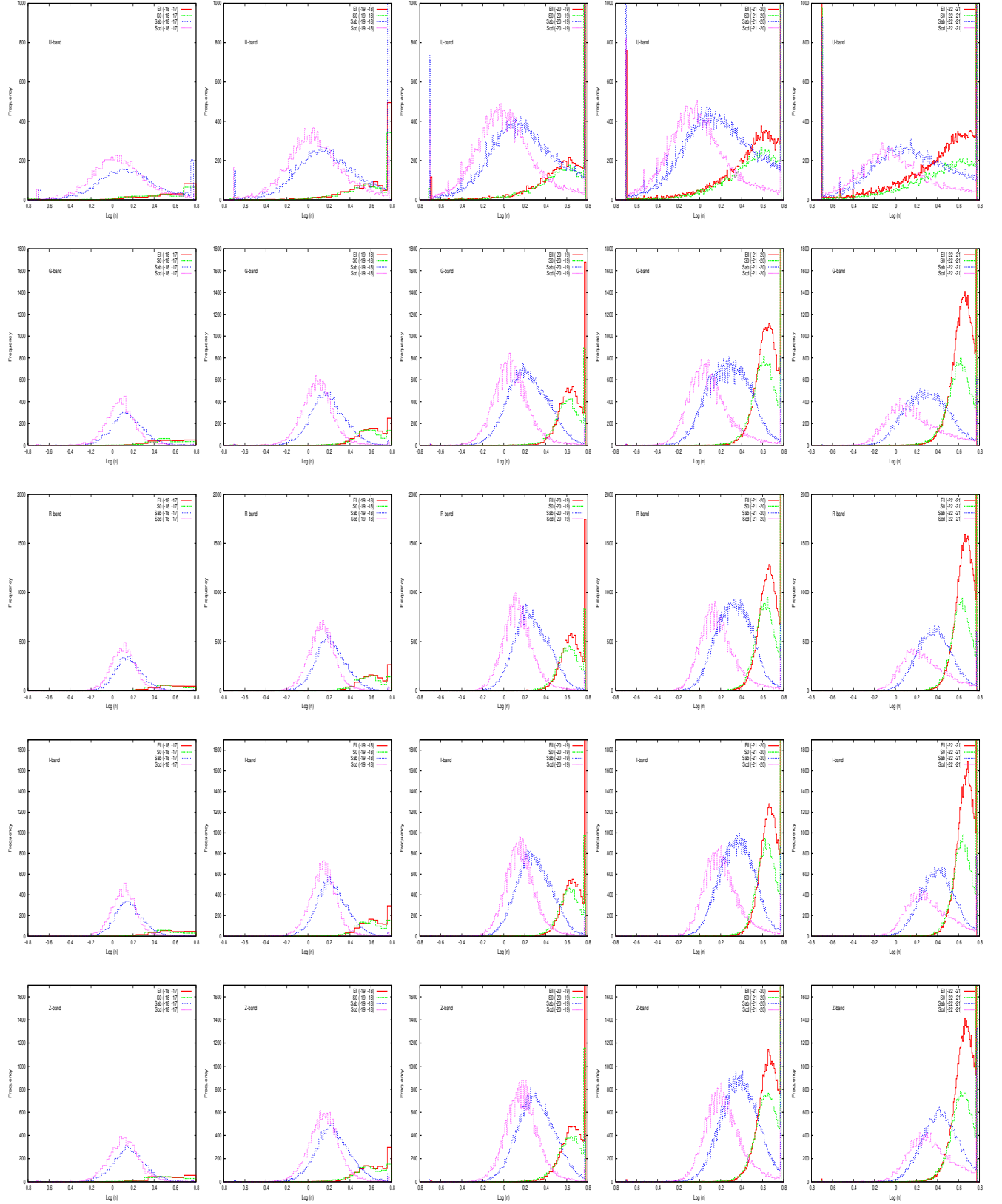


Figure 33: Sérsic's parameter n histograms per Petrosian bands u, g, r, i, z , per magnitude bin between -17 and -22 for the four types Ell , SO , Sab , Scd .

GALACTIC DISKS MODEL

3.1 INTRODUCTION

Observational data is really important when using models which involve parameters that one only could get through observation. In this work, the parameters obtained through the fitted Sérsic profile to each object should be related with the properties of the galactic disks model provided by (Mo, Mao & White) [22]. Then, through the observational parameters such as the surface brightness, Sérsic's index and scale length we are able to find, like in an inverse problem, properties of the dark matter halo where a certain galaxy is embedded in. The main problem of this chapter is to try to show up a way to infer the properties of dark matter halos, through the observations.

The different data used to achieve our goals are shown in this chapter. All the procedures to clean up the main sample are explained, and a brief sketch about the galactic disks model, and its importance to our work is also shown. Finally, the connection with the observation and the final results obtained through the implementation of the model with observations is explained.

3.2 DATA

First of all, (Mo, Mao & White) [22] model has been developed for galactic disks, so we are going to use it to study only our sample of disk galaxies. Thus, as it has been shown in [Chapter 2](#), the new subsample that is going to be used to study the connection of its observational properties with those of the dark matter halo will be the *Sab* and *Scd*, while *Ell* or *S0* will be avoided because they belong to the spheroidal ones. Thereby, our new sample consists of 257.637 objects which are splitted into 151.031 spiral galaxies of type *Sab* and 106.606 galaxies of type *Scd*.

Once we know exactly the subsample to use, some criteria should be applied to choose the strictly necessary parameters associated to the Sérsic's profile to work with. Therefore, to each kind of galaxy only the data in the petrosian band r was chosen, simply, because in this band the entire parameters are well behaved and the noise is the lowest. Thus, the surface brightness, scale length and Sérsic's index n were extracted in the r band. It was also extracted the stellar mass component associated to each galaxy provided by [11] which is going to be of great importance when trying to connect the surface brightness with the mass through a Mass-Luminosity relation.

All the data, was once again checked-up to avoid misclassification when applying the model. Several plots of the different properties extracted were looked to be in an appropriated range and units as shown in [29], for the two subsamples.

Next big step is to try to connect photometric properties with the dark matter halo parameters, such as the spin, concentration and virial mass. Before doing this, one should take care about the model to be used. In this case, as mentioned through this chapter, the (Mo, Mao & White) model [22] is the only one which is going to be used. Thus, in the next section a sketch of the more important components of the model and the connection with our work will be explained.

3.3 GALACTIC DISKS MODEL

In standard hierarchical model dissipationless dark matter aggregates into larger and larger clumps and the gas associated with such dark matter halos cools and condenses within them to form the galaxies we see today [22]. Thus, the cooled-off gas collected at the centre of the dark matter halo forms a self-gravitating unit, which we call galaxy, which can form stars, heating and enriching the rest of the gas. The halos can merge and interact forming groups and clusters.

As shown by [22], simulations have failed to reproduce viable models for observed spirals producing small disks. Thereby, (Mo, Mao & White) addressed the formation of disks in hierarchical cosmogonies through four key assumptions: (1) the mass of a disk is some fraction of the mass of the dark matter halo in which it is embedded; (2) Same assumption for the angular momentum, thus, the angular momentum of the disk is a fixed fraction of the dark matter angular momentum; (3) the disk has an exponential surface density profile and it is a centrifugally supported structure and (4) only those systems which are dynamically stable are the ones to be considered real galaxy disks. On the other hand, they obtained the abundance of halos in an specific cosmogony from the Press-Schechter formalism, the dark matter density profiles modeled through a NFW (Navarro, Frenk, White) profile and the angular momentum distributions through a near-universal form found in N-body simulations.

The relevant cosmological parameters are the Hubble constant $H_0 = 100h \text{ km s}^{-1} \text{ Mpc}^{-1}$ where $h = 0.7$, the total matter density $\Omega_M = 0.3$, the cosmological constant $\Omega_\Lambda = 0.7$, all of them components of the well known Λ CDM model. So important, because it is the comogony that we have been using throughout in this work. In the model, the spheres are treated as singular isothermal spheres neglecting the gravitational effects of the disks but lately a more realistic model including NFW profile and gravitational effects on the disks are performed.

3.4 MO, MAO & WHITE MODEL

In this section the galactic disks formation model will be explained going from the simplest model wich is the singular isothermal sphere to a more realistic one.

3.4.1 Model scheme

The simplest scenario is that the dark matter halo is a singular isothermal sphere where the density profile is just:

$$\rho(r) = \frac{V_c^2}{4\pi G r^2} \quad (3.1)$$

where the circular velocity V_c is independent of radius. We can define, based on the spherical collapse model the virial radius which is a limiting radius of the dark matter halo where the median mass density is proportional to critical density ρ_{crit} . Thus, the virial radius and the virial velocity are defined as,

$$R_{vir}^3 = \frac{3M_{vir}}{4\pi\Delta_{vir}\rho_{crit}(z)} \quad ; \quad V_{vir}^2 = \frac{GM_{vir}}{R_{vir}} \quad (3.2)$$

where the critical density is guven by $\rho_{crit} = 3H^2(z)/8\pi G$. All these quantities depends on the redshift because the Hubble constant at redshift z is given by,

$$H(z) = H_0[\Omega_{\Lambda,0} + (1 - \Omega_{\Lambda,0} - \Omega_0)(1+z)^2 + \Omega_0(1+z)^3]^{1/2} \quad (3.3)$$

this last equation will be computed for the present time which is $z = 0$ because our largest redshift value is $z = 0.25$ and we will use the cosmogony explained before .

Now taking into account, the conditions for the disk, the exponential surface density profile is,

$$\Sigma(R) = \Sigma_0 \exp(-R/R_d) \quad (3.4)$$

where the scale length R_d and the surface density Σ_0 are related to the disk mass through,

$$M_d = 2\pi\Sigma_0 R_d \quad (3.5)$$

Neglecting the gravitational effect of the disk in this case, the angular momentum of the disk is,

$$J_d = 2\pi \int V_c \Sigma(R) R^2 dR = 4\pi\Sigma_0 V_c R_d^2 = 2M_d R_d V_c \quad (3.6)$$

which is really important because it helps out to define the angular momentum of the disk as a fraction of the angular momentum of the halo and the spin parameter that characterizes the rotation of the dark matte halo, through,

$$J_d = j_d J \quad ; \quad \lambda = J|E|^{1/2} G^{-1} M^{-5/2} \quad (3.7)$$

where E is the total energy of the halo. For a truncated singular isothermal sphere it is easily obtained from the virial theorem by assuming particles to be on circular orbits [22]. Using this, and Equation 3.6 and Equation 3.7, one gets,

$$R_d = \frac{\lambda G M^{3/2}}{2V_c |E|^{1/2}} \left(\frac{j_d}{m_d} \right) \quad ; \quad E = -\frac{GM^2}{2R_{vir}} \quad (3.8)$$

Finally, using Equation 3.8, Equation 3.2 and Equation 3.5, one gets

$$R_d = \frac{1}{\sqrt{2}} \left(\frac{j_d}{m_d} \right) \lambda R_{vir} \quad (3.9)$$

and

$$\Sigma_0 = \frac{m_d M_{vir}}{2\pi R_d^2} \quad (3.10)$$

3.4.2 NFW model

It is evident from Equation 3.9 and Equation 3.10 that the properties of the galaxy depend directly on the intrinsic properties of the dark matter halo. If we concentrate in the case where the specific angular momentum of the material which forms the disk is the same as that of the halo, then we can assume that the relation between the fraction of angular momentum and mass is $j_d/m_d = 1$. It has been a standard assumption in modelling disk formation, but it is unclear if it is appropriate [22].

Now, using a NFW profile,

$$\rho(r) = \rho_{crit} \frac{\delta_0}{(r/r_s)(1 + r/r_s)^2} \quad (3.11)$$

thus, the mass within some radius r is then,

$$M(r) = 4\pi\rho_{crit}\delta_0 r_s^3 \left[\frac{1}{1+cx} - 1 + \ln(1+cx) \right] \quad ; \quad x \equiv r/R_{vir} \quad c \equiv R_{vir}/r_s \quad (3.12)$$

c is the halo concentration parameter that will be useful for us to compute the virial mass of the dark matter halo. The energy following what has been said above takes the form,

$$E = -\frac{GM^2}{2R_{vir}} f_c \quad (3.13)$$

where the energy is the same of the isothermal sphere but with a factor that depends on the concentration parameter f_c which comes from the change in total energy resulting from the different density profile,

$$f_c = \frac{c}{2} \frac{1 - 1/(1+c^2) - 2\ln(1+c)/(1+c)}{[c/(1+c) - \ln(1+c)]^2} \approx \frac{2}{3} + \left(\frac{c}{21.5} \right)^{0.7} \quad (3.14)$$

Assuming that the halo responds adiabatically to the slow assembly of the disk, and that it remains spherical as it contracts, and substituing Equation 3.11 into Equation 3.7 they obtained

$$R_d = \frac{1}{\sqrt{2}} \left(\frac{j_d}{m_d} \right) \lambda R_{vir} f_c^{-1/2} f_R(\lambda, c, m_d, j_d) \quad (3.15)$$

where f_R is due both to the different density profile and to the gravitational effects of the disk and it is given by,

$$f_R(\lambda, c, m_d, j_d) \approx \left(\frac{\lambda'}{0.1} \right)^{-0.06+2.71m_d+0.0047/\lambda'} (1-3m_d+5.2m_d^2)(1-0.019c+0.00025c^2+0.52/c) \quad (3.16)$$

where $\lambda' \equiv (j_d/m_d)\lambda$. Taking all this, we can finally obtain the form of the scale length of the galaxy and the surface density profile in terms of a more realistic model. Thus, the scale length in Kpc is obtained by

$$R_d \approx (3.241 \times 10^{-17}) \frac{1}{\sqrt{2}} \lambda \left(\frac{2M_{vir}G}{\Delta_{vir}H^2(z)} \right)^{1/3} f_c^{-1/2} f_R(\lambda, c, m_d, j_d) \left(\frac{j_d}{m_d} \right) \quad Kpc \quad (3.17)$$

Moreover using Equation 3.10 the surface density profile is given by

$$\Sigma_0 = (260.4) \left(\frac{0.05}{\lambda} \right)^2 \left(\frac{V_{vir}}{250km s^{-1}} \right) \left(\frac{H(z)}{H_0} \right) f_c f_R^{-2} \left(\frac{m_d}{j_d} \right)^2 \quad M_\odot pc^{-2} \quad (3.18)$$

The most important results which are of our interest in this work are Equation 3.17 and Equation 3.18 because they gives us a tool to know the scale length and the surface density profile of a galaxy through properties that can be measured through observations as the virial velocity, virial mass and Hubble constant and also through properties of the dark matter halo that can be model as the spin and concentration.

Following the prescription, one should know how to find the spin and concentration of a given dark matter halo before using the model to compare the data. Thereby, in the next subsection we proceed with a sketch of the calculation of the spin, concentration and virial mass of the dark matter halo to later on match it with the (Mo, Mao & White) model.

3.4.3 Spin, Concentration, Virial Mass

In this moment, we are going to concentrate in the dark matter halo parameters as spin, concentration and virial mass. So the big deal now is that we need to create a big sample of model galaxies according to theory to obtain reliable data to compute the scale length and the surface density profile.

First of all, let's observe that the concentration and the spin parameter are independent. However, the concentration is directly correlated with the mass of the dark matter halo, while the spin is almost independent of the mass, it shows up a weak dependence on the mass when the redshift z increases as shown by [25]. This guarantees us how to deal with the calculations of these different quantities.

To begin, in first place, we address the computation of the spin parameter. Based on [25] work, we know that the spin parameter distribution at all redshifts is well fitted by a lognormal distribution:

$$P(\lambda') = \frac{1}{\lambda' \sqrt{2\pi}\sigma} \exp \left[-\frac{\ln^2(\lambda'/\lambda'_0)}{2\sigma^2} \right] \quad (3.19)$$

with $\sigma = 0.57$ and $\lambda'_0 = 0.031$. According to this distribution and using the Acceptance-Rejection method we reproduced a sample of 500.000 spins. At the end we can check-up if the data reproduce through the model is well done by re-building the histogram of the distribution and fitting the original distribution to find if the values of σ and λ'_0 are in the expected range. If the method is well enough to reproduce the values, one expects that this parameters do not change too much. Fitting Equation 3.19 to the new sample of spins as shown in Figure 34 we were able to

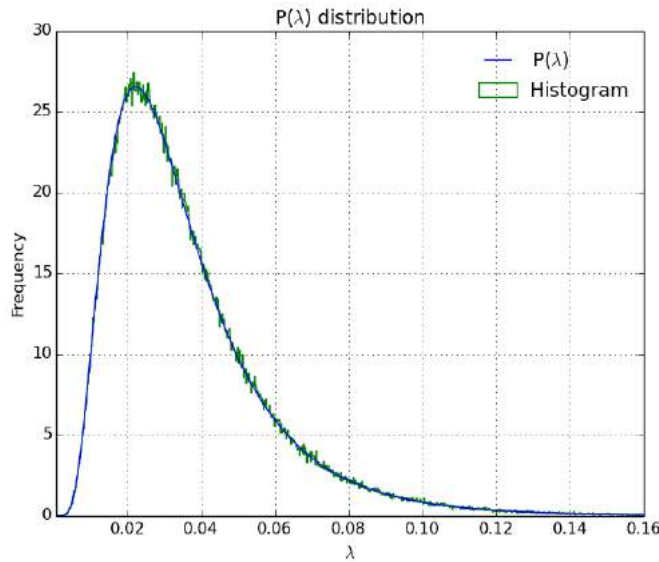


Figure 34: Spin distribution obtained through the acceptance-rejection method. The y-axis corresponds to the frequency while the x-axis are the values of the spin parameter. The green lines represent the histogram of a sample of 500.000 spins and the blue one is the fitted probability distribution that might follow those spins. The value of $\sigma = 0.0309$ and $\lambda'_0 = 0.572$ really close as those in Equation 3.19.

extract the values that best fit our histogram obtaining $\sigma = 0.0309$ and $\lambda'_0 = 0.572$ which confirms

that the produced sample follows a lognormal distribution. These spins are then, the ones we are going to use to associate them to a given model galaxy.

Using a tabulated form of Warren et. al,2006 mass function we were able to reproduce 500.000 virial masses which build our model sample. The mass covers a wide range but we will split it into $[10^{10}, 10^{13}]M_{\odot}$ because are the ones where spiral galaxies are expected to be hosted in. We performed a linear interpolation to obtain the total of masses we wanted to all the original range of masses. After this, the Acceptance-Rejection method was again employed to the sample of 500.000 dark matter halo masses but only between our range $[10^{10}, 10^{13}]M_{\odot}$ and those were the ones extracted. In Figure 35 the blue line represents the data taken as Warren et. al,2006 while the green one is the linear interpolation. It is observed that the interpolation fits well the data so we can use it to reproduce the mass distribution. Thus, in Figure 36 we plotted the mass distribution for a sample of 500.000 masses between our mass range with its respective frequency in the y-axis. It is important to observe that the masses follow a Press-Schechter form as expected. Finally,

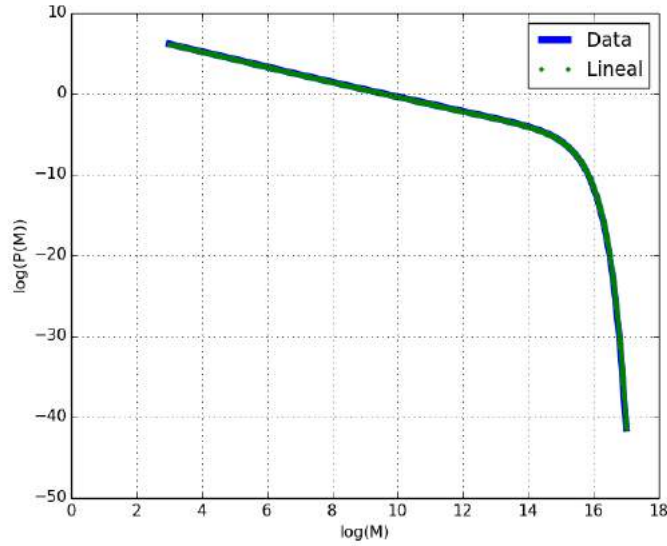


Figure 35: Mass function distribution derived from a mass function of dark matter halos provided by Warren et. al,2006. The blue line are the data while the green one represents the linear interpolation to obtain enough data to perform an Acceptance-Rejection method.

and once the spin parameter and the virial mass of the dark matter halo has been computed we proceed to calculate the concentration. Because of its dependence on mass it is important to note that for a given halo mass there is a given concentration while the spin could be whichever. The concentration following [25] is given by,

$$\begin{aligned} \log(c) &= a(z) \log(M_{vir}/[M_{\odot}]) + b(z) \\ a(z) &= wz - m \\ b(z) &= \frac{\alpha}{(z + \gamma)} + \frac{\beta}{(z + \gamma)^2} \end{aligned} \tag{3.20}$$

where the parameters have been set equal to $w = 0.029$, $m = 0.097$, $\alpha = -110.001$, $\beta = 2469.720$ and $\gamma = 16.885$. there is a dependence with redshift in all the last equations, but we have computed the concentration at $z = 0$, and assumed that z dependence does not affect too much our results.

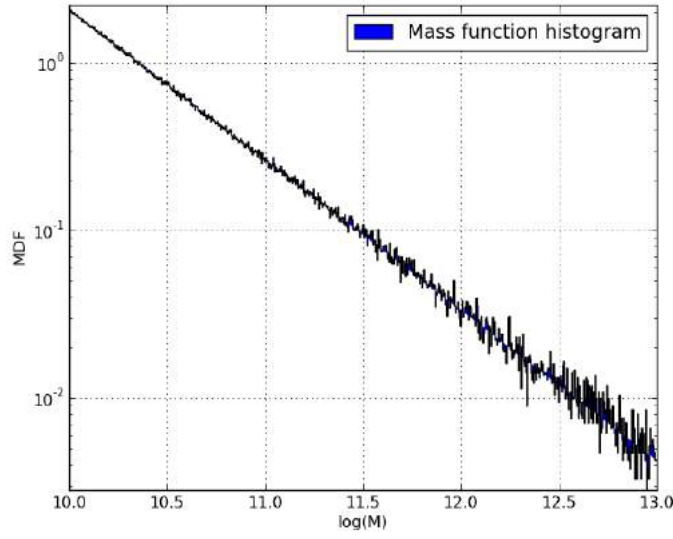


Figure 36: The x-axis is the logarithm of mass in solar masses while y-axis is the frequency.

However, it is not so realistic to find a concentration following the median values as those produced by Equation 3.20, thus, given a mass M_{vir} the median concentration was found and using it a new concentration was calculated using a random normal distribution around that median. The new concentration was then obtained just simply using a $\sigma = 0.3$ scatter in the found concentration through the normal distribution [21]. In Figure 37 we have the concentration of

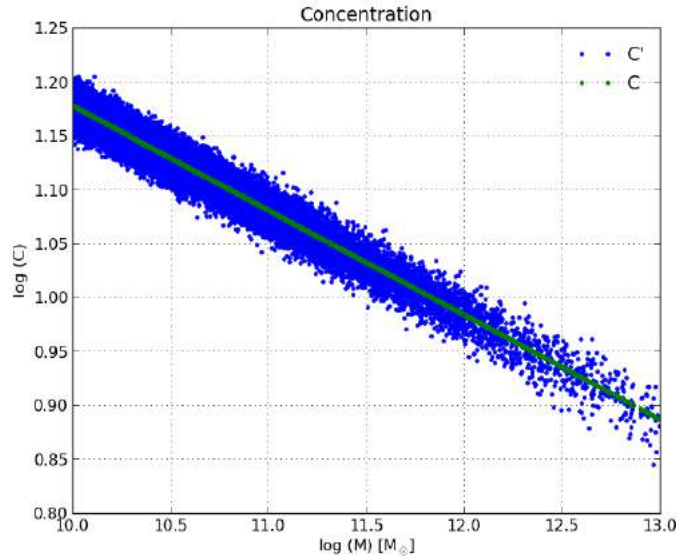


Figure 37: Concentration distribution against the virial mass. In the x-axis there is the logarithm of the virial mass of a dark matter halo while in the y-axis is the concentration to that particular halo. The blue dots represent the concentrations with an scatter of $\sigma = 0.3$ applied to Equation 3.20 which are the median values of the concentration and corresponds to the green line.

a collection of dark matter halos with masses in the range $[10^{10}, 10^{13}]M_{\odot}$. The blue dots are the

concentrations computed with an scatter while the green line is the median values of those blue points obtained applying Equation 3.20.

Finally, our result is a set of 500.000 model dark matter halos with a given spin, concentration and virial mass. According to what has been said through this chapter, this parameters which characterizes the dark matter halo will be the straight connection between the observational data and the model ones. Using this into the (Mo, Mao & White) model will helps us to find out the scale length and the surface density profile of a given galaxy to later on compare it with those extracted from the VAGC.

3.5 CONNECTION BETWEEN OBSERVATION AND MODEL

As it has been said scale length and surface density profile can be computed once the spin, concentration and virial mass of the dark matter halo through Equation 3.17 and Equation 3.18. However in Equation 3.18 depends on virial velocity which can be obtained in terms of the virial radius and the virial mass as shown in Equation 3.2. Using the sample of 500.000 model dark matter halos we proceed to calculate a sample of R_d and Σ_0 , given by the concentration, spin and virial mass which are well known yet.

To verify our results, we plotted a scale length's histogram to assure that when computing all the quantities the final result is in agreement with expectations. In Figure 38 we can observe the scale length distribution once has been computed using the (Mo, Mao & White) model and all the parameters of the dark matter halo explained above. In the y -axis there is the frequency while in the x -axis the scale length in kpc . This plot shows a log-normal like distribution as was expected from observational distributions shown in Figure 29 from Chapter 2 and we can see how the scale length frequency decreases towards large values while values below 2 kpc are more likely as observations show. Same procedure was addressed to obtain the surface density profile

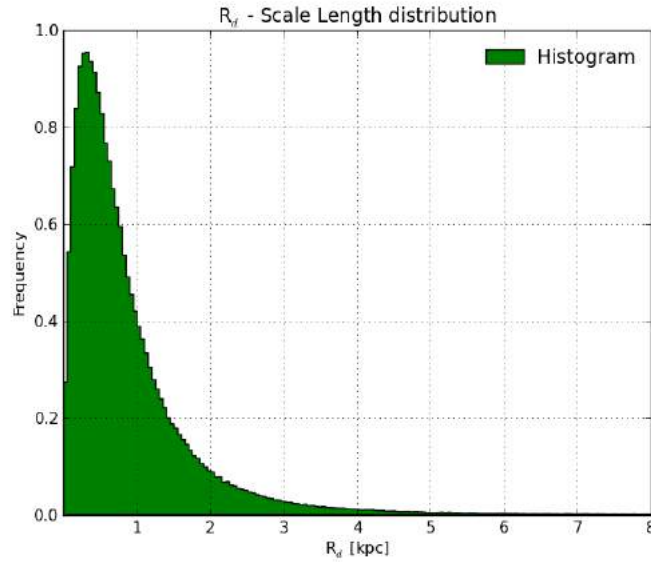


Figure 38: Scale length distribution. In the x-axis is represented the scale length is Kpc while in the y-axis is the frequency. It shows the distribution of the computed scale lengths for a total sample of 500.000 objects through the model properties of the dark matte rhalo and the (Mo, Mao & White) disks model [22].

of the galaxies. In Figure 39 one can observe the surface density profile histogram plotted with data from Equation 3.18. Once again as in the case of the scale length in the y -axis there is the frequency while in the x -axis is the surface central brightness. We can see that central surface brightness follows an expected distribution where the most likely values are around $2.5 M_{\odot} pc^{-2}$ as shown by [20]. The plot was build up to verify that this quantity was well computed after using the model data of the dark matter halos and the disks model. The scale length and the surface

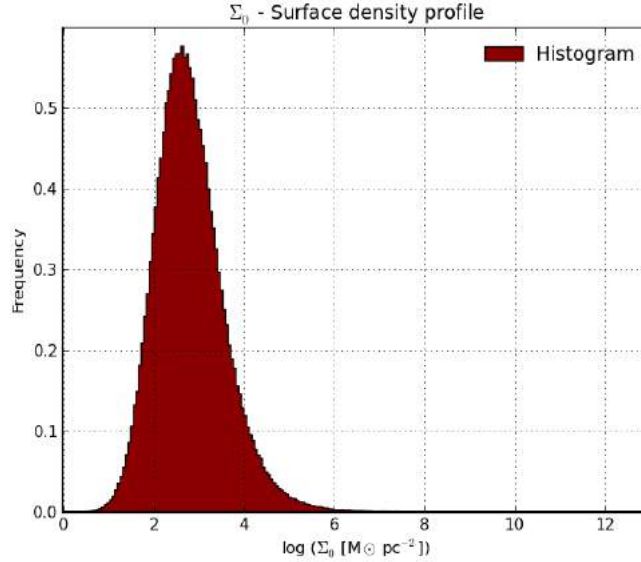


Figure 39: Surface density profile. In the x-axis is represented the surface density profile in $M_{\odot} pc^{-2}$ and in the y-axis is the frequency. The surface density was computed using the (Mo, Mao & White) model and the dark matter halo properties. There is a total of 500.000 objects with computed surface density.

density profile for 500.000 represents our final model sample. This will be used to compare the model and the observations. A question now is: How to match the VAGC observations with these two quantities?. When we extracted the *Sab* and the *Scd* galaxies, we concentrated in the Sérsic's profile for which one of its parameters is the disk scale length. Thus, we can use this to connect model and observed quantities. The task now is, given an observed galaxy of a certain type, if the measured scale length is in a certain range of the model ones all of them will be candidates and all its dark matter halo model properties will be inherited such as spin, concentration and virial mass. Of course the median value of each set of parameters will characterize the value assigned to a given galaxy. This is why, through comparing observational data with model we are able to infer properties of the dark matter halo where a galaxy is embedded.

Our criteria to match model galaxies with observed data is represented in Figure 40. Imagine that we take an observed galaxy, for this one we will have the three Sérsic's parameter in the r band and the stellar mass. On the other hand, there are 500.000 model galaxies which can be quite similar or not to the observed one. The match between model galaxies and data is achieved through the disk scale length. For an observed galaxy we look for all the model galaxies that satisfy, $R_0 - 0.1R_0 \leq R \leq R_0 + 0.1R_0$. We have set a range of $\pm 0.1R_0$ which we thought was prudent, however this parameter can be changed. Hence, the final result is a set of galaxies for which their median value of the scale length is close to the observed galaxy's scale length and with an specific surface density, spin, concentration and virial mass of the dark matter halo. Basically, this is the

method to find the properties of the dark matter halo connecting the observed properties and the model ones.

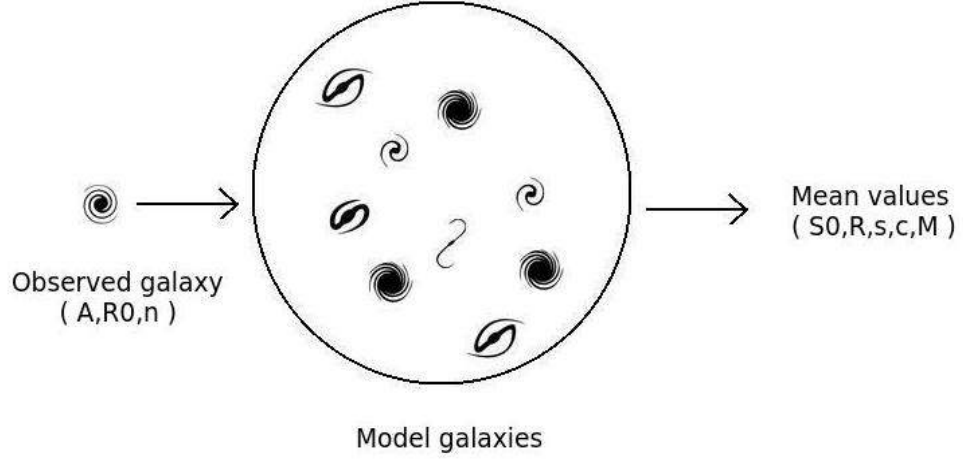


Figure 40: Selection method with scale lengths. In the left-hand there is an observed galaxy with its Sérsic's parameters: scale length, n -index and surface brightness. If in the bunch of galaxies model in the middle there are galaxies which scale lengths belong to a certain range that we defined as $\pm 0.1R_0$, then, those galaxies are extracted and the median values of those galaxies corresponds to the values of scale length, surface density, spin, concentration and virial mass associated to the observed one.

3.6 COMPARISON

After matching an observed galaxy with a bunch of model galaxies, we proceed to analyze each sample separately (*Sab* and *Scd*). It is important to note first that some of these galaxies were rejected because the observed scale length was too small or too big and no-matches were found. In addition, all of those galaxies with a spin parameter smaller than 0.02 were excluded because the parameter was too small. Hence, a total of 76471 *Sab* galaxies from 151031, and, a total of 90541 *Scd* galaxies from 106606, are our final sample of disk galaxies.

Once the matching has been performed and the total sample was cleaned up, we carried out a check-out of the matched data. We chose (randomly) four objects in the sample *Sab* and four in the sample *Scd* and we analyzed the distribution of their spin, concentration, virial mass and surface density distributions. In [Figure 41](#), [Figure 42](#), [Figure 43](#) and [Figure 44](#) there are the distributions of the concentration, spin, virial mass and surface density for the *Sab* galaxies. Each plot label contains information about the observed scale length and the median model scale length to ensure the good matching. Also, there are values corresponding to median dark matter halo parameters and the surface density. The distributions shown in [Figure 41](#), [Figure 42](#), [Figure 43](#), and [Figure 44](#) follows expectations. Concentrations tend to be large for our disk sample as can be observed in the distributions, while the spin parameter of their dark matter halo tend to be really small. Their dark matter halo virial masses are in the small tail of our sample as expected close to $[10^{10} M_{\odot}]$, because the most massive are the spheroidal types, and surface density tends

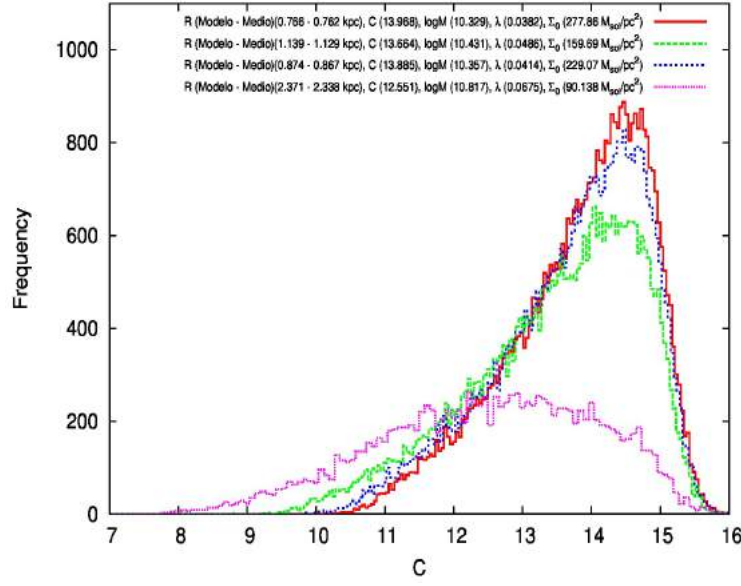


Figure 41: Concentration distribution for four randomly chosen *Sab* matched galaxies. In the x-axis there is the concentration while in the y-axis is the frequency. Each line represents one of the chosen test galaxies. The label shows up the scale length both the observed and model, spin, concentration, virial mass and surface density of the object. Those dark matter attributes are inherited to the object from the scale length matching.

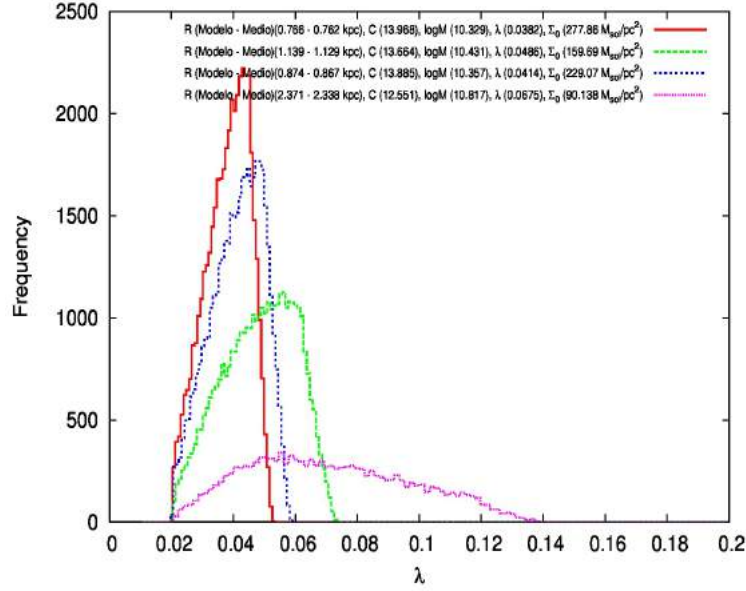


Figure 42: Spin distribution for four randomly chosen *Sab* matched galaxies. In the x-axis there is the spin while in the y-axis is the frequency. Each line represents one of the chosen test galaxies. The label shows up the scale length both the observed and model, spin, concentration, virial mass and surface density of the object. Those dark matter attributes are inherited to the object from the scale length matching.

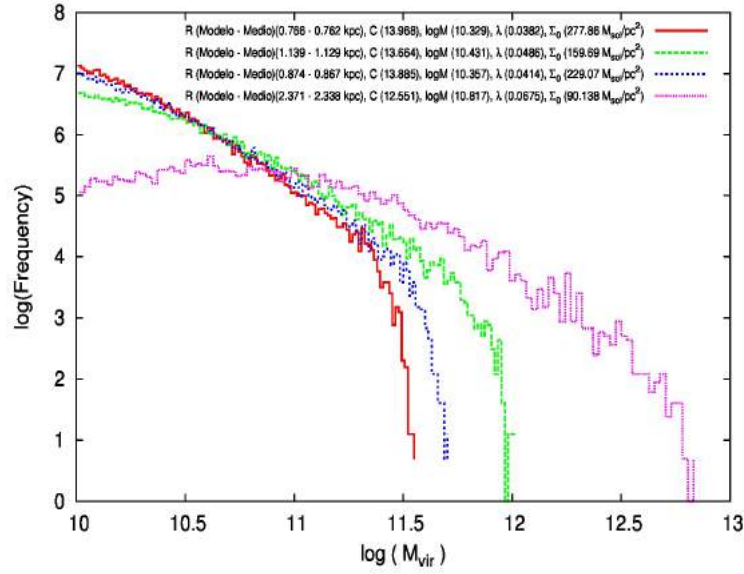


Figure 43: Virial mass distribution for four randomly chosen *Sab* matched galaxies. In the x-axis there is the virial mass in logarithm while in the y-axis is the frequency in logarithm. Each line represents one of the chosen test galaxies. The label shows up the scale length both the observed and model, spin, concentration, virial mass and surface density of the object. Those dark matter attributes are inherited to the object from the scale length matching.

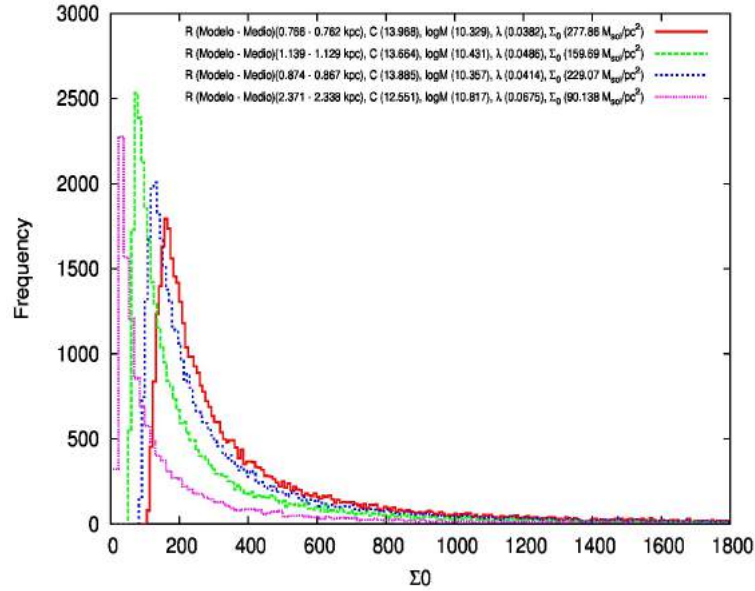


Figure 44: Surface density distribution for four randomly chosen *Sab* matched galaxies. In the x-axis there is the surface density while in the y-axis is the frequency. Each line represents one of the chosen test galaxies. The label shows up the scale length both the observed and model, spin, concentration, virial mass and surface density of the object. Those dark matter attributes are inherited to the object from the scale length matching.

to be close to small values instead of large ones which exposes the disk nature of our sample. Roughly, the expectations about the behavior of these quantities are the expected ones. However, we plotted relations between the concentration, virial mass and spin to check the whole *Sab* sample, and not just for the four galaxies. This can be found in [Figure 45](#). In panel (a) we see the expected dependence of dark matter halo median concentration on the median virial mass, where less massive halos are the most concentrated ones. In panel (b) and (c) we see the median values of spin-concentration and spin-virial mass, however the observed correlations comes from the relation of all these parameters through the scale length equation given by (Mo, Moa & White), which indicates that if we want to build up a galaxy with a given scale length inside a dark matter halo with a given virial mass (i.e concentration), so, the spin parameter must satisfy some value related to the concentration.

In [Figure 45](#) panel (a) those halos less massive are the more concentrated, as expected and in fact are those with a low spin parameter. The dependency of the spin parameter with the mass is introduced by the model equations because one can be obtained in terms of the other but it can not be taken as a fact because as it has been said above these two parameters are independent. The correlations between the dark matter halos can be found in [Figure 50](#).

Same tests were performed to the *Scd* sample. The four chosen galaxies can be found in

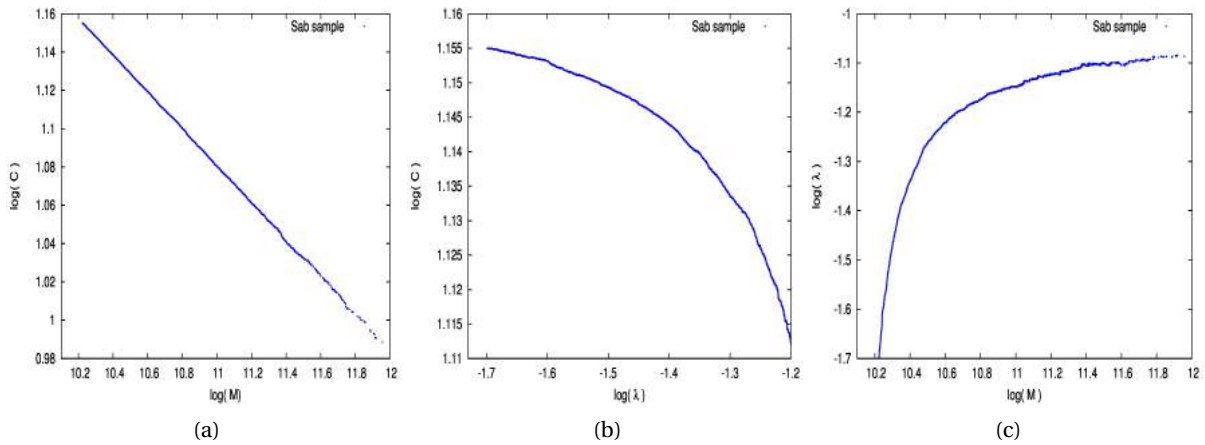


Figure 45: (a) Concentration and mass relation. (b) Concentration and spin relation. (c) Spin and virial mass relation.

[Figure 46](#), [Figure 47](#), [Figure 48](#), [Figure 49](#) and [Figure 50](#). Of course this sample have the same behavior as the one presented for *Sab* sample.

However, concentration, virial mass and spin parameter were not the only parameters used to characterize the sample. We proceed to find relations between all the observational and model parameters. In this case we plot the whole sample of *Sab* and *Scd* galaxies and found the median values which fit the distribution to obtain the trends to perform a better analysis. In [Figure 51](#) we can see in (a) and (b) the behavior of the scale length on virial mass and spin parameter respectively. In panel (a) we see how disk scale length increases with virial mass. In panel (b) disk scale length once more increases for larger values of the spin parameter but smoother than with virial mass. In (c) the mass fraction (M_*/M_{vir}) decreases when virial mass increases but it is not really pronounced. Same analysis was performed for the *Scd* galaxies.

We have to remark here that once the matching has been performed we end up with a final

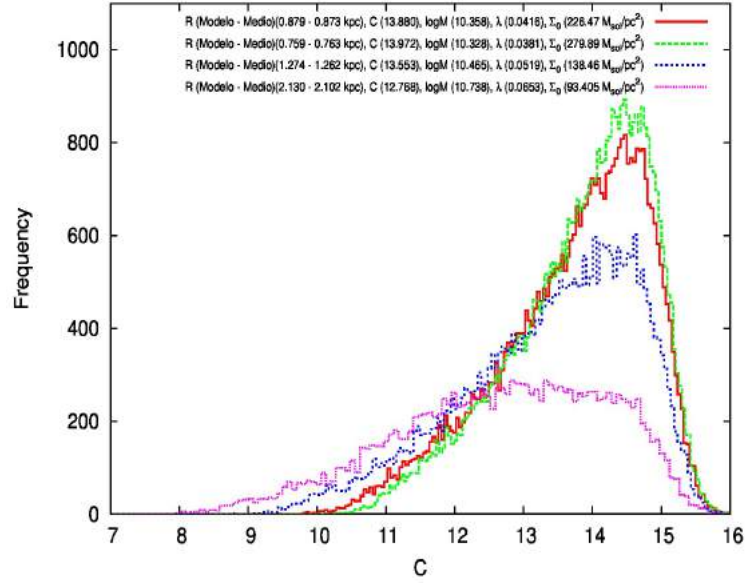


Figure 46: Concentration distribution for four randomly chosen *Scd* matched galaxies. In the x-axis there is the concentration while in the y-axis is the frequency. Each line represents one of the chosen test galaxies. The label shows up the scale length both the observed and model, spin, concentration, virial mass and surface density of the object. Those dark matter attributes are inherited to the object from the scale length matching.

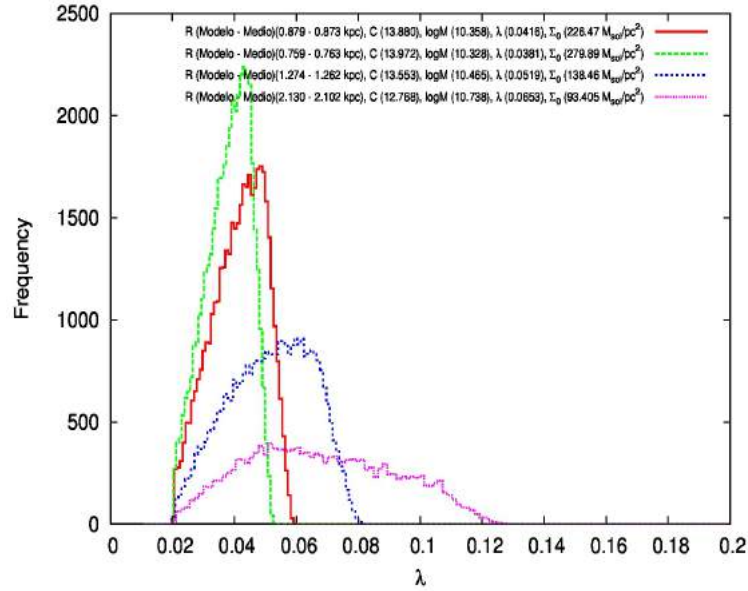


Figure 47: Spin distribution for four randomly chosen *Scd* matched galaxies. In the x-axis there is the spin while in the y-axis is the frequency. Each line represents one of the chosen test galaxies. The label shows up the scale length both the observed and model, spin, concentration, virial mass and surface density of the object. Those dark matter attributes are inherited to the object from the scale length matching.

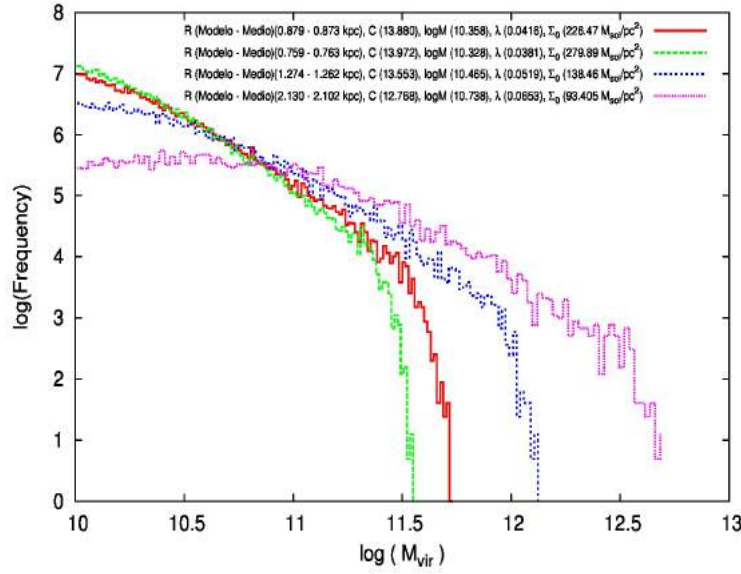


Figure 48: Virial mass distribution for four randomly chosen *Scd* matched galaxies. In the x-axis there is the virial mass in logarithm while in the y-axis is the frequency in logarithm. Each line represents one of the chosen test galaxies. The label shows up the scale length both the observed and model, spin, concentration, virial mass and surface density of the object. Those dark matter attributes are inherited to the object from the scale length matching.

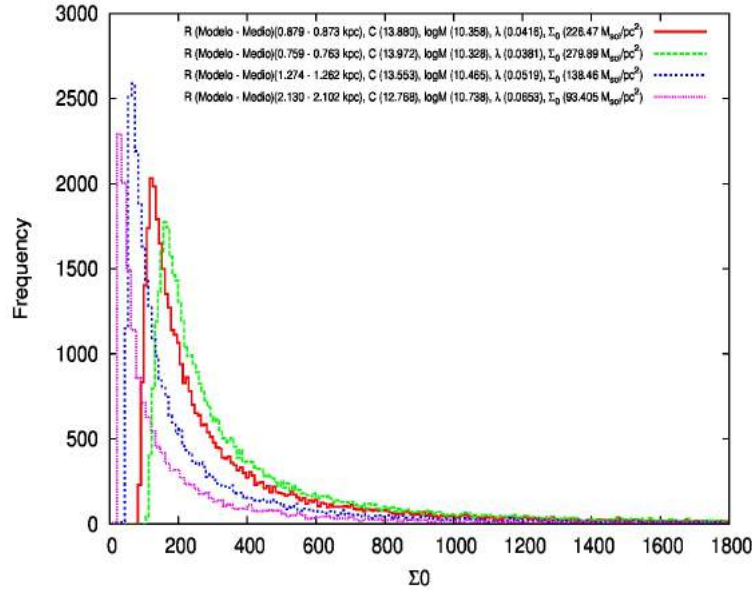


Figure 49: Surface density distribution for four randomly chosen *Scd* matched galaxies. In the x-axis there is the surface density while in the y-axis is the frequency. Each line represents one of the chosen test galaxies. The label shows up the scale length both the observed and model, spin, concentration, virial mass and surface density of the object. Those dark matter attributes are inherited to the object from the scale length matching.

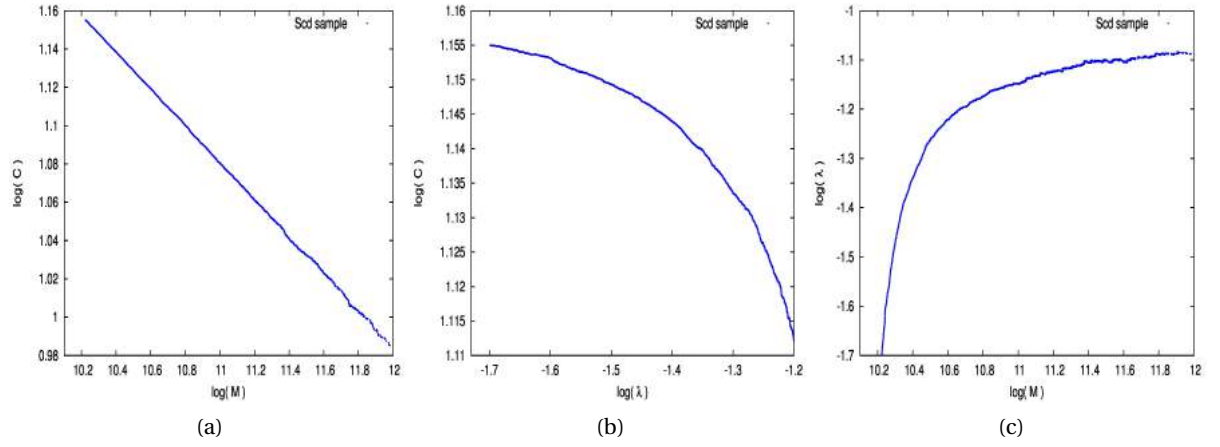


Figure 50: (a) Concentration and mass relation. (b) Concentration and spin relation. (c) Spin and virial mass relation.

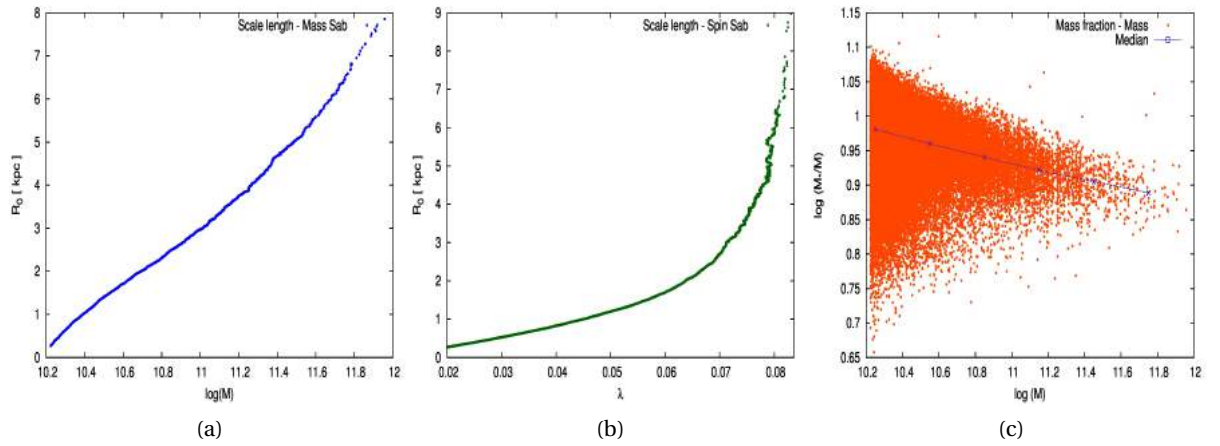


Figure 51: Sab galaxies. (a) Scale length vs virial mass of the dark matter halo. A galaxy's scale length increases with virial mass. Less massive dark matter halos are expected to contain small galaxies compared with bigger ones. (b) Scale length vs spin parameter. Same as the virial mass the spin parameter is expected to increase in this population for bigger scale lengths. (c) represents in the y-axis the mass fraction M_*/M_{vir} against the virial mass in the x-axis. For bigger virial mass the less mass fraction, however it is not so noticeable.

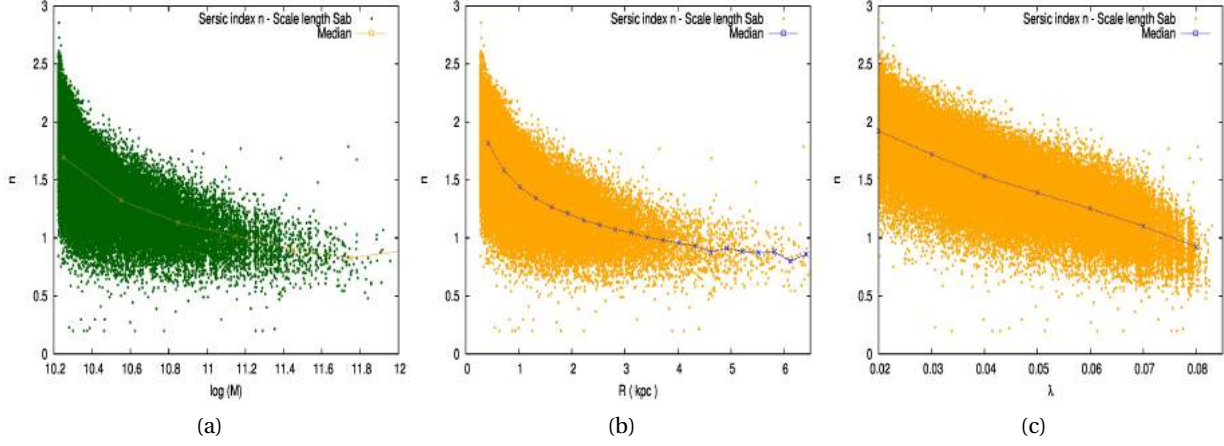


Figure 52: Sab galaxies. (a) Sérsic's index n vs virial mass. As expected lower virial mass, lower Sérsic n index which is interpreted as spiral galaxies which is the sample we have. (b) Sérsic's index n vs scale length. To higher scale length the lower Sérsic's index n . (c) Sérsic's index n vs spin parameter. Higher spin parameter the lower Sérsic's index.

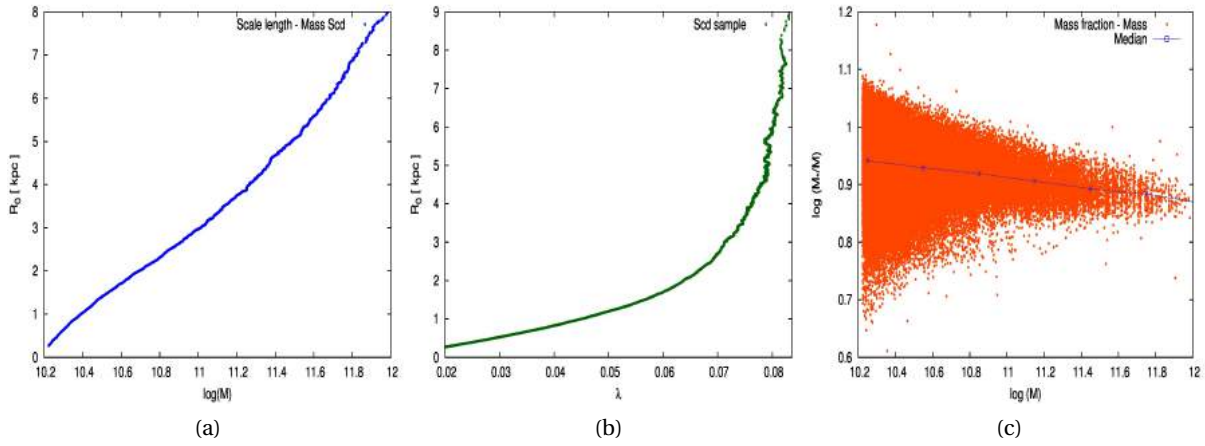


Figure 53: Scd galaxies. (a) Scale length vs virial mass of the dark matter halo. A galaxy's scale length increases with virial mass. Less massive dark matter halos are expected to contain small galaxies compared with bigger ones. (b) Scale length vs spin parameter. Same as the virial mass the spin parameter is expected to increase in this population for bigger scale lengths. (c) represents in the y-axis the mass fraction M_*/M_{vir} against the virial mass in the x-axis. For bigger virial mass the less mass fraction, however it is not so noticeable.

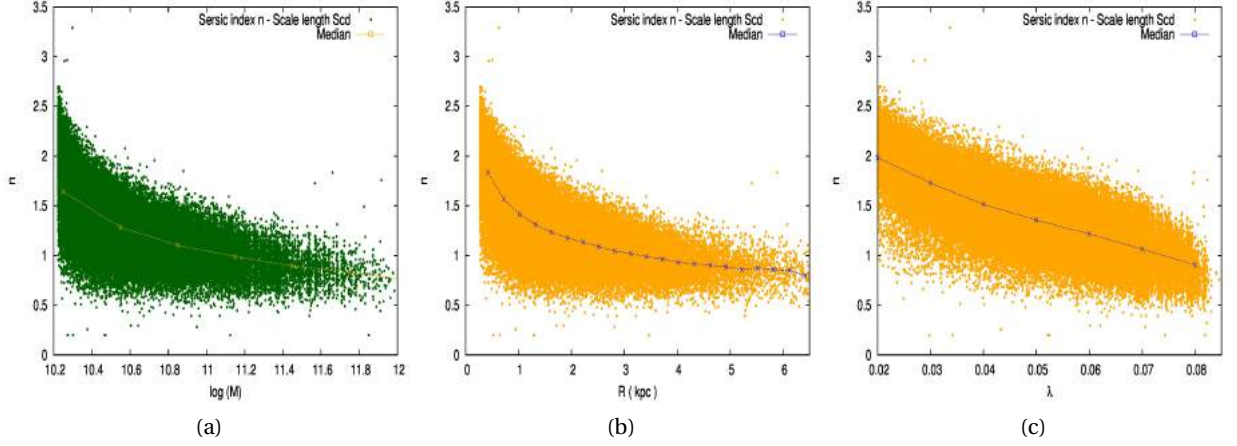


Figure 54: Scd galaxies. (a) Sérsic's index n vs virial mass. As expected lower virial mass, lower Sérsic n index which is interpreted as spiral galaxies which is the sample we have. (b) Sérsic's index n vs scale length. To higher scale length the lower Sérsic's index n . (c) Sérsic's index n vs spin parameter. Higher spin parameter the lower Sérsic's index.

sample of 76.471 *Sab* galaxies and 90.541 *Scd* galaxies. Our whole sample was reduced after the matching process because a few galaxies were too small such that the model was not able to match them. Moreover, we cut-off our last sample again and we chose only those objects whose spin parameter was sufficiently large such as $\lambda \geq 0.02$. Finally, the main result is that through comparing disk scale lengths one is able with the (Mo, Mao & White) model to infer the parameters that will describe the dark matter halo where a given galaxy is being hosted. In [Table 12](#) and [Table 13](#) are summarized the median values get through the matching for the first ten objects both for *Sab* as *Scd*. Each object is characterized by an *ID* which is just like an order tag. All the physical quantities are the median values computed with the whole targets obtained for a given galaxy through the matching process. The disk scale length is in *kpc*, concentration and spin parameter λ are dimensionless, the virial mass of the dark matter halo is in logarithm and given in solar mass units M_\odot and the surface brightness in M_\odot/pc^2 .

After analyzing the behavior of the extracted parameter with the matching process we proceed to perform the same steps but in this case with the Sérsic's parameters and other quantities of interest as redshift and petrosian magnitude in the *r*-band. This just to find direct correlations for the *Sab* and *Scd* galaxies. This will help us out to find one parameter in terms another one. Thus, in [Figure 55](#), [Figure 56](#), [Figure 59](#), [Figure 58](#), [Figure 57](#), [Figure 61](#) and [Figure 60](#), we can find the *Sab* and *Scd* samples.

First of all, to analyze the behavior of a given Sérsic parameter against redshift, stellar mass or magnitude we took the sample constituted by 151.031 *Sab* and 106.606 *Scd* galaxies. We also cut the whole sample taking into account that the only galaxies which can help us to know some correlations between the spiral objects are those which n Sérsic parameter satisfy $0 \leq n \leq 2$ because it ensures that those objects are disks instead of spheroids.

In [Figure 55](#) there is the surface brightness parameter A_r in the *r*-band as a function of the stellar mass for both *Sab* (panel (a)) and *Scd* (panel (b)). Stellar masses are in solar mass units and surface brightness are in units of the SDSS. For the *Sab* objects the orange dots are the total sample and the yellow ones represents those with $0 \leq n \leq 2$, same for the *Scd* where the total sample are the green dots and the selected are the blue ones. The line with dots fitted to the

Table 12: **Sab final sample result**

ID	R_d [kpc]	C	$\log(M_{vir})$	λ	Σ_0 [M_\odot/pc^2]
1	0.012	14.355	10.199	0.006	874015.04
2	0.346	14.249	10.239	0.023	1107.05
3	0.477	14.161	10.268	0.028	622.99
4	0.928	13.834	10.373	0.043	211.04
5	0.358	14.245	10.241	0.024	1036.39
6	0.082	14.356	10.199	0.011	18204.04
7	1.383	13.471	10.492	0.054	125.84
8	0.222	14.325	10.213	0.018	2550.14
9	4.697	10.962	11.408	0.078	90.10
10	2.227	12.676	10.775	0.066	92.47

Table 13: **Scd final sample result**

ID	R_d [kpc]	C	$\log(M_{vir})$	λ	Σ_0 [M_\odot/pc^2]
1	0.989	13.797	10.387	0.045	191.87
2	0.029	14.359	10.199	0.008	147665.69
3	2.867	12.121	10.969	0.071	88.58
4	2.458	12.474	10.837	0.069	88.28
5	0.963	13.810	10.380	0.044	199.15
6	0.269	14.289	10.223	0.020	1754.29
7	0.489	14.157	10.269	0.029	591.80
8	1.995	12.894	10.689	0.064	96.01
9	0.873	13.886	10.356	0.041	229.46
10	0.495	14.156	10.269	0.029	581.51

selected sub-sample are the median values. In panel (c) we see both median values for each sub-sample. *Sab* galaxies have larger values of A_r than *Scd* because the last ones are more close to disk-types than spheroids. However, both show that for larger values of the stellar mass we have larger values of surface brightness which makes sense because an increase in stellar mass means more luminous sources.

Now let's compare the surface brightness with the redshift. In [Figure 56](#) once again the color codes mean the same as said before and the line with dots are the mean values. What is really interesting here as seen in panel (c) is that for both sub-samples to large redshifts the surface brightness increases which means that we are seeing the brightest objects so our sample is affected by the *Malmquist – Bias*. However, this does not affect what we have performed before because we were just comparing, although this has to be corrected if we want to use any of these relations to perform some analysis.

Finally in [Figure 57](#) we can find the surface brightness now compared with the magnitude in the r -band. One can clearly see how to lower magnitudes (large luminosity) the surface brightness increases. This is expected because more luminous galaxies are in general bigger which increases the surface brightness but this could also be *Malmquist – Bias*. Once again, *Sab* are bigger and more luminous than *Scd* because as seen throughout last chapters they are a transition between the spheroidal and disk objects. Although surface brightness is in units of the SDSS we know how to convert them into physical units which can be helpful to relate the surface brightness density obtained through the matching process and the surface brightness measured using a given stellar mass luminosity relation.

Let's now focus on the disk scale length. In [Figure 58](#) we have the scale length in the y -axis in kpc and the stellar mass in the x -axis in solar mass units. Orange and green dots in panel (a) and (b) respectively represents the whole sample while yellow and blue the selected sample under the assumptions done over the Sérsic index n . In panel (c) we can see how this time *Sab* galaxies have lower values of the disk scale length in comparison with *Scd*, although both increase with stellar mass. *Sab* galaxies have low values of scale length because these objects are close to the elliptical class, so their photometric nature represented by the Sérsic's profile shows a large difference between the intensity at the centre $I(0)$ respect the the intensity in the outskirts $I(R)$. *Scd* on the contrary have not a strong gradient in their intensity which leads to higher values of the disk scale length.

In [Figure 59](#) is shown the correlation between the disk scale length and the magnitude in the r -band. We can observe here that those objects more luminous (i.e with lower magnitudes) show a large scale length (bias). Finally, in [Figure 60](#) panel (c) we see the scale length dependence on redshift which shows once again *Malmquist – Bias* because large objects are predominant at large redshifts. Though to perform an analysis to relate properties and characterize the photometric sample which can be performed in other work one must to cut the samples in volume and not in magnitude to avoid *Malmquist – Bias*.

The n -index has been studied along the whole document. However, we performed in [Figure 61](#) plots for the *Sab* and *Scd* galaxies as a function of redshift. Here is evident the cut-off point done to select objects below $n = 2$. Which is interesting here is that we confirm that the *Sab* sample has large values of n once again because they are more close to the spheroidal sample which implies that they Sérsic index must to increase. *Scd* however are close to a pure spiral-type. This parameter is not strong affected by the *Malmquist – Bias* as the surface brightness or the disk scale length because the shape of the surface brightness profile doen not depend on the distance to an object. Although, we do not use this last result here it is useful as said before when you need

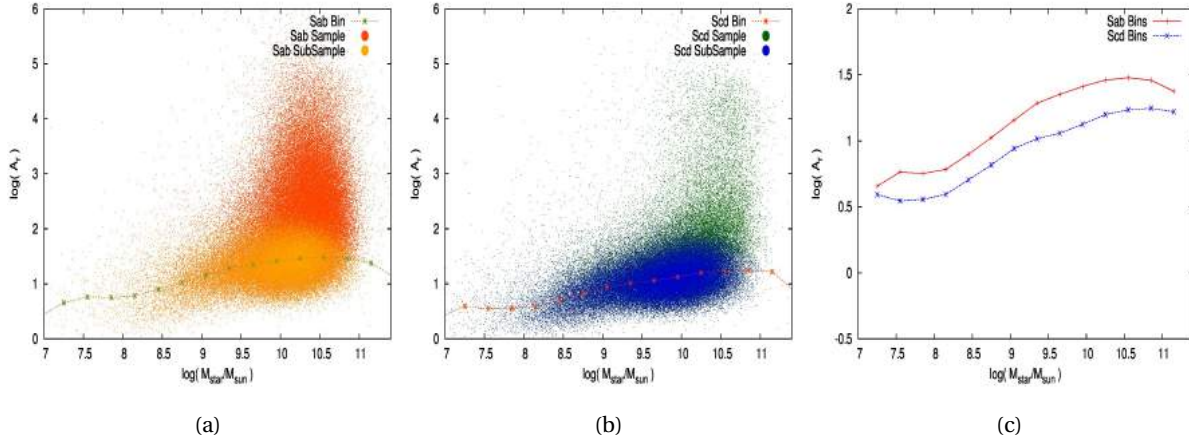


Figure 55: Surface brightness parameter A from Sérsic's profile vs Stellar mass of each object. (a) we can find in this figure the surface brightness in the r -band for the *Sab* galaxies in the y-axis and the stellar mass of those objects in the x-axis. Orange dots are the whole *Sab* sample while the yellow ones are a subsample extracted for those galaxies with Sérsic's index n between 0 and 2. Olive dots-line are the median values of the subsample. (b) Same as the first plot but in this case for the *Scd* sample. Green dots are the whole sample while blue ones are the subsample. Orange dots-line are the median values of the subsample. (c) Shows the median values both *Sab* (red-line) and *Scd* (blue-line) samples.

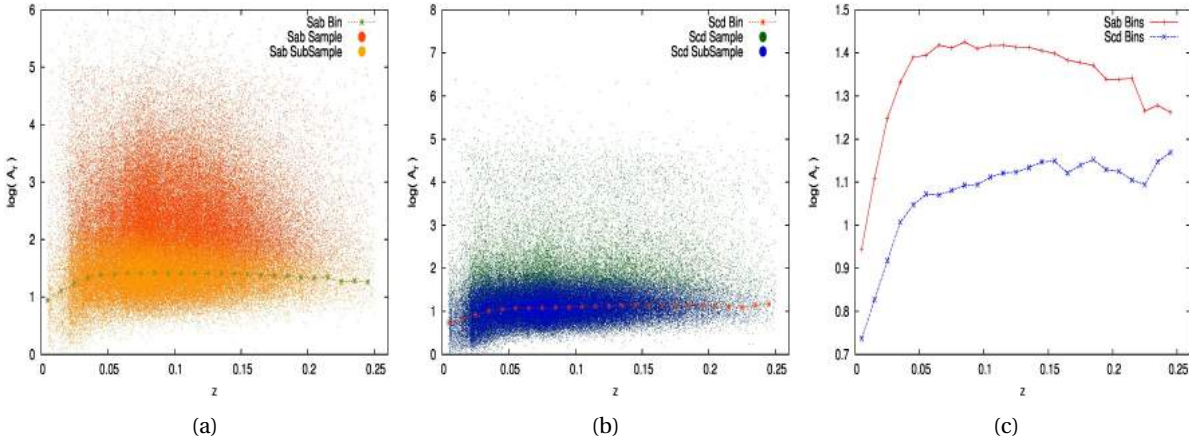


Figure 56: Surface brightness parameter A from Sérsic's profile vs measured redshift of each object. (a) we can find in this figure the surface brightness in the r -band for the *Sab* galaxies in the y-axis and measured redshift for those objects in the x-axis. Orange dots are the whole *Sab* sample while the yellow ones are a subsample extracted for those galaxies with Sérsic's index n between 0 and 2. Olive dots-line are the median values of the subsample. (b) Same as the first plot but in this case for the *Scd* sample. Green dots are the whole sample while blue ones are the subsample. Orange dots-line are the median values of the subsample. (c) Shows the median values both *Sab* (red-line) and *Scd* (blue-line) samples.

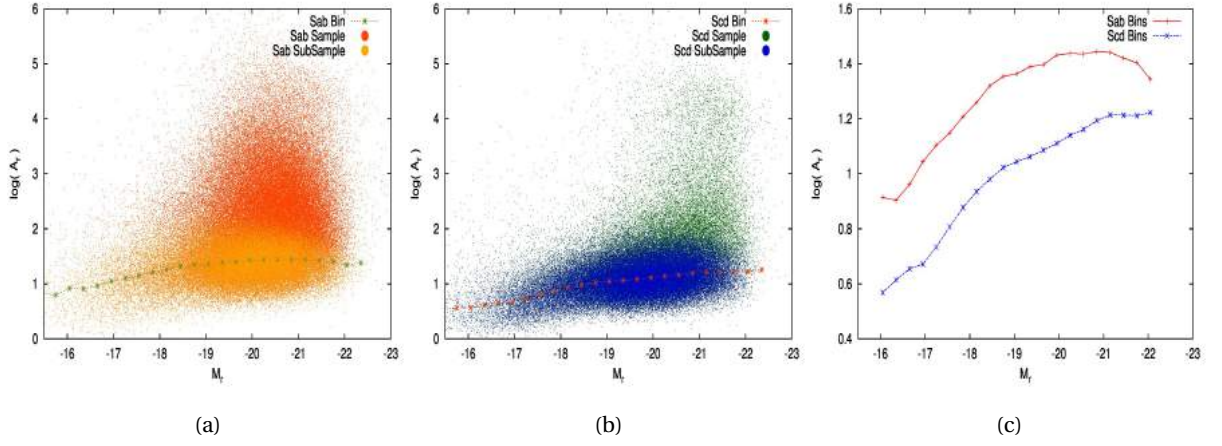


Figure 57: Surface brightness parameter A from Sérsic's profile vs Absolute magnitude in the r – band.

(a) we can find in this figure the surface brightness in the r -band for the *Sab* galaxies in the y-axis and absolute magnitude for those objects in the x-axis. Orange dots are the whole *Sab* sample while the yellow ones are a sub sample extracted for those galaxies with Sérsic's index n between 0 and 2. Olive dots-line are the median values of the subsample. (b) Same as the first plot but in this case for the *Scd* sample. Green dots are the whole sample while blue ones are the subsample. Orange dots-line are the median values of the subsample. (c) Shows the median values both *Sab* (red-line) and *Scd* (blue-line) samples.

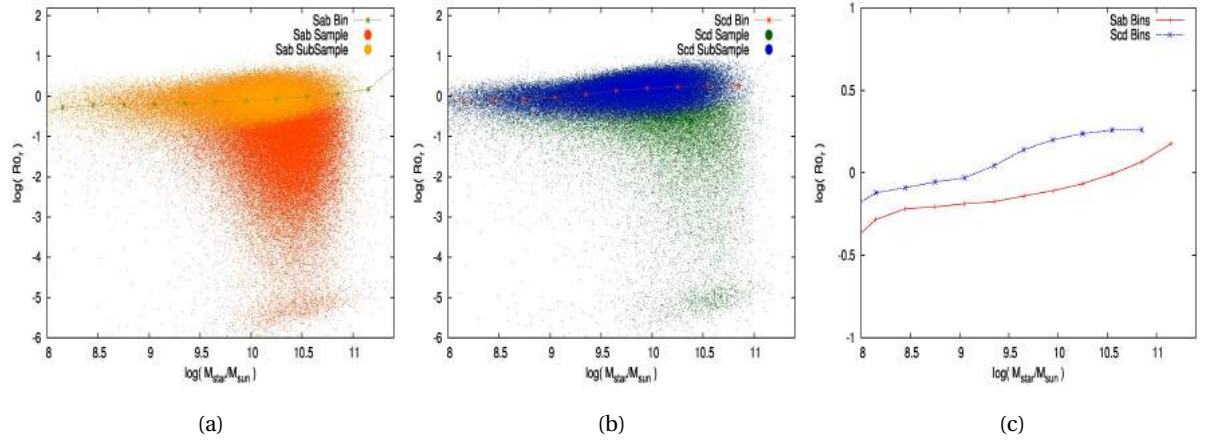


Figure 58: Scale length parameter R_0 from Sérsic's profile vs Stellar mass of each galaxy. (a) we can find in this figure the scale length parameter in the r -band for the *Sab* galaxies in the y-axis and stellar mass for those objects in the x-axis. Orange dots are the whole *Sab* sample while the yellow ones are a sub sample extracted for those galaxies with Sérsic's index n between 0 and 2. Olive dots-line are the median values of the subsample. (b) Same as the first plot but in this case for the *Scd* sample. Green dots are the whole sample while blue ones are the subsample. Orange dots-line are the median values of the subsample. (c) Shows the median values both *Sab* (red-line) and *Scd* (blue-line) samples.

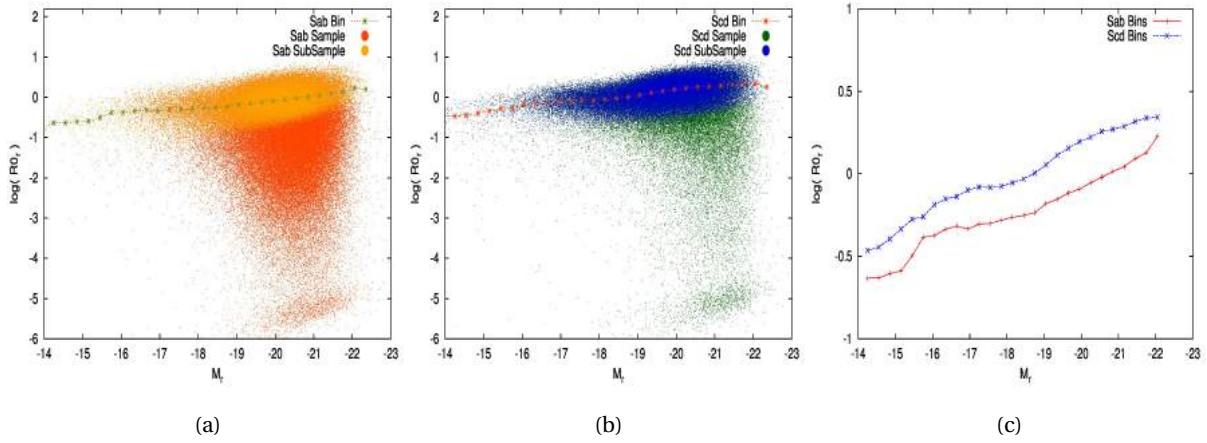


Figure 59: Scale length parameter R_0 from Sérsic's profile vs Absolute magnitude in the r – band. (a) we can find in this figure the scale length parameter for the *Sab* galaxies in the y-axis and absolute magnitude for those objects in the x-axis, both in the r -band. Orange dots are the whole *Sab* sample while the yellow ones are a sub sample extracted for those galaxies with Sérsic's index n between 0 and 2. Olive dots-line are the median values of the subsample. (b) Same as the first plot but in this case for the *Scd* sample. Green dots are the whole sample while blue ones are the subsample. Orange dots-line are the median values of the subsample. (c) Shows the median values both *Sab* (red-line) and *Scd* (blue-line) samples.

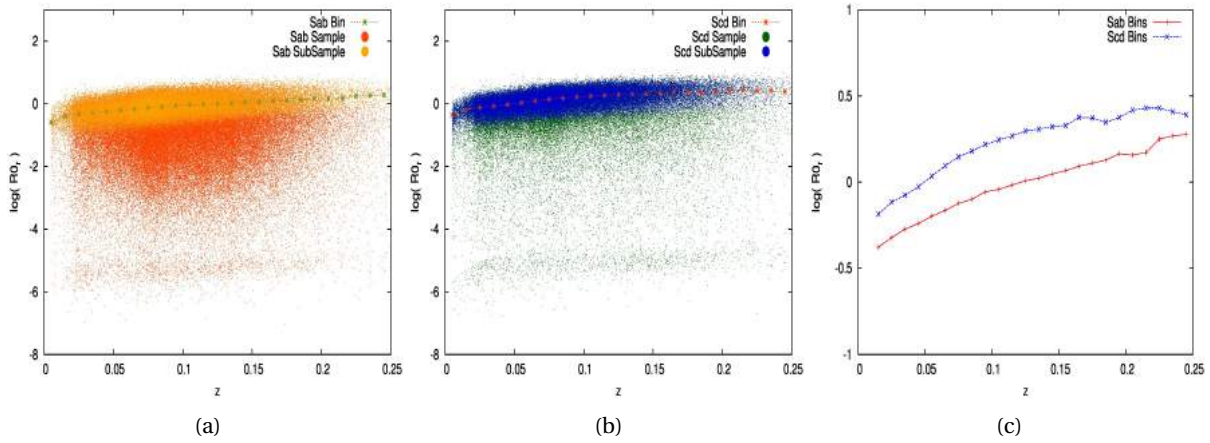


Figure 60: Scale length parameter R_0 from Sérsic's profile vs measured redshift of each object. (a) we can find in this figure the scale length in the r -band for the *Sab* galaxies in the y-axis and measured redshift for those objects in the x-axis. Orange dots are the whole *Sab* sample while the yellow ones are a sub sample extracted for those galaxies with Sérsic's index n between 0 and 2. Olive dots-line are the median values of the subsample. (b) Same as the first plot but in this case for the *Scd* sample. Green dots are the whole sample while blue ones are the subsample. Orange dots-line are the median values of the subsample. (c) Shows the median values both *Sab* (red-line) and *Scd* (blue-line) samples.

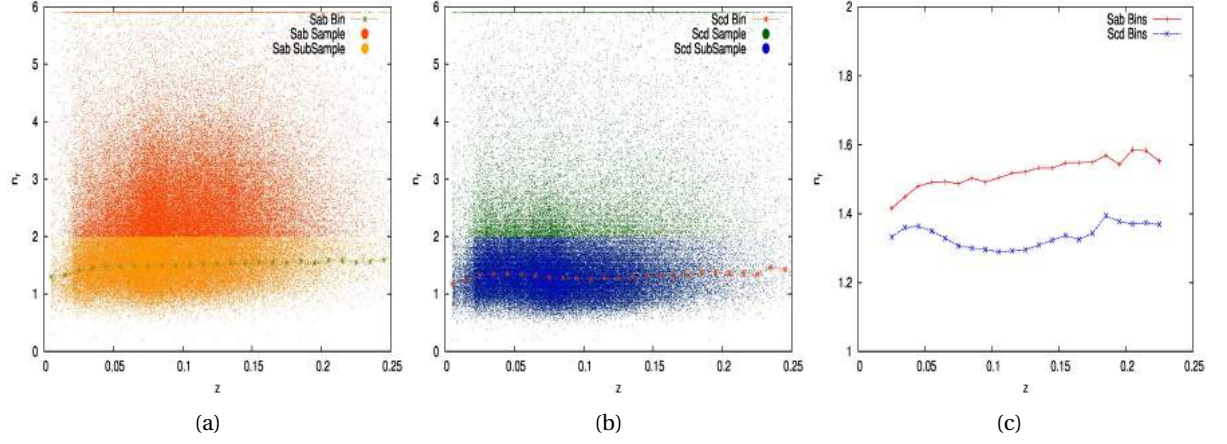


Figure 61: n -index from Sérsic's profile in the r – $band$ vs measured redshift of each object. (a) we can find in this figure the n -index in the r -band for the *Sab* galaxies in the y-axis and measured redshift for those objects in the x-axis. Orange dots are the whole *Sab* sample while the yellow ones are a sub sample extracted for those galaxies with Sérsic's index n between 0 and 2. Olive dots-line are the median values of the subsample. (b) Same as the first plot but in this case for the *Scd* sample. Green dots are the whole sample while blue ones are the subsample. Orange dots-line are the median values of the subsample. (c) Shows the median values both *Sab* (red-line) and *Scd* (blue-line) samples.

to see correlations between the distinct parameters. Indeed, it is useful to connect the surface brightness with the surface density through an stellar mass-luminosity relation and performe this same analysis we have done with the disk scale length but now with other parameter of the Sérsic's profile.

DISCUSSION AND SUMMARY

4.1 DISCUSSION

In this thesis we use a sample of 698.420 galaxies from the SDSS [7] divided in two groups of elliptical and spiral galaxies which were indeed subdivided into two classes each one, *Ell* and *S0* for the ellipticals, *Sab* and *Scd* for the spirals. All this galaxies belongs to the data base provided by Huertas-Company, 2010 [19]. To enrich the original sample which only contains a given probability of belonging to a certain class and subclass, we performed a match between this galaxies with the VAGC-NYU catalog [11] to obtain new data as the Sérsic's profile parameters, absolute magnitudes in the petrosian filters u, g, r, i, z , velocity dispersion and so on. In the original set of galaxies we set a selection criteria between the main probability of belonging to an early-type or late-type to be safe when characterizing galaxies of a given class. With this, we ensure that selected galaxies are approximately as close as possible to the tagged type.

Supported on Mo, Mao & White's model [22] we were able to compute the scale lengths and the surface density of model galaxies using modelled dark matter halo properties such as spin parameter, concentration and virial mass of the dark matter haloes. Once one has a certain collection of modelled galaxies there is a straight way to connect the observed galaxies with the modelled quantities through matching them with the scale lengths. We perform this using a simple criteria where we looked for different values which can match the observed scale length, always between an interval we set to $\pm 0.1 R_0$. Finally and without forgetting that the model only is helpful for disk galaxies, and cutting the samples in good redshifts, reasonable intervals of the parameters and well behaved data we obtained a final sample of 76.471 *Sab* and 90.541 *Scd* galaxies which have a potential related spin parameter, concentration and virial mass for the dark matter halo where it is embedded. As an extra, relation between all the parameters were found to see correlations that can be useful to compute a parameter in terms of another one. When we perform the analysis between the spin, concentration and virial mass parameters which describes the dark matter halo it is easy to see that before comparing the observable data with the model there is no correlation between the spin parameter and the concentration. However, after performing the matching both parameters correlate each other which indicates that if one wants to build-up a galaxy of a given scale length inside a dark matter halo with a given virial mass the spin parameter must be related to the concentration (i.e virial mass) and can not take an arbitrary value. This correlation is induced because the model connects the observable parameters of galaxies with those of the dark matter halo relating them with each other.

As it can be seen, the main goal was to connect photometric properties of the disk galaxies with parameters of the dark matter halo where those galaxies could be hosted. However, there is no much about this issue or this way of performing the analysis in literature. We were aimed because inferring information about the dark matter halo from real observed galaxies could be useful to model disk galaxies in a way that can be more appropriated. A big number of galaxies through this work were discriminated because they have bad measured properties such as those spiral galaxies with Sérsic's n -index bigger than 2, redshifts beyond 0.25 or spin parameter close or

exactly to zero. We set lots of conditions to finally have a safe sample where we can be sure of it. A sample where one can trust that the noise have been minimized.

The comparison between the data provided by [19] (morphological classification) and [11] (photometric characterization) it showed the expected results because the segregation between the different types of galaxies as shown in the fundamental plane, Sérsics plots, CMD and velocity dispersion plots are in an appropriate range. As shown throughout the Chapter 2 and Chapter 3 there is a connection between the observed properties of galaxies with the parameters which characterizes the dark matter halo because the hierarchical process where galaxies are formed. Thus, once we know the disk scale length we can go ahead and compare different objects to extract the mean values of spin and concentration parameters and the virial mass of the dark matter halo where they formed at. As seen for larger values of the scale length we get wide ranges of spin, concentration and virial masses, while for small values the distributions are more close. To small values of the spin parameter, we observe small galaxies with closely values of virial mass and concentration. After cleaning off data the *Sab* and *Scd* samples behave quite similar because their shared galaxies disappear. However, some differences between their Sérsic parameters against the redshift, luminosity and stellar mass raise up which can indicates that probably the different values of the sub-samples are due to structural differences between their dark matter halos. Despite this, our sample is affected by *Malmquist – Bias* as can be seen in those plots when the surface brightness and the scale length are involved with the redshift or luminosity. However, this does not affect our selection method because we are not comparing the different behavior of each parameter, but we must to limit our sample in volume and not in magnitude to perform a better analysis of this differences of the photometric parameters for a given morphological class if we want to find the real relations between some parameters of interest.

However, it is interesting to perform this analysis with new SDSS data, albeit the new issue here is that the probabilities which were calculated by [19] now must be performed by us. Using new data will remove lots of issues that this sample could have, indeed it will be helpful to compare if our analysis is sufficiently robust towards changing the main sample. In addition, it will give more fine parameters and new ones which will enrich the sample. We will maybe intend to return to face this issues in future works with new data.

We are grateful with Huertas-Company [19] for freely providing his results on characterizing galaxies through probabilities which was our starting point, the SDSS and the VAGC-NYU data base. Although to all the people who in one way or another helped us with discussions and advices.

4.2 FUTURE PROSPECTS

Once we have checked that our method works, it is useful to refine our criteria and statistical methods to compare the observations with the model. We must to ensure that the data we are giving are robust and integral. So, our next goal is to publish this results which could be really useful for people who looks for adequate dark matter halo initial parameters to model galaxy mergers or dark matter halo structures. To perform this we must:

- To use more and better data which can be provided by the SDSS-DR12.

- We should include the dependence on redshift for the model galaxies because they were computed for $z = 0$, so solving this can help to reduce the scatter in our final data providing a sample with more accuracy.
- It is necessary to take into account the *Malmquist – Bias* and fix it because dark matter halos are at different redshifts so one should compute the matching with distinct samples according to the redshift of each galaxy.
- Use a better and stronger constraint than 10% of R_0 . Also we can perform the same comparison through the surface mass density if we can obtain the mass-luminosity relation which can be deduced for a given sample through the photometric data relations provided by the survey.
- Use statistical inference techniques which can help us to obtain a larger sample.
- Finally, to publish the results.

Although our main results and behavior will not be altered at least in their interpretation, our samples will be in an statistical way better and more suitable to public use.

BIBLIOGRAPHY

- [1] URL. http://gepicom04.obspm.fr/sdss_morphology/Morphology_2010.html.
- [2] URL. <http://ned.ipac.caltech.edu/level5/March01/Battaner/node27.html>.
(Cited on page 34.)
- [3] URL. <https://www.sdss3.org/dr8/algorithms/magnitudes.php>, . (Cited on page 50.)
- [4] URL. <http://skyserver.sdss.org/dr1/en/proj/advanced/color/sdssfilters.asp#filters>, . (Cited on page 40.)
- [5] URL. <https://bama.ua.edu/~rbuta/gvatlas/devsys.html>. (Cited on page 8.)
- [6] URL. <http://ned.ipac.caltech.edu/level5/CLASSIFICATION/yc.html>. (Cited on page 10.)
- [7] K. N. Abazajian, J. K. Adelman-McCarthy, M. A. Agüeros, S. S. Allam, C. Allende Prieto, D. An, K. S. J. Anderson, S. F. Anderson, J. Annis, N. A. Bahcall, and et al. The Seventh Data Release of the Sloan Digital Sky Survey. *The Astrophysical Journal Supplement Series*, 182:543–558, jun 2009. (Cited on pages iii, 37, 38, and 95.)
- [8] A. J. Benson. Galaxy formation theory. *Physics Reports*, 495:33–86, oct 2010. (Cited on pages 22, 28, 29, 30, and 33.)
- [9] James Binney and Michael Merrifield. *Galactic Astronomy*. Princeton University Press, 1998. (Cited on pages 2, 3, 4, and 8.)
- [10] M. R. Blanton, J. Brinkmann, I. Csabai, M. Doi, D. Eisenstein, M. Fukugita, J. E. Gunn, D. W. Hogg, and D. J. Schlegel. Estimating Fixed-Frame Galaxy Magnitudes in the Sloan Digital Sky Survey. *Astronomical Journal*, 125:2348–2360, may 2003. (Cited on page 39.)
- [11] M. R. Blanton, D. J. Schlegel, M. A. Strauss, J. Brinkmann, D. Finkbeiner, M. Fukugita, J. E. Gunn, D. W. Hogg, Ž. Ivezić, G. R. Knapp, R. H. Lupton, J. A. Munn, D. P. Schneider, M. Tegmark, and I. Zehavi. New York University Value-Added Galaxy Catalog: A Galaxy Catalog Based on New Public Surveys. *Astronomical Journal*, 129:2562–2578, jun 2005. (Cited on pages iii, 37, 39, 40, 41, 71, 95, and 96.)
- [12] Michael R. Blanton and Hogg. et al. The Broadband Optical Properties of Galaxies with Redshifts $0.02 < z < 0.22$. *The Astrophysical Journal*, 594(1):186, 2003. (Cited on pages 13, 15, and 39.)
- [13] Dale A. Ostlie Bradley W. Carroll. *An Introduction to Modern Astrophysics (2nd Edition)*. Addison-Wesley, 2006. (Cited on pages 6 and 7.)
- [14] Andreas. Burkert. Galactic disk formation and the angular momentum problem. *ASP conference series*, 419:3–9, 2009. (Cited on pages 29, 30, and 31.)
- [15] R. J. Buta. Galaxy Morphology. *ArXiv e-prints*, February 2011. (Cited on pages 2 and 15.)

- [16] R. Buta & F. Combes. Galactic Rings. *Fund. Cosmic Physics*, 17:95–281, 1996. (Cited on page 9.)
- [17] G. Gavazzi, M. Fumagalli, O. Cucciati, and A. Boselli. A snapshot on galaxy evolution occurring in the Great Wall: the role of Nurture at $z = 0$. *Astronomy & Astrophysics*, 517:A73, July 2010. (Cited on pages 12 and 13.)
- [18] D. W. Hogg. Distance measures in cosmology. *ArXiv Astrophysics e-prints*, may 1999. (Cited on pages 20, 21, and 22.)
- [19] M. Huertas-Company, J. A. L. Aguerri, M. Bernardi, S. Mei, and J. Sánchez Almeida. Revisiting the Hubble sequence in the SDSS DR7 spectroscopic sample: a publicly available Bayesian automated classification. *Astronomy & Astrophysics*, 525:A157, jan 2011. (Cited on pages iii, 37, 41, 42, 43, 46, 47, 51, 57, 60, 95, and 96.)
- [20] A. V. Macciò, A. A. Dutton, F. C. van den Bosch, B. Moore, D. Potter, and J. Stadel. Concentration, spin and shape of dark matter haloes: scatter and the dependence on mass and environment. *Monthly Notices of the Royal Astronomical Society*, 378:55–71, June 2007. (Cited on page 79.)
- [21] A. V. Macciò, A. A. Dutton, and F. C. van den Bosch. Concentration, spin and shape of dark matter haloes as a function of the cosmological model: WMAP1, WMAP3 and WMAP5 results. *Monthly Notices of the Royal Astronomical Society*, 391:1940–1954, December 2008. (Cited on page 77.)
- [22] H. J. Mo, S. Mao, and S. D. M. White. The formation of galactic discs. *Monthly Notices of the Royal Astronomical Society*, 295:319–336, April 1998. (Cited on pages iii, 37, 71, 72, 73, 78, and 95.)
- [23] W. W. Morgan. A Preliminary Classification of the Forms of Galaxies According to Their Stellar Population. 70:364, August 1958. (Cited on page 9.)
- [24] W. W. Morgan. SOME CHARACTERISTICS OF GALAXIES. *ApJ*, 1:1, 1962. (Cited on pages 10 and 18.)
- [25] J. C. Muñoz-Cuartas, A. V. Macciò, S. Gottlöber, and A. A. Dutton. The redshift evolution of Λ cold dark matter halo parameters: concentration, spin and shape. *Monthly Notices of the Royal Astronomical Society*, 411:584–594, feb 2011. (Cited on pages 33, 34, 35, 75, and 76.)
- [26] F. Prada, A. A. Klypin, A. J. Cuesta, J. E. Betancort-Rijo, and J. Primack. Halo concentrations in the standard Λ cold dark matter cosmology. *Monthly Notices of the Royal Astronomical Society*, 423:3018–3030, July 2012. (Cited on page 34.)
- [27] M.S. Roberts and M.P. Haynes. Physical Parameters along the Hubble Sequence. *Annual Review of Astronomy & Astrophysics*, 32:115–152, 1994. (Cited on pages 14, 15, 16, and 17.)
- [28] Peter Schneider. *Extragalactic Astronomy and Cosmology: An Introduction*. Springer, 2006. (Cited on pages 47, 49, and 50.)
- [29] S. Shen, H. J. Mo, S. D. M. White, M. R. Blanton, G. Kauffmann, W. Voges, J. Brinkmann, and I. Csabai. The size distribution of galaxies in the Sloan Digital Sky Survey. *Monthly Notices of the Royal Astronomical Society*, 343:978–994, August 2003. (Cited on page 71.)

- [30] Sidney van den Bergh. *Galaxy Morphology and Classification*. Cambridge University Press, 1998. (Cited on pages [11](#) and [12](#).)